Imaging Atoms and Molecules with Strong Laser Fields

Author:
Christopher Smeenk

Supervisor:
Dr. Paul Corkum

University of Ottawa

Ph.D. Thesis

April 2013

Imaging Atoms and Molecules with Strong Laser Fields

Christopher Smeenk

Thesis submitted to the
Faculty of Graduate and Postdoctoral Studies
in partial fulfillment of the requirements
for a doctoral degree in Physics

Department of Physics
Faculty of Science
University of Ottawa

For my mother and father

Abstract

We study multi-photon ionization of rare gas atoms and small molecules by infrared femtosecond laser pulses. We demonstrate that ionization is accurately described by a tunnelling model when many infrared photons are absorbed. By measuring photo-electron and photo-ion spectra, we show how the sub-Ångstrom spatial resolution of tunnelling gives information about electron densities in the valence shell of atoms and molecules.

The photo-electron and photo-ion momentum distributions are recorded with a velocity map imaging (VMI) spectrometer. We describe a tomographic method for imaging a 3-D momentum distribution of arbitrary symmetry using a 2-D VMI detector. We apply the method to measure the 3-D photo-electron distribution in elliptically polarized light.

Using circularly polarized light, we show how the photo-electron momentum distribution can be used to measure the focused laser intensity with high precision. We demonstrate that the gradient of intensities present in a focused femtosecond pulse can be replaced by a single average intensity for a highly nonlinear process like multi-photon ionization.

By studying photo-electron angular distributions over a range of laser parameters, we determine experimentally how the photon linear momentum is shared between the photo-electron, photo-ion and light field. We find the photo-electron carries only a portion of the total linear momentum absorbed. In addition we consider how angular momentum is shared in multi-photon ionization, and find the photo-electron receives *all* of the angular momentum absorbed.

Our results demonstrate how optical and material properties influence the photo-electron spectrum in multi-photon ionization. These will have implications for molecular imaging using femtosecond laser pulses, and controlling the initial conditions of laser generated plasmas.

Contents

Chapter 1

Introduction to Ultrafast Science

The evolution of ultrafast science is closely coupled to developments in ultrafast technology. The first ultrafast scientist was arguably August Toepler (1836–1912) who used a high voltage discharge over a spark gap to create shock waves [1]. To observe the sound waves he invented the schlieren imaging method in 1859. Also in the 19th century Eadweard Muybridge and Étienne-Jules Marey used primitive cinematography to record the motion of animals and fluids. Muybridge's images of a horse galloping conclusively demonstrated that horses go completely airborne at certain phases of their gallop. The images generated an immediate sensation and were picked up by Scientific American magazine in 1878. Marey's diverse studies of moving fluids, people and animals are no less striking (see Fig. 1.1). The 19th century marks the first scientific and artistic applications of ultrafast technology that surpass the resolution of human vision (30 ms), hearing (10 ms), and touch ($\sim$ 100 ms) [2, 3, 4].

In the mid 20th century stroboscopic measurements by Harlod Edgerton and collaborators advanced the time resolution to microseconds. They used ultrafast techniques to make iconic photographs of fluid drops breaking and fruit exploding among other phenomena (see Fig. 1.1). By the second half of the 20th century high speed photography had reached nanosecond time resolution and could go no further. This lower limit is a reflection of the large dispersion in the microwave region of almost all solid materials due to lattice vibrations [5]. This causes rapid distortion of octave spanning ultrashort electronic pulses. Consequently the time resolution of a conventional strobe

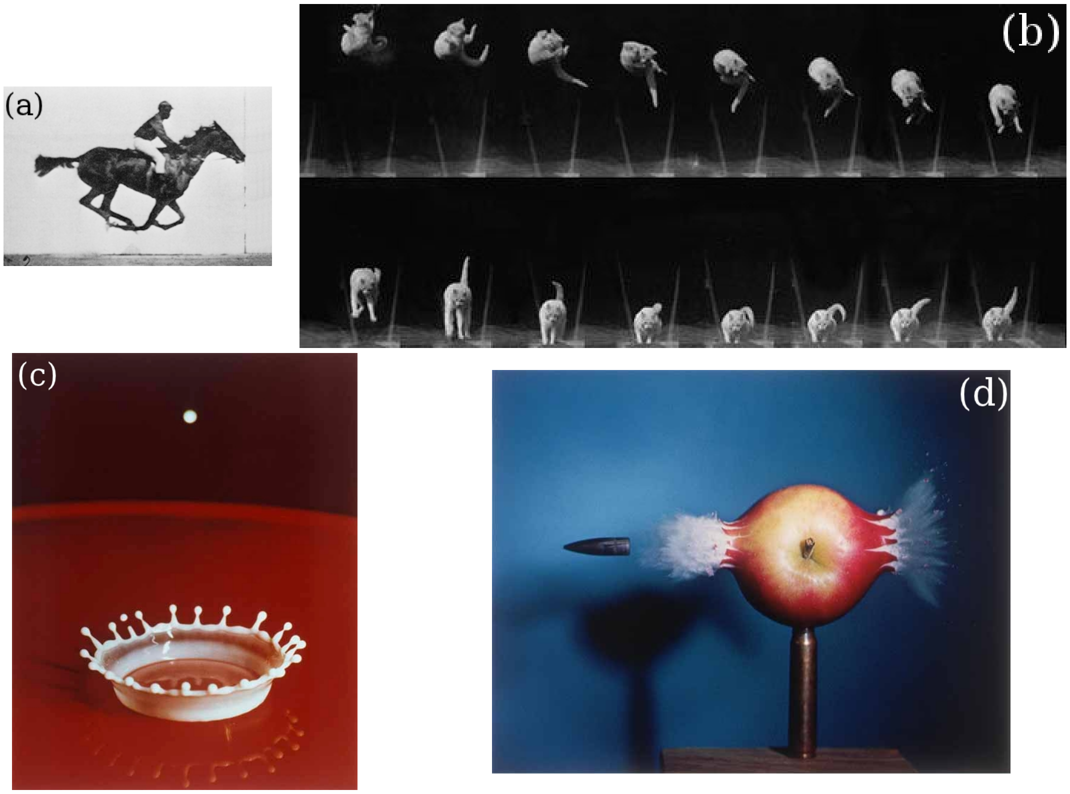

Figure 1.1: (a) 1878 photograph of a galloping horse by E. Muybridge. (b) 1894 photo series of a falling cat by É. J. Marey. (c) 1957 image of a milk drop coronet by H. Edgerton *et al* (d) 1964 image of a bullet piercing an apple by H. Edgerton *et al*

light pulse or CCD readout cannot reliably be less than tens of picoseconds. Further development in ultrafast science therefore called for a new technology.

Fortunately around the same period as ultrafast electronics was beginning to plateau, the laser was invented. Subsequent developments in nonlinear optics made it possible to apply strobe-like pump-probe techniques to resolve events down to a few femtoseconds by the 1990s. This led to the 1999 Nobel Prize in Chemistry to Ahmed Zewail for real-time observations on the breaking and formation of chemical bonds [6].

Eventually ultrafast optics also reached a lower limit given by the optical frequency. One cycle of a visible light wave is a couple femtoseconds, and optical pulses cannot surpass this limit. Continued advances in the field of ultrafast science requires (a) shorter wavelength radiation and (b) attention to the dynamics of matter on *sub-cycle* time scales. By using strong laser fields and particles with small mass, it is possible to manipulate these dynamics. This offers an avenue to generate attosecond XUV pulses and is the current state of the art in ultrafast technology and science. In 2001 two labs succeeded in generating attosecond XUV pulses [7, 8]. This marks the beginning of experimental attosecond science, allowing us to “watch” motion on time scales shorter than the period of one visible light wave.

1.1 Wave Optics

Light is a transverse electromagnetic (EM) wave and can be characterized by it’s oscillating electric field,

$$\boldsymbol{E}(\boldsymbol{r},t) = E_0 f(\boldsymbol{r},t)\left[\cos(\omega t - kz)\hat{\imath} + \epsilon\sin(\omega t - kz)\hat{\jmath}\right] \tag{1.1}$$

where E_0 is the maximum electric field, ϵ is the ellipticity, k is the wave number and ω is the angular frequency. The function $f(\boldsymbol{r},t)$ represents the pulse envelope and is given by $f(\boldsymbol{r},t) = \exp\left(-2\ln 2(z-ct)^2/c^2\tau^2\right)$ where c is the speed of light in vacuum and τ is the pulse duration FWHM in intensity. The magnetic field is given by

$$\nabla \times \boldsymbol{B} = \mu_0 \boldsymbol{J} + \frac{1}{c^2}\frac{\partial \boldsymbol{E}}{\partial t} \ . \tag{1.2}$$

We can drop the term $\propto \boldsymbol{J}$ for a travelling wave or interactions with low density gases. The magnetic field of the light pulse is then approximately

$$\boldsymbol{B}(\boldsymbol{r},t) = \frac{E_0}{c} f(\boldsymbol{r},t)\left[-\epsilon\sin\left(\omega t - kz\right)\hat{\imath} + \cos\left(\omega t - kz\right)\hat{\jmath}\right] \ . \tag{1.3}$$

In Eq. (1.3) we have neglected terms $\frac{\partial}{\partial t} f(\boldsymbol{r},t)$. This is the *slowly evolving wave approximation* and is valid when the pulse duration is much longer than the period of the carrier wave **or** the group and phase velocity are similar [9].

As an alternative to the fields, one can described an EM wave using the vector and scalar potentials [10]. In the Coulomb gauge the scalar potential is

$$\phi(\boldsymbol{r},t) = \frac{1}{4\pi\epsilon_0}\int \frac{\rho(\boldsymbol{r}',t)}{|\boldsymbol{r}-\boldsymbol{r}'|}\mathrm{d}^3\boldsymbol{r}' \tag{1.4}$$

and for a travelling wave when no sources are present $\phi = 0$. Then the fields are given by

$$\boldsymbol{E} = -\frac{\partial \boldsymbol{A}}{\partial t} \tag{1.5}$$

$$\boldsymbol{B} = \nabla \times \boldsymbol{A} \tag{1.6}$$

where $\boldsymbol{A}(\boldsymbol{r}, t)$ is the vector potential. The use of the Coulomb gauge amounts to defining the vector potential such that $\nabla \cdot \boldsymbol{A} = 0$ and other definitions are possible [10]. However, any gauge definition must leave the fields (1.5) and (1.6) unaffected. The Coulomb gauge is only one possible definition of an EM wave.

Many atomic, molecular and optical (AMO) physics problems can be simplified by noting that the atomic scale is much smaller than the optical wavelength. Hence $kz \approx 0$ and the oscillating terms are simplified. In addition, the magnetic field of an EM wave is smaller than the electric field by a factor $1/c$ and is often ignored. These two simplifications constitute the electric dipole approximation. We use it frequently throughout this work, however, we will encounter some situations where it is not valid. Saying that a quantity is small is different from saying it does not exist. And if it is small or large, or important or negligible largely depends on the sensitivity of your experiment and what you are interested in.

1.2 Charged Particles in an Oscillating Light Wave

Imagine a free particle with mass m and charge q appears at the instant t_i in the wave described by Eq. (1.1). Later on we will consider how it is produced (ionization), but for now we focus on its dynamics after ionization [11].

The equation of motion for the particle is

$$\gamma m \ddot{\boldsymbol{r}} = q\boldsymbol{E}\left(\boldsymbol{r}, t\right) + q\dot{\boldsymbol{r}} \times \boldsymbol{B}\left(\boldsymbol{r}, t\right) \tag{1.7}$$

where $\gamma = 1/\sqrt{1 - v^2/c^2}$. Eq. (1.7) is solvable using Hamilton-Jacobi theory [12, 13]. To simplify the analysis and illustrate the underlying dynamics we make the following assumptions: (1) consider the non-relativistic limit $\gamma \approx 1$, (2) make the electric dipole approximations and the slowly evolving wave approximation, and (3) treat the magnetic field (i.e. the second term in Eq. (1.7)) as a perturbation on the motion due to the electric field. Based on these assumptions, we have the first order solutions to the particle's momentum and position:

$$\begin{aligned}
\boldsymbol{p}^{(1)}(t) &= \frac{qE_0}{\omega} f(t)\left[(\sin\omega t - \sin\omega t_i)\,\hat{\imath}\right. \\
&\qquad\qquad \left. -\,\epsilon\,(\cos\omega t - \cos\omega t_i)\,\hat{\jmath}\right] + \boldsymbol{p}_i \qquad (1.8) \\
\boldsymbol{r}^{(1)}(t) &= \frac{qE_0}{m\omega^2} f(t)\left[-\left(\cos\omega t - \cos\omega t_i + \omega(t-t_i)\sin\omega t_i\right)\hat{\imath}\right. \\
&\qquad \left. -\epsilon\left(\sin\omega t - \sin\omega t_i - \omega(t-t_i)\cos\omega t_i\right)\hat{\jmath}\right] \\
&\qquad\qquad +\boldsymbol{p}_i(t-t_i) + \boldsymbol{r}_i \qquad (1.9)
\end{aligned}$$

where $\boldsymbol{p}_i$ and $\boldsymbol{r}_i$ are the particle's initial momentum and position. For now we set these equal to zero. In section 3.3 we will see that the conservation of photon momentum requires that $\boldsymbol{p}_i$ is non-zero. Whenever energy is absorbed from an EM wave (ionization), there must also be momentum absorbed [14]. This comes from the second order interaction with the magnetic field. Then in section 3.4 we will examine how the conservation of angular momentum may give insight into a non-zero value for $\boldsymbol{r}_i$.

It's often useful to compare a measured energy in an experiment to the energy of the corresponding free particle averaged over one cycle in the oscillating EM wave. This is it's ponderomotive energy,

$$\begin{aligned}
U_p &= \frac{\langle|\boldsymbol{p}|^2\rangle}{2m} \\
&= \frac{q^2E_0^2}{4m\omega^2}\left(1+\epsilon^2\right) \ . \qquad (1.10)
\end{aligned}$$

It's worth emphasizing that the ponderomotive energy depends on the polarization of the EM wave.

1.2.1 Linear and Circular Polarization

Let's examine in more detail the trajectory of the particle described by the classical equations of motion (1.8) and (1.9). According to Eq. (1.8) the particle's motion is characterized by a fast oscillation at the optical frequency along with a constant drift momentum. In a linearly polarized wave ($\epsilon = 0$) a particle that appears before the peak of an optical cycle travels far enough away in the first half-cycle that it never returns to the origin (see

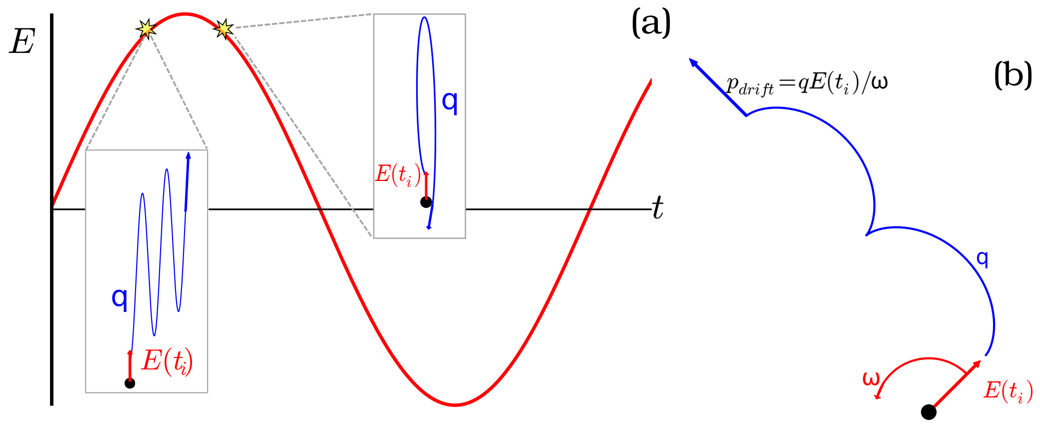

Figure 1.2: Classical trajectories of charged particles in EM waves shown in blue. (a) linearly polarized light, (b) circularly polarized light. In linear polarization a particle that appears before the peak of the optical cycle (inset, far left) never returns to it's exact origin. A particle that appears after the peak (inset, centre) does return. In a circularly polarized pulse (b), the classical trajectory follows a cycloid. The particle's asymptotic momentum is perpendicular to the polarization vector at ionization.

Fig. 1.2a). A particle that appears after the peak of the optical wave is initially accelerated away from the origin, but later returns to it's location of birth with considerable kinetic energy. These are the re-scattering particles we will consider in section 1.2.2.

In circularly polarized light ($\epsilon = 1$), the particle's trajectory follows a cycloid. This is shown in Fig. 1.2b. The drift momentum is perpendicular to the direction of the electric field at ionization $\boldsymbol{E}(t_i)$. The direction of $\boldsymbol{p}_d$ rotates 2π in one optical cycle: 2.7 fs using 800 nm light. Hence, measurement of the momentum distribution in near-circularly polarized, few-cycle laser pulses offers a method to measure attosecond dynamics termed attosecond angular streaking [15, 16]. The magnitude of the drift momentum follows the pulse envelope $f(t)$ and provides a coarse time scale. The direction of the measured momentum vector follows the rotating electric field and provides a fine scale. These two time scales have been compared to the minute and second hands on a clock [17].

For any value of ϵ, the fast oscillation disappears as the laser pulse passes and the pulse envelope $f(t) \to 0$. The terms that oscillate in Eqs. (1.8) and

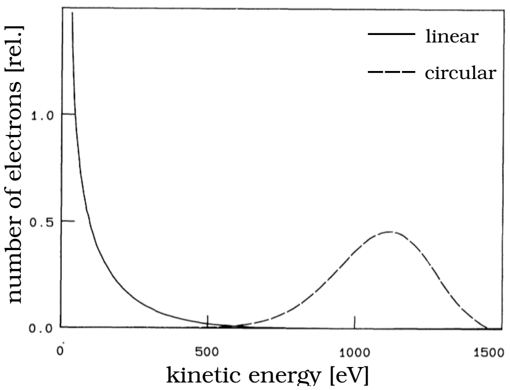

Figure 1.3: Calculated photo-electron kinetic energy distributions in linear (1×10^{14} W/cm^2) and circular (2×10^{14} W/cm^2) polarization at $\lambda = 10$ μm. Taken from [11].

(1.9) vanish and the asymptotic momentum is

$$\boldsymbol{p}_d = \frac{qE_0}{\omega} f(t_i)\left[-\sin\omega t_i\ \hat{\imath} + \epsilon\cos\omega t_i\ \hat{\jmath}\right] + \boldsymbol{p}_i\ . \tag{1.11}$$

In attosecond physics the charged particle is almost always an electron ionizing from an atom or molecule. By using circularly polarized light we can immediately move the electron away from the parent ion. Circular polarization is therefore ideal for isolating the ionization process and avoiding the residual Coulomb interaction between the photo-electron and parent nucleus. We will use this property to study the photo-electron momentum distribution at ionization in section 3.1. Furthermore, Eq. (1.11) shows the magnitude of the drift momentum is independent of phase in circularly polarized light. There is a simple relationship between the drift momentum, laser frequency and field strength at ionization: $p_d = qE_0 f(t_i)/\omega$. In section 3.2 we exploit this relationship to make a high precision measurement of the laser field at ionization.

In circular polarization the asymptotic kinetic energy is the same for all phases of ionization: $K = p_d^2/(2m) = U_p$. In linear polarization the asymptotic kinetic energy is

$$K = \frac{q^2 E_0^2 f^2(t_i)}{2m\omega^2}\sin^2\omega t_i \tag{1.12}$$

and has the maximum value $K_{max} = 2U_p$ when $\omega t_i = \pi/2$. Those particles will be interesting because they have ionized when the field (1.1) passes through zero. Examples of calculated kinetic energy spectra are shown in Fig. 1.3.

1.2.2 Re-collision Phenomena

Re-collision is the fundamental physical concept in attosecond science [18]. It gives rise to a variety of different ultrafast phenomena. An electron that ionizes and is driven back upon it's parent nucleus can interfere with the remaining charge and emit an XUV attosecond pulse [19, 7]. This high-harmonic generation is currently a very active research area, both as a source of attosecond pulses [7, 20] and as a probe of atomic and molecular structure itself [21, 22]. However, high harmonic generation is not the subject of this work.

Instead of emitting XUV radiation, the re-colliding electron can scatter off the parent nucleus – either elastically, carrying away structural information of the ionic charge distribution [23, 24, 25], or inelastically, leading to the emission of a second electron [26, 27, 28].

In addition to these high energy re-scattering processes, there are also low energy collisions. Soft collisions that occur during a portion of the optical cycle do not lead to the emission of high energy electrons or XUV photons, however, they are very much a part of attosecond science. During soft collisions the photo-electron interacts with the parent ion, leading to a deformation of the electron momentum distribution [29, 30] and prominent low energy features [31]. After the pulse has passed and the oscillatory motion disappears the low energy electrons can be recaptured into highly excited levels of the neutral atom or molecule [32, 33].

Re-collision phenomena can occur with a small ellipticity [32, 34], however, the re-scattering current density is largest with linear polarization. Let's therefore use the classical physics from section 1.2 to model the re-collision kinematics in linearly polarized light. From Eq. (1.9) we see that the condition for re-collision is

$$0 = \cos \omega t_R - \cos \omega t_i + \omega(t_R - t_i) \sin \omega t_i \tag{1.13}$$

where t_R is the re-collision time. One can solve this expression numerically. However, the solution is well-described by the function [35]

$$\omega t_R = \frac{\pi}{2} - 3 \arcsin\left(\frac{2}{\pi}\omega t_i - 1\right) \ . \tag{1.14}$$

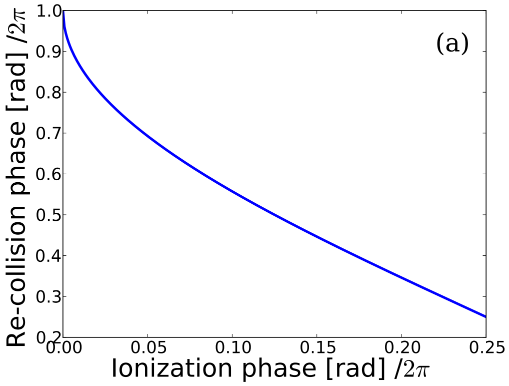

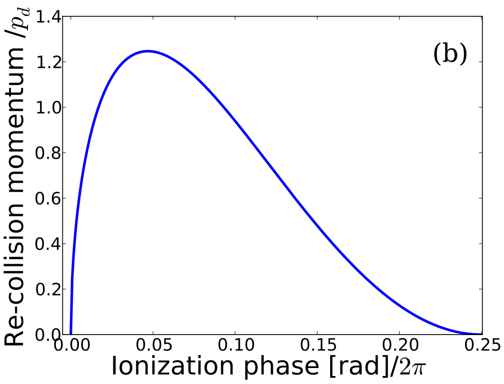

Figure 1.4: (a) Re-collision phase as a function of ionization phase Eq. (1.14). (b) Re-collision momentum as a function of ionization phase Eq. (1.15). The y-axis is normalized by the drift momentum $p_d = qE_0/\omega$.

The momentum at re-collision is found from Eq. (1.8)

$$p_R = \frac{qE_0}{\omega}\left[\cos\left(3\arcsin\left(\frac{2}{\pi}\omega t_i - 1\right)\right) - \sin\omega t_i\right]. \tag{1.15}$$

The functions (1.14) and (1.15) are plotted in Fig. 1.4. From (1.15) we find that the maximum kinetic energy at re-collision is $K_{max} = 3.17U_p$ [18]. The re-scattering process creates a mapping of time into energy, however, we observe in Fig. 1.4 that the mapping is not unique. Each momentum corresponds to two different re-collision phases. These are the so-called short and long trajectories. The redundancy is overcome in certain experiments like high-harmonic generation by experimentally separating the two re-collision phases spatially. The different re-collision phases produce harmonic beams having different divergence, thus appearing at a different position on a detector [36].

From Fig. 1.4 we note that re-scattering occurs over only a fraction of the optical cycle. Hence re-scattering gives experimental access to the attosecond time domain using infrared laser pulses. Of course, once the particle re-collides the story doesn't end. The laser field is still present and can continue to drive the motion. Multiple re-collisions are possible, although the re-scattering current density is highest at the first re-collision [34, 37]. Furthermore, particles that elastically back-scatter off the origin are again accelerated by the EM wave and receive an additional qE_0/ω boost in momentum. Hence the backward scattered particles contain the maximum possible kinetic energy $K_{max} \approx 10U_p$. This is clearly much larger than the maximum possible kinetic energy in the absence of re-scattering from Eq. (1.12).

1.3 Strong Field Ionization

The discussion thus far has focused on the dynamics of free particles that appear in EM waves. Let's now turn to the mechanism that produces them – ionization. Although the preceeding work applies to any particle of mass m and charge q, we now focus on the ionization of electrons from atoms and molecules, since this is of paramount importance for attosecond science. We use atomic units throughout this section. Atomic units are defined by setting $e = \hbar = m_e = 4\pi\epsilon_0 = 1$ [38, 39]. Without an ultrafast process to create the free electrons, it would be impossible to use re-collision as an attosecond probe. Strong field ionization by infrared laser pulses functions as a trigger to enable attosecond pulse generation [18] and initiate ultra-fast charge migration in atoms [40, 41] and molecules [42, 43].

To model multi-photon ionization of an atom we first write the Schrödinger equation for an electron in the presence of a nucleus and external EM wave,

$$i\frac{\partial}{\partial t}\Psi(\boldsymbol{r},t) = \hat{H}\Psi(\boldsymbol{r},t) \tag{1.16}$$

where $\hat{H}$ is the Hamiltonian and is given by

$$\begin{aligned} \hat{H} &= \frac{1}{2}\left(\hat{\boldsymbol{p}} - \boldsymbol{A}\right)^2 + \phi(r) && (1.17) \\ &= \hat{H}_0 - \boldsymbol{A}\cdot\hat{\boldsymbol{p}} + \frac{1}{2}\boldsymbol{A}^2 && (1.18) \end{aligned}$$

where $\hat{\boldsymbol{p}}$ is the momentum operator and $\phi(r)$ is the potential binding the electron to the nucleus. In general $\phi(r)$ depends on the nuclear charge and the positions of all other electrons in the atom. Note that by using the Schrödinger equation we are ignoring electron spin and other relativistic effects. In the non-relativistic limit it is also valid to drop the term $\propto A^2$ in (1.18). The term $\hat{H}_0$ is the atomic field-free Hamiltonian,

$$\hat{H}_0 = \frac{\hat{\boldsymbol{p}}^2}{2} + \phi(r)\ . \tag{1.19}$$

Eq. (1.18) can be made to appear in different forms by adopting different gauge transformations of the vector and scalar potentials, and the wavefunction [44]. We do not derive the transformation here, but state the main results. The velocity-gauge Hamiltonian is

$$\hat{H} = \hat{H}_0 - \boldsymbol{A} \cdot \hat{\boldsymbol{p}} \ , \tag{1.20}$$

and the length-gauge Hamiltonian reads

$$\hat{H}' = \hat{H}_0 - \boldsymbol{E} \cdot \hat{\boldsymbol{r}} \ . \tag{1.21}$$

The wavefunction in the length gauge Ψ' is related to the wavefunction in velocity gauge Ψ by [44]

$$\Psi'(\boldsymbol{r}, t) = \Psi(\boldsymbol{r}, t) \exp\left(i\boldsymbol{A} \cdot \boldsymbol{r}\right) . \tag{1.22}$$

Since any physical system is unaffected by a gauge transformation, the velocity and length gauge Hamiltonians should give identical results. In practice, calculations can be affected by approximations for the potential function $\phi(r)$.

1.3.1 Tunnel Ionization

By examining the length-gauge Hamiltonian, we can see that the interaction of the strong laser field with the atomic system introduces a deformation to the Coulomb potential binding the valence electrons to the nucleus. In femtosecond, infrared laser pulses the external field strength can approach or exceed the Coulomb force binding the valence electrons. The modified potential then takes the form of a barrier that the electron can tunnel through [45]. This is sketched in Fig. 1.5.

Tunnelling is a very general phenomenon in quantum mechanics. Several applications of tunnelling have been recognized with Nobel Prizes. It was originally introduced to explain DC phenomena like nuclear decay [46]. Tunneling was also used by Giaver (Nobel Prize 1973) to study the density of states in a superconductor [47], and it is the foundation behind the Scanning Tunnelling Microscope (Nobel Prize 1986) [48, 49, 50]. The feature that makes tunnelling a powerful tool in such diverse areas is it's high sensitivity. The tunnelling rate depends exponentially on the height and length of the potential barrier, and incident particle energy. Hence any applications where these parameters can change will see large changes in the tunnelling signal.

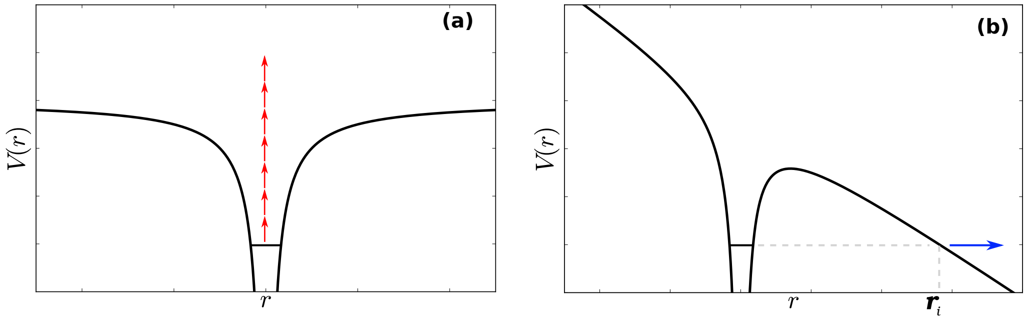

Figure 1.5: (a) Multi-photon ionization in the perturbative regime $\gamma \gg 1$. A bound electron is promoted to the continuum via absorption of many photons from the field. (b) Multi-photon ionization in the tunnelling limit $\gamma \ll 1$. The Coulomb potential confining the valence electron is distorted by the external laser field. The electron can tunnel through the barrier into the continuum at position $\boldsymbol{r}_i$ where it is free.

In an oscillating laser field, tunnelling will be possible if the time for the electron to travel the length of the barrier is much shorter than the time for the EM field to change direction. Taking the ratio of these two quantities yields the Keldysh parameter:

$$\gamma = \omega\tau = \frac{\omega}{E}\sqrt{2I_p} \tag{1.23}$$

where I_p is the electron's binding energy (ionization potential). Eq. (1.23) is in atomic units ($e = \hbar = m_e = 4\pi\epsilon_0 = 1$) [38, 39]. For $\gamma \ll 1$ ionization is well described by tunnelling. For $\gamma \gg 1$, light-matter interaction is perturbative. Most contemporary strong field experiments with near infrared lasers are done in a regime where $\gamma \approx 1$, making it difficult to know which model to use. Even in this intermediate regime, tunnelling models often succeed very well at quantitatively describing ionization rates [51], photo-electron momentum distributions [52, 37], and light absorption [53] in infrared laser fields. An upper limit on the laser field in tunnelling is given by over-barrier ionization,

$$E_{OB} = \frac{I_p^2}{4Z} \ . \tag{1.24}$$

Several intensities associated with over-barrier ionization of noble gas atoms are listed in table 1.1. Above E_{OB} the electron no longer can be thought

Atom	$\mathbf{I_p}$ **(eV)**	$\mathbf{E_{OB}}$ **(a.u.)**	$\mathbf{I_{OB}}$ (W/cm^2)
Xe	12.1	0.049	1.7×10^{14}
Ar	15.7	0.083	4.9×10^{14}
Ne	21.6	0.158	1.7×10^{15}
He	24.6	0.204	2.9×10^{15}

Table 1.1: Threshold intensities for over-barrier ionization in circularly polarized light.

of as tunnelling. Nonethless, quantum mechanical effects like non-classical reflection should still be present even for fields greater than E_{OB}.

Let an electron occupy a bound orbital with principal quantum number n, angular momentum quantum number l and magnetic quantum number m. The adiabatic tunnel ionization rate (in atomic units) is given by [35, 54]

$$W_{l,m}(E) = |C_{n^*,l^*}|^2 G_{l,m} I_p \left(\frac{2\left(2I_p\right)^{3/2}}{E} \right)^{2n^*-|m|-1} \times \exp\left(-\frac{2\left(2I_p\right)^{3/2}}{3E} \right) \quad (1.25)$$

where $n^* = Z/\sqrt{2I_p}$ is the effective principal quantum number and $l^* = n^* - 1$ is the effective orbital quantum number. For single ionization $Z = 1$. The prefactors are given by,

$$|C_{n^*,l^*}|^2 = \frac{2^{2n^*}}{n^*\Gamma\left(n^* + l^* + 1\right)\Gamma\left(n^* - l^*\right)} \quad (1.26)$$

$$G_{l,m} = \frac{\left(2l+1\right)\left(l+|m|\right)!}{2^{|m|}|m|!\left(l-|m|\right)!} \quad (1.27)$$

where $\Gamma(x)$ is the gamma function [55]. The tunnelling rate is an exponential function of the laser field E and of the binding energy I_p. This behaviour can be understood physically by recalling that the transmission rate for a particle of wavenumber k through a barrier of length d scales with $\exp\left(-2\int_0^d k(x)\mathrm{d}x\right)$ [56]. In the context of tunnel ionization of an atom by a laser field we have $d \approx I_p/E$ and $k \approx \sqrt{2(I_p - Ex)}$.

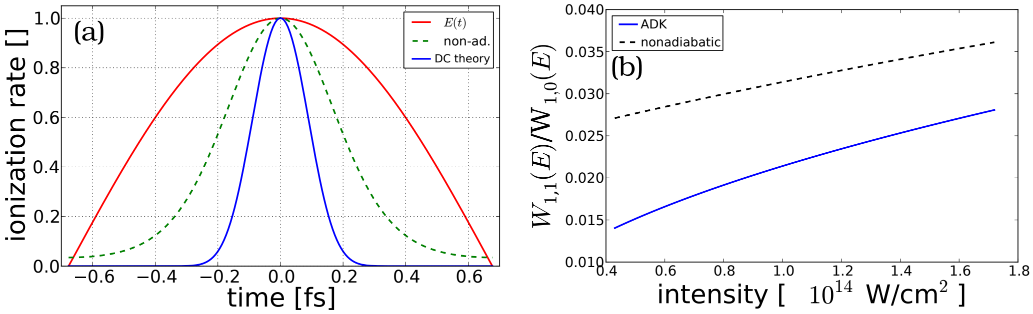

Figure 1.6: (a) Non-adiabatic effects change the subcycle ionization rate in linearly polarized light for Ar at 800 nm and 4×10^{13} W/cm^2. The DC tunnelling theory calculated from Eq. (1.25) is plotted in blue. The non-adiabatic rate is the dashed green line. Also shown in red is the laser field. (b) Non-adiabatic effects enhance ionization from orbitals unaligned to the laser polarization. The ratio of ionization from the $m = 0$ orbital (aligned with polarization axis) to the $|m| = 1$ orbitals is shown for Ar at 800 nm.

The total ionization probability for the atom is

$$p(t) = 1 - \exp\left(-\int_{-\infty}^{t} W\left(E(t')\right) \mathrm{d}t'\right) \tag{1.28}$$

which should include integration over the optical cycle and laser pulse envelope. In an experiment, there is also spatial integration as well, which we cover in more detail in Chapter 3.

We also note that the rate (1.25) depends very sensitively on the azimuthal quantum number m. This means that in rare gases (with the exception of helium) 97-98 % of the ionization signal comes from the electrons in the $m = 0$ orbital, i.e. the orbital aligned with the laser polarization axis. In Fig. 1.6 we have plotted the ratio of the ionization rate from $|m| = 1$ to the rate from $m = 0$. The contribution from $|m| = 1$ can be slightly enhanced due to non-adiabatic effects. In section 3.1.1 we show how the tunnel ionization dependence on m can lead to observable consequences on the photo-electron momentum distribution.

Non-adiabatic effects refer to changes in the tunnel barrier during the particle's interaction with the barrier. This can occur when the laser period is comparable to the classical time for the electron to cross the barrier $\gamma \approx 1$. As we noted, this is the condition of almost all contemporary experiments

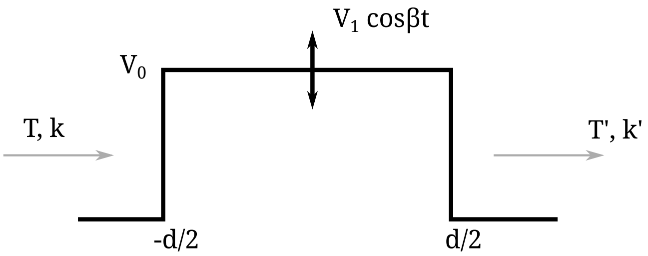

Figure 1.7: Idealized system for modelling non-adiabatic tunnelling [57]. An incident particle with wavenumber k and energy T tunnels through a potential barrier of height $V_0 \gg T$. The barrier oscillates with small amplitude V_1 at frequency β. The energy of the transmitted particle can be modified by interaction with the oscillating barrier.

with femtosecond, near IR light. An elegant model system for understanding the co-existence of tunnelling and perturbative features comes from Büttiker & Landauer [57].

Consider an incident particle of energy T and wavenumber k on a barrier of height V_0 and length d (see Fig. 1.7). The barrier is modulated by a small amplitude V_1 and frequency β and we assume that $T \ll V_0 - V_1$. In this ideal situation the oscillation of the barrier is decoupled from the tunnelling problem. The issue is, how does the periodic modulation of the barrier affect the tunnelling behaviour?

If the barrier oscillation is slow with respect to the time of interaction, then the tunnelling particle sees a static barrier and the tunnelling rate is given by the instantaneous barrier height $V(t) = V_0 + V_1 \cos \beta t$. Sidebands in the tunnelling particle spectrum appear at equal amplitude at energy $T \pm \hbar\beta$. However, if the barrier oscillation is rapid with respect to the interaction time, then the particle sees a time averaged barrier and can absorb quanta during tunnelling. In this case the sidebands appear with unequal amplitudes. A particle that absorbs $\hbar\beta$ sees a smaller barrier and therefore has a larger transmission rate. Since the wavefunction amplitude decreases exponentially with the penetration into the barrier, those particles that absorb at $x \approx -d/2$ will dominate the tunnelling signal. Similarly, a particle that emits $\hbar\beta$ sees a larger barrier and those particles that emit close to the exit of the barrier $x \approx d/2$ will dominate the signal. The transition from equal sideband amplitude to unequal amplitude was used in Ref. [57] as an operational definition for tunnelling time. Since the barrier always exists the problem is always tunnelling and the transition from a static to rapidly oscillating barrier is continuous.

With regard to laser tunnelling, we expect similar behaviour to exist in the transition regime $\gamma \approx 1$. That is, it is possible for tunnelling electrons to absorb quanta while interacting with the barrier. Similar to the case above, these electrons will appear at sidebands with respect to their incident kinetic energy. However, in laser tunnelling the barrier modulation frequency is identical to the overall ionization frequency. In the context of the scattering problem discussed above, this is like sending a new particle to the barrier at a time interval $2\pi/\beta$. Of course this introduces another periodicity in the spectrum and unfortunately it overlaps exactly with the sidebands one expects from modulation of the potential barrier. This is the situation we face in laser tunnelling.

Theory for non-adiabatic tunnelling in the context of laser ionization exists. The non-adiabatic ionization rate has a closed form expression which we do not reproduce here [58, 59]. The non-adiabatic rate is less sensitive than the DC tunnelling rate (1.25) to the phase of a linearly polarized wave and may be non-zero even when the classical field is passing through zero. See Fig. 1.6 for a comparison between the two theories. The difference also extends to the m dependence. The relative contribution from $|m| = 1$ using the non-adiabatic rate is always larger than the contribution using DC tunnelling. In general non-adiabatic effects allow for ionization when the barrier is larger, i.e. when the laser field has not reached it's maximum, or for ionization from $|m| = 1$ orbitals. Very recently there is some work studying the role of the sign of m (positive or negative) [60]. This dependence is not considered in either the DC or non-adiabatic tunnelling theories.

Using tunnelling to model strong field ionization by EM waves requires several assumptions: (a) the ionizing electron adiabatically follows the oscillating electric field, (b) only a single electron responds to the field, (c) the electric dipole approximation is valid (no relativistic effects), (d) the length gauge. We have noted how newer theories correct for non-adiabatic effects. The single active electron approximation works very well to model ionization of atoms [61] and small molecules [62]. It's even possible to model ionization of inner orbitals using this approach [63]. However the single electron approximation breaks down for transition metal clusters [64, 65] and larger molecules [66, 67]. Correlated detection of electron and ion offers one possible method to handle multi-electron effects experimentally [68]. The electric dipole approximation is widely used, although we will discuss observations on non-dipole effects in Chapter 3. Although a photo-electron can be accelerated to relativistic velocities *after* ionization, the tunnelling ansatz says that it appears at the edge of the barrier with close to zero kinetic energy. Hence a non-relativistic treatment for valence orbital ionization is sensible. Lastly, as we have noted, physical systems are gauge independent. Although there is no potential barrier *per-se* in velocity gauge or others, tunnelling is a useful tool for interpreting observations and guiding intuition for strong field light-matter interactions. It's quantitative successes are largely the reason for it's widespread use.

1.3.2 Momentum Distributions

The sensitive dependence of the tunnelling rate on the size of the potential barrier places limits on the momentum distribution of the tunnelled photo-electron. The momentum distribution and it's connection to re-scattering processes has been studied via ellipticity scans [32, 34]. However, using circularly polarized light, the lateral momentum distribution can be measured directly [69].

The portion of the electron wavepacket that ionizes with a lateral momentum $p_\perp$ must absorb extra energy from the laser field. This is because the momentum in the lateral direction is not useful for ionization. Hence, the lateral momentum represents an elevated barrier for the electron to overcome. The modified barrier height is $I_p' = I_p + p_\perp^2/2$. Inserting this into Eq.(1.25) gives the ionization rate dependence on the lateral momentum [70]

$$W(p_\perp) = W(0)\exp\left(-p_\perp^2 \frac{\sqrt{2I_p}}{E}\right) \tag{1.29}$$

where $W(0)$ is a prefactor independent of $\boldsymbol{p}$. Eq. (1.29) represents a prediction on the lateral momentum distribution in the adiabatic limit. Non-adiabatic theory suggests that the corrections to tunnelling should make the net lateral distribution wider [71]. However, experiment did not show a significant wavelength dependence in the regime $\gamma \approx 1$ [69], and simulations found that non-adiabatic effects can narrow the lateral wavepacket [72]. Recently, theoretical investigation has focused on the pre-exponential factor in Eq. (1.29) and shown better agreement with measured values [73].

The momentum distribution of the tunnelled electron along the polarization axis is more difficult to observe. This is because immediately upon ionization, the strong laser field drives the electron in the same direction as it has ionized. For small ellipticity ($\epsilon < 0.2$) both the lateral and longitudinal distributions must be distorted by re-scattering and Coulomb interaction with the nucleus. In near-circular polarization the longitudinal distribution maps onto the azimuthal position in the momentum-space torus [74]. Since ionization occurs for any phase of the laser field in circularly polarized light, the momentum distribution along this direction is convolved with the angle-dependent ionization rate.

$$W(p_{\|}) \propto \exp\left(-p_{\|}^2 \frac{\gamma^3}{3\omega}\right) = \exp\left(-p_{\|}^2 \frac{\omega^2 (2I_p)^{3/2}}{3E^3}\right) \tag{1.30}$$

which suggests that the free-electron wavepacket has equal probability to be initially moving toward the barrier (in reverse from the direction that it tunnelled) as it does to move away from the barrier. This counter-intuitive result was not supported by calculations [75], however, recent experiments supplemented by simulation have shown some results consistent with Eq. (1.30) [76]. There remain open questions with regard to the longitudinal momentum distribution in the tunnelling limit.

The longitudinal momentum spread (1.30) represents an intrinsic limit on the time resolution of attosecond angular streaking [16]. Two events separated by a time interval τ will map onto an angular separation $\Delta\theta = \omega\tau$ in the photo-electron momentum distribution using circularly polarized light. Assuming that the laser field is unchanged during this interval, Eq. (1.30) shows each event will have a corresponding uncertainty in the longitudinal momentum $\sigma_{\|} = \sqrt{3E^3/\omega^2(2I_p)^{3/2}}$. When the momentum distributions originating from two different phases overlap too much, they will be indistinguishable by direct observation[1]. This places a limit on the minimum time resolution of angular streaking via tunnel ionization,

$$\tau = \left(\frac{6E}{\omega^2 (2I_p)^{3/2}}\right)^{1/2} . \tag{1.31}$$

At 800 nm for ionization of Ne in 10^{15} W/cm^2, this corresponds to 250 attoseconds. This represents the minimum time resolution of a direct observation via the photo-electron momentum distribution. If one has *a priori*

---

[1] Mathematically, one can take the sum of two Gaussian distributions and find the separation between them where the net distribution has only two inflection points. The value for the separation is $\sigma\sqrt{2}$ where σ is the standard deviation of each distribution.

knowledge of the underlying physics it should be possible to improve on this by fitting. In addition, angular streaking by an infrared pulse could be combined with attosecond pulses to provide finer time resolution. In this case the limitation would be from the momentum distribution of ionization via an attosecond pulse. The corresponding time resolution is then $\tau = \sigma_{\parallel}\sqrt{2}/E$ where $\sigma_{\parallel}$ is the standard deviation of the longitudinal momentum distribution from attosecond pulse ionization and E is the electric field of the infrared streaking pulse.

The preceding analysis pays little attention to the bound orbital the electron is tunnelling out of. In the last decade, however, it has become clear that this affects ionization rates [62, 77] and photo-electron angular distributions [78, 63, 79]. One of the first attempts was made by Ivanov *et al* [80] who introduced the bound state as a quantity in the pre-exponential factor:

$$\Phi'_{n,l,m}(p_{\perp}) = \Phi_{n,l,m} \exp\left(-p_{\perp}^2 \frac{\sqrt{2I_p}}{2E}\right) \tag{1.32}$$

where $\Phi_{n,l,m}$ is the bound momentum distribution. Ref. [73] gives a formal derivation illustrating the role of the bound state in tunnel ionization. Eq.(1.32) suggests that tunnelling acts as a filter on the bound momentum distribution, removing the large lateral momentum portion of the bound distribution. This has implications for atomic and molecular imaging using laser tunnelling. Since the tunnel filter is always much narrower than the bound momentum distribution, large lateral momentum values do not pass through it. In molecules, one can skirt the problem by rotating the molecule with respect to the ionizing field [63, 77]. But at any particular angle a portion of the bound distribution always remains unobserved.

1.3.3 What is a Strong Field?

When discussing the behaviour of matter in strong fields, we normally assume that everyone already knows what we mean by “strong”. But what is it? The definition “approaching the field strength binding atoms and molecules” is vague. Another approach is offered by Delone & Krainov [81]. They build around the idea of above-threshold ionization (ATI) [82]. In ATI, an electron makes a transition from a bound state $|i\rangle$ to a continuum state $|f\rangle$ via the absorption of n photons. The photo-electron spectrum consists of a series of

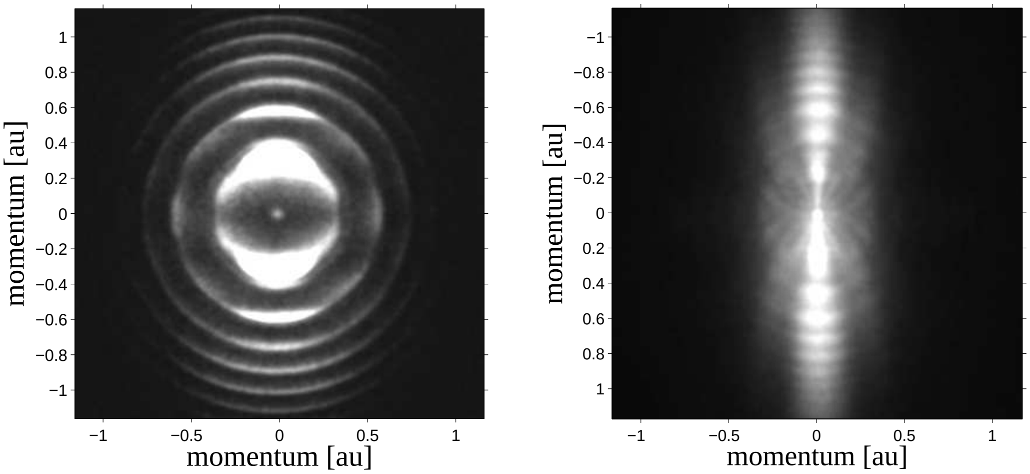

Figure 1.8: Measured ATI spectra from argon. (left) 400 nm; (right) 800 nm. The laser propagates left-right and the polarization is along the vertical axis in the images. Photo-electrons appear at a comb of discrete kinetic energies Eq. (1.33) where the comb spacing equals the photon energy.

discrete peaks at the kinetic energy

$$K = n\hbar\omega - I_p - U_p \tag{1.33}$$

where n is the integer number of photons absorbed.

ATI allows us to give a more precise definition to a strong field. According to Delone and Krainov, a strong field is one where absorption of n photons is equally likely as absorption of $n+1$ photons. The n photon ionization rate is [81]

$$W^{(n)} = \sigma^{(n)}\frac{E^{2n}}{\omega^n} \tag{1.34}$$

where $\sigma^{(n)}$ is the n photon cross-section. Setting $W^{(n+1)}/W^{(n)} = 1$ gives a critical field strength $E_c \approx 5 \times 10^7$ V/cm which corresponds to 3×10^{12} W/cm^2. This is much less than the atomic field strength, $E_a = 5.1 \times 10^9$ V/cm. Thus, a strong field is one which produces an ATI photo-electron spectrum where each succesive peak is roughly equal in probability to the preceding peak. Examples of ATI at $\sim 1 \times 10^{14}$ W/cm^2 are shown in Fig. 1.8.

In Fig. 1.8 the laser propagates left-right and the polarization axis is along the vertical direction of the page. We observe that the photo-electrons are emitted in a series of concentric rings spaced by the photon energy. The rings at 800 nm are more tightly confined to the polarization axis, whereas at 400 nm the rings have a broader angular distribution. This is because fewer photons are needed to ionize at shorter wavelength. The electron makes a transition from the valence 3p orbital in Ar to a continuum state with a particular energy and angular momentum. Since each photon absorbed carries an angular momentum of $\pm\hbar$, absorbing more photons corresponds to a higher angular momentum and therefore a more narrow angular distribution. Note that at both wavelengths many ATI peaks are observable, indicating that the measurement is done with a "strong field".

Further evidence of the photon angular momentum appears in the photoelectron angular distribution at 400 nm shown on the left in Fig. 1.8. Each successive ring in the ATI spectrum has either a node along the horizontal axis (local minimum in the electron signal) or an anti-node (local maximum). This behaviour mirrors the change in spherical harmonic functions which oscillate between a local minimum in the perpendicular direction (p_z, f_{z^3}, etc.) or local maximum in the perpendicular direction (s, d_{z^2}, etc.) with the addition of one unit of angular momentum. Since the angular wavefunction of the photo-electron is described by a spherical harmonic, the observed oscillation corresponds to absorption of an additional one unit of angular momentum. Such effects are more difficult to observe at 800 nm due to re-scattering effects [37, 52].

1.4 Atomic Units in Optics

Atomic units are very useful in ultrafast physics since most of what we study is on the atomic scale and it simplifies equations. Atomic units are defined by setting $e = \hbar = m_e = 4\pi\epsilon_0 = 1$ [38, 39]. On the other hand, the laser community has historically quoted parameters like pulse length, pulse energy, wavelength and intensity in SI units. Although in many cases the conversion is trivial, there remains considerable confusion surrounding intensity. While it is perfectly reasonable to speak of an atomic unit of length or electric field, it is not clear what is meant by an atomic unit of intensity. Isolated atoms have no intensity. One can try to avoid this issue by first finding what an atomic unit of electric field is and then calculating the laser intensity corresponding to this field strength. A 1s electron in hydrogen feels an electric field (in SI units)

$$\begin{aligned} E &= \frac{e}{4\pi\epsilon_0 a_0^2} \\ &= \frac{(1.6022 \times 10^{-19}\ \mathrm{C})}{4\pi(8.8542 \times 10^{-12}\ \mathrm{F/C})\ (5.2918 \times 10^{-11}\ \mathrm{m})^2} \\ &= 5.1422 \times 10^{9}\ \mathrm{V/cm} \end{aligned}$$

where a_0 is the Bohr radius. The laser intensity corresponding to this field strength (in SI units) is

$$\begin{aligned} I &= \frac{1}{2} c\epsilon_0 E^2 \\ &= \frac{1}{2}(2.9979 \times 10^{8}\ \mathrm{m/s})\ (8.8542 \times 10^{-12}\ \mathrm{F/C})\ (5.1422 \times 10^{9}\ \mathrm{V/cm})^2 \\ &= 3.5094 \times 10^{16}\ \mathrm{W/cm^2}\ . \end{aligned} \tag{1.35}$$

Many people take this as the atomic unit of intensity. It is immediately clear that something is amiss, however, since (1.35) assumes a linearly polarized laser beam. If it were circularly polarized, the atomic unit of intensity would have twice this value. Writing (1.35) in terms of the atomic units gives

$$I = \frac{1}{2}(137.04)\ \left(\frac{1}{4\pi}\right)\ (1\ \mathrm{a.u.})^2 \quad = 5.4527\ \mathrm{a.u.}$$

So a linearly polarized wave with one atomic unit peak electric field strength has an intensity of 5.453 atomic units. This means the atomic unit of intensity is

$$I_{au} = \frac{3.5094 \times 10^{16}}{5.4527} = 6.4364 \times 10^{15}\ \mathrm{W/cm^2}\ .$$

One can also construct an intensity using the fundamental constants of atomic units,

$$I_{au} = \frac{E_H}{t_{au} a_0^2} = 6.4364 \times 10^{15}\ \mathrm{W/cm^2}$$

where E_H is the Hartree energy and $t_{au} = 24.19$ as is the atomic unit of time. This shows the atomic unit of intensity is 6.4364×10^{15} W/cm^2 in agreement with reference [38].

We recognize that in ultrafast physics the dynamics is governed by the laser field, not intensity. However, experimental papers still quote pulse intensity in SI units. Although it is possible to use Eq. (1.35) as a tool for conversion in linearly polarized light, it is incorrect to call it the atomic unit of intensity.

Chapter 2

Velocity Map Imaging Chamber

We used a velocity map imaging (VMI) spectrometer to make high precision measurements of the photo-electron and photo-ion momentum distributions from multi-photon ionization [83]. In this chapter we provide the details of the spectrometer and associated electronics, and describe an experimental calibration technique. Lastly we discuss a new approach to imaging the 3-D momentum distributions in a VMI spectrometer. The method works for both electron and ions and is applicable to distributions of arbitrary symmetry.

2.1 Spectrometer

Velocity map imaging is an experimental technique for measuring a projection of the 3-D momentum distribution onto a two dimensional detector. Invented in 1997, the simplicity of the technique has led to its widespread adoption in physics and chemistry labs around the world. A photograph of the chamber at JASLab is shown in Fig. 2.1. The apparatus consists of two differentially pumped vacuum chambers, separated by a gate valve. The source chamber shown on the right in the photo is pumped by a 1000 L/s turbo pump to a nominal base pressure of 5×10^{-8} torr. The detector chamber is shown on the left in the photo and contains the spectrometer and detector. It is pumped by a 500 L/s turbo pump to a base pressure of 1×10^{-9} torr. The detector is read out by a video camera located outside the high vacuum chamber shown at the top of the photo.

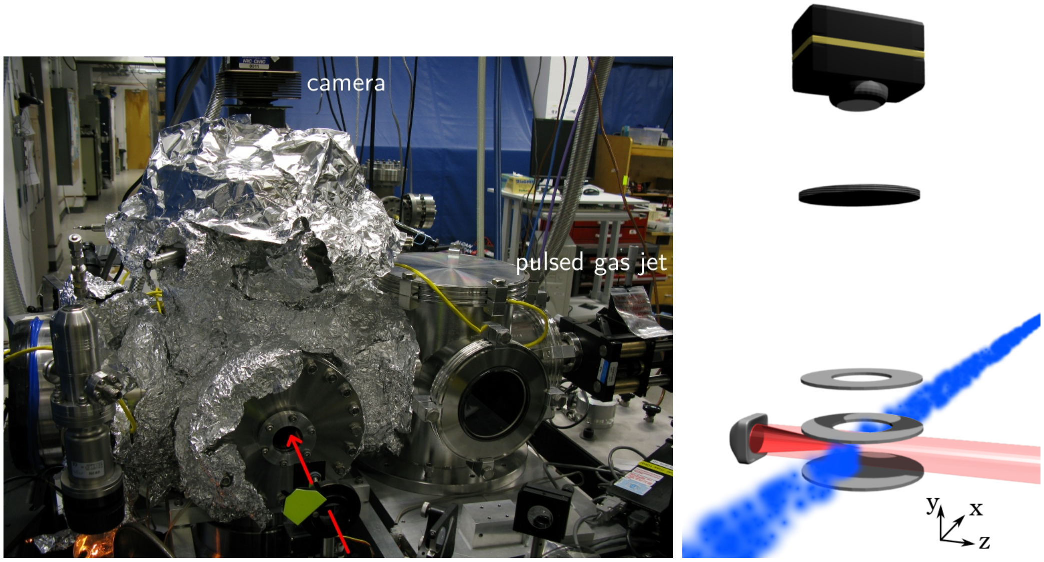

Figure 2.1: **Left** Photograph of the VMI apparatus showing the source chamber (right) and detector chamber (left). The detector is read out by a CCD camera (top) and stored on a desktop computer (not shown). **Right** Sketch of the VMI spectrometer. The laser pulse propagates along the z-axis; at the focus, it overlaps the molecular beam shown in blue, which propagates along x. The spectrometer electrodes shown in grey create an inhomogeneous electric field along the y axis that focuses charged particles onto the MCP detector.

The spectrometer itself consists of three stainless steel electrodes mounted in a cylindrical geometry inside the high vacuum chamber. A sketch of the spectrometer is shown in Fig. 2.1. An laser beam incident from outside the chamber is focused onto a collimated gas jet at the center of the spectrometer by a parabolic mirror ($f = 50$ mm, diameter $= 26.42$ mm). The laser focus is between the lower electrode, called repeller, and the middle electrode, called extractor. The potential on these two electrodes is adjustable from -15 kV to +15 kV using homemade power supplies. The top electrode is always grounded. By selecting the polarity of the electrodes, the spectrometer can be made to image either photo-electrons or photo-ions. These charged particles are focused onto a micro-channel plate detector (MCP). The detected signal is then read out by a CCD camera and stored on a desktop computer (not shown).

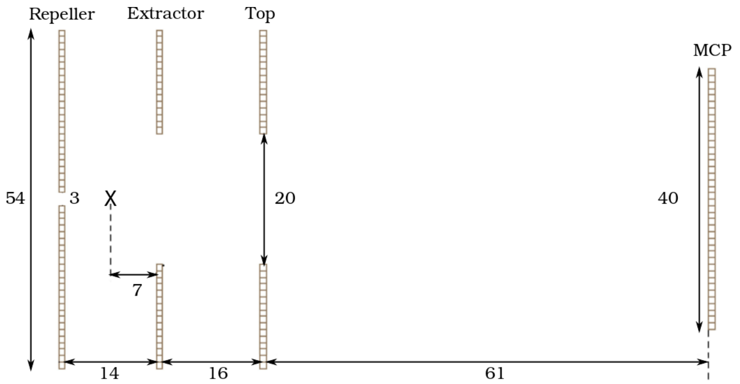

Figure 2.2: Cross section through the centre of the VMI spectrometer. The X marks the laser focus. All dimensions are in mm.

The spectrometer dimensions are given in Fig. 2.2. Note that the repeller and extractor electrodes are 1 mm thick and the top electrode is 3 mm thick. A small hole (diameter 3 mm) was drilled in the centre of the repeller electrode to allow ions to pass through when the spectrometer operates in electron imaging mode. This eliminates secondary electron emission which can occur when ions are created in the laser focus and accelerate into the repeller electrode.

Tuning the voltage on the repeller and extractor creates an electrostatic lens which focuses the charged particles onto the MCP detector. A simulation showing the equi-potential lines under velocity focusing conditions is shown in Fig. 2.3(a). In order to achieve velocity focusing, the correct ratio of the repeller to extractor voltage must be found. In general this depends on the dimensions of the spectrometer [83]. In our geometry, simulations and tests show that the velocity focusing condition is $V_E/V_R = 0.787$ where V_E and V_R are the extractor and repeller voltages.

The electrostatic lens is an inhomogeneous field that maps the particle's initial velocity at the laser focus into the detector plane. This is sketched in Fig. 2.3 where we show three velocity vectors having different magnitude but the same $v_{x'}$ component. The spectrometer field E_{spec} integrates over the $v_{y'}$ component and focuses the $v_{x'}$ component of each vector onto an identical location in the detector plane, sketched as the three horizontal lines. The projection of the velocity vector into the 2-D plane of the detector creates a "velocity map image".

The scale of the velocity spectrum or the magnification of the electrostatic

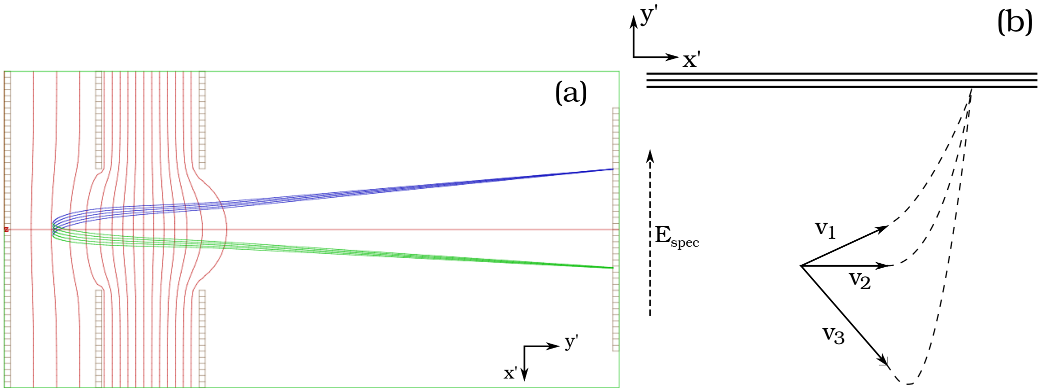

Figure 2.3: (a) Simulation showing the equipotential lines (red) when the spectrometer is operated at the velocity focusing setting $V_E/V_R = 0.787$. Photo-electrons having different kinetic energy are shown in blue and green. Electrons are mapped onto a unique position in the detector plane, proportional to their velocity. (b) Projection of three different velocity vectors having the same x' component into the plane of the detector.

lens depends on the magnitude of the repeller voltage. This also affects the time-of-flight (TOF). Using higher voltage lowers the time-of-flight, thereby allowing higher energy particles to be mapped onto the detector. In the inhomogeneous electric field, the TOF obeys the usual scaling law,

$$t = \kappa\sqrt{\frac{m}{qV_R}} \tag{2.1}$$

where κ is a fitting constant [83]. For electrons the TOF is nanoseconds and it is impossible to resolve them electronically. For heavier ions the TOF is ~ 1 μs and it is possible to separate different m/q using electronics (see section 2.2). A simulation showing the ion TOF vs. m/q at $V_R = 1$ kV is shown in Fig. 2.4. There is good agreement with Eq. (2.1) using $\kappa = 0.294$ μs (kV/amu)$^{1/2}$. Note that the measured TOF values can change day to day by ~ 80 ns depending on the position of the laser focus.

2.2 Data Acquisition

The VMI spectrometer uses a micro-channel plate detector in chevron configuration [84] (Burle Industries 3040PS). The front of the MCP is grounded –

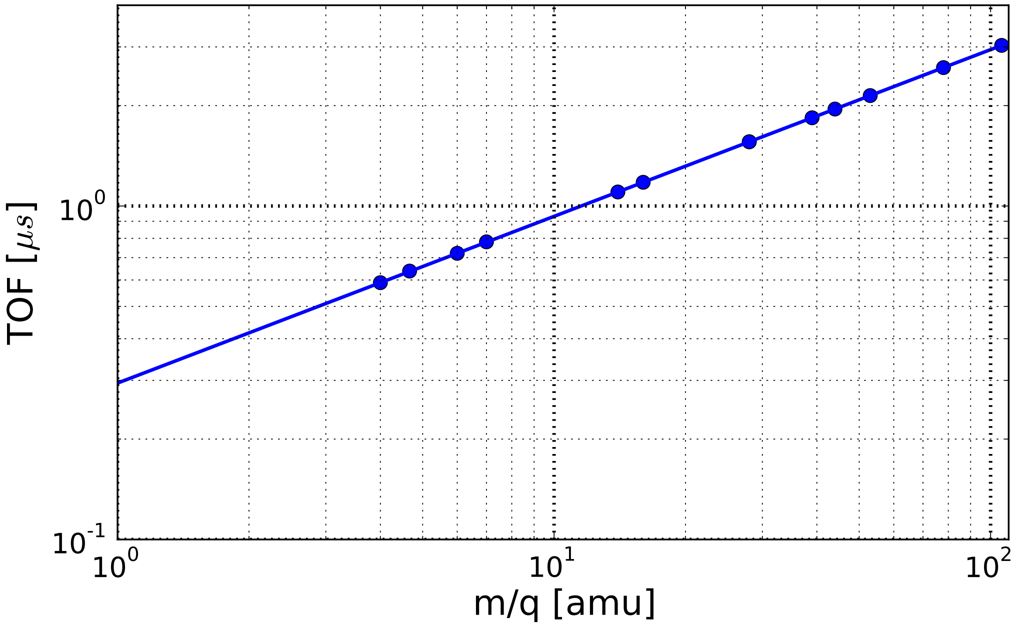

Figure 2.4: Ion TOF simulation at $V_R = 1$ kV. The blue line is from Eq. (2.1) with $\kappa = 0.294$ μs (kV/amu)$^{1/2}$.

allowing efficient detection in both electron and ion imaging modes. The voltage on the back of the MCP is controlled by a high voltage switch (Directed Energy GRX) and is pulsed between +1.5 and +2.2 kV. The high voltage pulse is 300 ns in duration and synchronized with a trigger pulse from our laser system. Owing to the non-linearity of MCP amplification [84], there is no detected signal outside this 300 ns window. The amplified electron burst from the MCP is accelerated onto a phosphor screen (nominally at +5.00 kV DC) where it emits light.

The light from the phosphor is focused by a lens with adjustable focal length (Computar 09D) onto a 12 bit CCD camera mounted outside the vacuum chamber (DVC 1312M). The signal from the camera is transferred to a desktop computer via a frame grabber card (Matrox Meteor II Digital). The camera-frame grabber assembly acquire continuously at 12 fps and are not synchronized with the laser pulses.

Pulsing of the MCP has two advantages. First, it eliminates dark counts that largely occur when the laser pulse is not present. Secondly, pulsing the MCP in ion imaging mode allows for a selection of a portion of the ion TOF

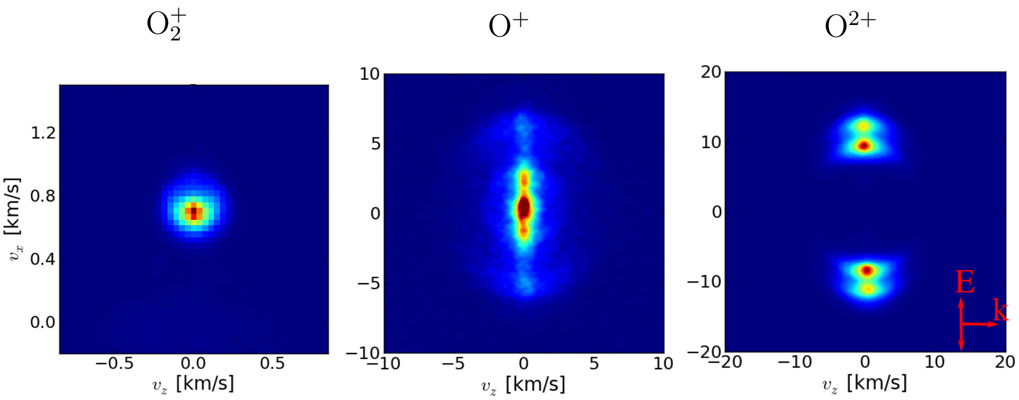

Figure 2.5: Pulsing the MCP allows us to scan through the TOF distribution and selectively image different fragments. Shown here are fragments produced in Coulomb explosion of O_2 with linearly polarized light.

spectrum. Explosion of a molecule will produce fragments with many m/q values. According to Fig. (2.4) the fragments will spread out in time-of-flight over 1 μs or more. By pulsing the detector for 300 ns it is possible to select different dissociation fragments or highly charged atomic fragments. This is a common approach to measuring molecular alignment (see chapter 4).

In Fig. 2.5 we present fragments from the Coulomb explosion of O_2. In these and all the fragment ion or photo-electron momentum spectra we present, the laser propagates left–right along the z axis and the polarization lies in the xy plane (unless otherwise noted). The propagation direction is indicated by the k arrow in Fig. 2.5 and the polarization axis is indicated by the E arrow.

Fig. 2.5 shows the molecular single ion O_2^+ which creates a narrow single spot on the detector. The spot is very tightly confined and is at the resolution limit of the detection system. As discussed in section 2.4, this is because the spread of the molecular velocity is very small in our gas jet. Also shown are O^+ and O^{2+} fragments. The bright spot at the centre of the O^+ distribution comes from O_2^{2+} which is stable and has the same m/q as O^+. O_2^{2+} produces a narrow ion spot very similar to the jet spot from O_2^+. In the O^{2+} distribution we see evidence of two dissociation channels, likely from $O_2^{3+} \rightarrow O^+ + O^{2+}$ and $O_2^{4+} \rightarrow 2O^{2+}$. The more highly charged dissociation channels yield larger fragment velocities because of Coulomb repulsion. Fig. 2.5 illustrates how we can select different fragments by scanning the timing of the high voltage pulse on our MCP detector.

MCP dead time. When a charged particle hits the MCP, an electron avalanche ensues. It takes some time afterward for the charge to be restored to a particular channel. A time constant for this process can be estimated as follows [84]. Suppose the MCP is like a parallel plate capacitor with a thickness $\sim$ 1 mm and dielectric constant $\epsilon = 8.3$. The capacitance of the MCP is then 95 pF. Each channel in the detector is 10μm in diameter and the open area is 55% of the total which means there are $\sim 8.8 \times 10^6$ channels on the detector. Thus the capacitance per channel is 10^{-17} F. The resistance of the MCP has been measured with a high voltage power supply and has the value 12.24 MΩ. The resistance per channel is then 1.1×10^{14} Ω. Multiplying these yields a time constant for each channel $\tau = RC \approx 1$ ms. In reality each channel acts more or less independently, so it is possible to measure more than one particle per laser pulse provided they do not hit the same channel.

2.3 Calibration

Electrons

The momentum scale of the spectrometer was calibrated using the photoelectron spectrum from above threshold ionization in linearly polarized light. We measured ATI spectra by focusing pulses at 400 and 800 nm onto a supersonic gas jet containing argon. The ATI spectra were recorded at seven different repeller voltages. At each repeller voltage, the extractor voltage was adjusted to maintain velocity focusing. Examples of measured spectra are shown in Fig. 1.8. Using the knowledge that the ATI peaks are spaced by the energy of one photon, we determine a momentum scale at each repeller voltage. The result is plotted in Fig. 2.6.

From Eq. (2.1) we note that the TOF scales with the square root of repeller voltage. Hence the displacement in the plane of the detector $x = v_x t$ obeys the same scaling. Indeed, Fig. 2.6 shows that the electron momentum scaling follows the expression $y = a\sqrt{V_R}$ where $a = (3.32 \pm 0.02) \times 10^{-3}$ a.u./(pixel kV$^{1/2}$). The blue and red curves in Fig. 2.6 are fits to the data at the two wavelengths. This expression provides an electron momentum calibration at all repeller voltage values.

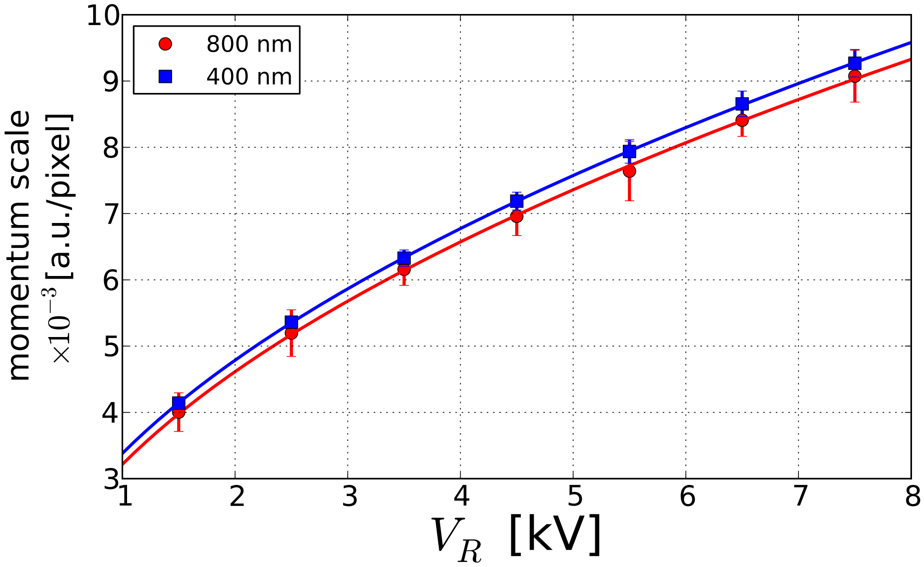

Figure 2.6: Momentum calibration as a function of repeller voltage measured from ATI of Ar at 400 and 800 nm. The momentum scale obeys the expression $y = a\sqrt{V_R}$ where $a = (3.32 \pm 0.02) \times 10^{-3}$ a.u./(pixel kV$^{1/2}$).

Ions

We can use the ion TOF calibration from Fig. 2.4 to estimate the ion momentum scale on the detector. We find that

$$\frac{v}{x} \propto \frac{1}{t} = \frac{1}{\kappa}\sqrt{\frac{qV_R}{m}} \times \text{dpix} = 0.168\ \frac{\text{km/s}}{\text{pixel}}\ \sqrt{\frac{qV_R}{m}} \tag{2.2}$$

where dpix is the size of one pixel in m. Note that the momentum scale changes depending on the m/q ratio of the particle being imaged. Using Eq. (2.2) we find that at $V_R = 1.00$ kV, the scale for protons is ~ 0.168 (km/s)/pixel, while for N_2^+ it is ~ 0.030 (km/s)/pixel, etc.

2.4 Gas Source

The source chamber contains a pulsed gas valve (Even-Lavie E.L.-5-2-2005-HRR, RT) which can operate up to 100 bar and up to 1 kHz. The valve is pulsed for 10 μs, synchronized with the laser trigger. The gas jet is collimated by a stainless steel skimmer (diameter = 1.02 mm) before entering the detector chamber. Once in the detector chamber the jet is further collimated by a piezoelectric slit (Piezosystem Jena PZS 1) of variable width.

The temperature of the gas jet was determined by fitting to rotational revivals in O_2. We used a linearly polarized pump pulse at 800 nm to create a rotational wavepacket in pure O_2 at 8.5 bar. A circularly polarized probe pulse explodes the molecules at a variable delay controlled by a stepper motor. We set the timing on the HV switch to select the O^{2+} fragments as shown in Fig. 2.5. Since the exploding molecules recoil along the molecular axis, by recording the two dimensional O^{2+} momentum distribution we can determine the molecular alignment distribution [85]. In chapter 4 we discuss molecular alignment in more detail.

An example of rotational revivals in O_2 is shown in Fig. 2.7. The revivals show characteristic strong 1/4 and 3/4 revivals at 2.92 and 8.78 ps. This is because only odd rotational states are populated in O_2, owing to nuclear spin selection rules [85]. In the intermediate regions between the fractional revivals there remains small sub-structures. The initial distribution of rotational states is very narrow when using a very cold gas source. Consequently the pump laser pulse excites a highly coherent rotational wavepacket. The rotational temperature obtained from fitting to the revivals is 5 K. This very low value for the rotational temperature produces the intermediate structures seen in the alignment scan in Fig. 2.7 in contrast to other experiments using a higher temperature continuous gas jet [85]. It is expected that translational and rotational degrees of freedom are in equilibrium for these gas sources [86]. It would also be possible to characterize the jet using the speed ratio [87]. Given the limited resolution shown in Fig. 2.5 it is difficult to make reliable measurements below 10 K.

In addition to the gas jet, the detector chamber is equipped with a variable leak valve (Varian). Some preliminary tests were done by leaking gas into the interaction chamber to around 10^{-7} torr. The cooling properties and higher density in the pulsed gas jet makes it a more attractive source for regular use.

2.5 Laser system

The laser system used in this work is a Ti:Sapphire chirped-pulse-amplification (CPA) system. It produces compressed pulses 45 ± 4 fs FWHM in intensity at 1 kHz and 2.25 ± 0.03 mJ. The majority of the uncertainty in both pulse

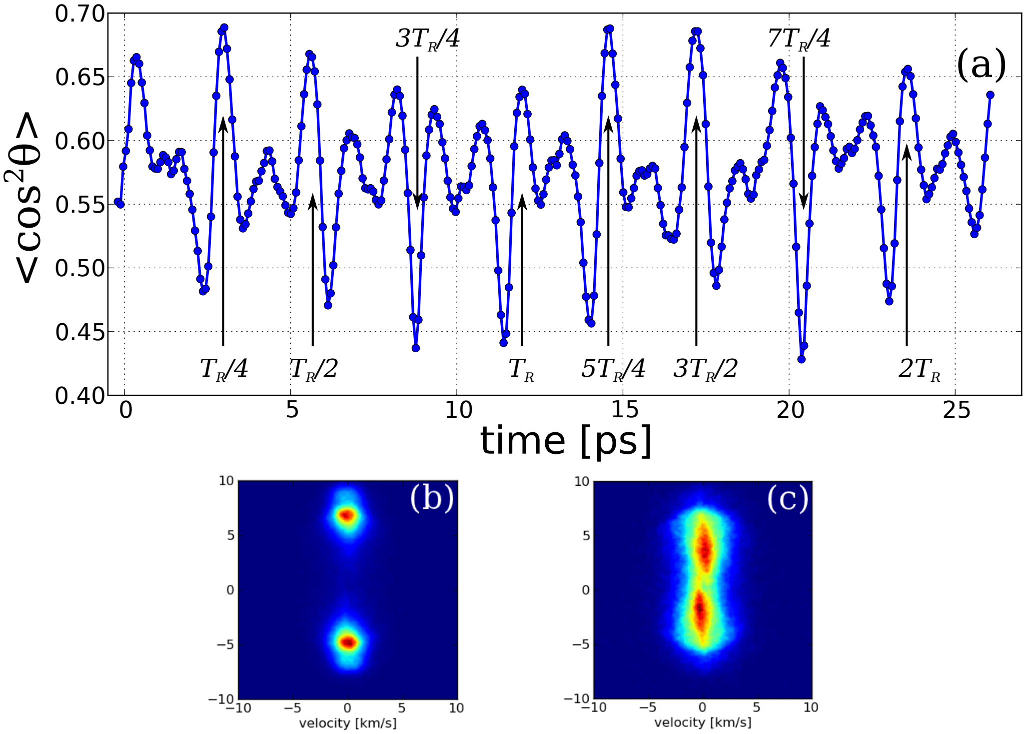

Figure 2.7: (a) Revivals in the alignment of O_2. The full revival occurs at 11.7 ps. (b) O^{2+} momentum distribution at 1/4 revival (2.92 ps). (c) O^{2+} momentum distribution at 3/4 revival (8.78 ps).

energy and duration is due to systematic changes in alignment. The nominal wavelength is 800 nm with a bandwidth of 23 nm FWHM.

For some experiments we used self-phase modulation in a hollow fibre (diameter=250 μm, length=1.0 m) filled with Ar gas to broaden the spectrum of the 45 fs pulse [88]. The bandwidth of the output pulse was 200 nm. The pulse was then compressed using a set of chirped mirrors (Femtolaser GSM014). The compressed pulse was measured to be 15 ± 1 fs FWHM using GRENOUILLE [89].

For some experiments we have used an optical parametric amplifier (Light Conversion TOPAS standard model) pumped by the 800 nm system to convert the photon wavelength to 1400 nm. The pulse at 1400 nm was estimated to be 70 fs.

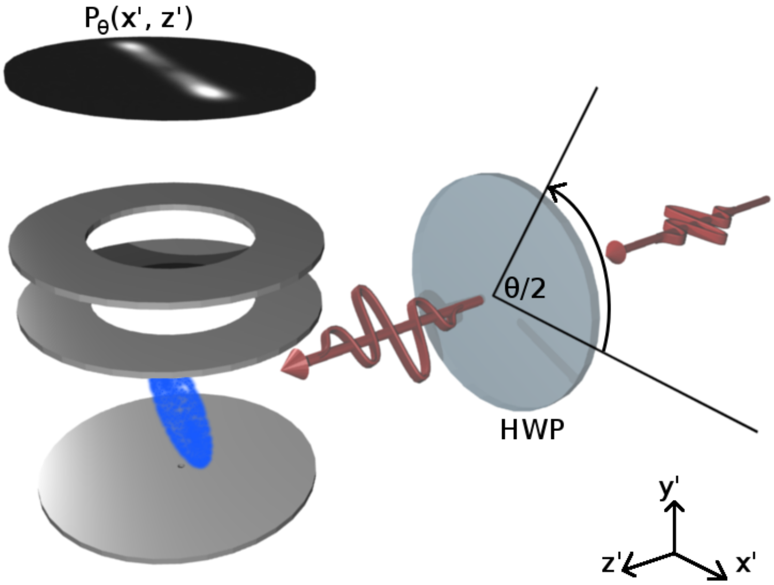

Figure 2.8: The momentum distribution of electrons or ions is mapped by the VMI spectrometer onto a 2-D detector in the lab frame of reference (x', y', z'). The momentum distribution can be rotated with respect to the detector by placing a half wave plate before the spectrometer.

2.6 Image Inversion

In a standard VMI setup the measured 2-D momentum spectrum is a projection of the 3-D distribution onto the detector. This is sketched in Fig. 2.8. There are several different strategies for recovering the three dimensional structure from a measurement of it's projection – a classic inverse problem. One approach called slice imaging uses electrostatic fields to isolate the central region of the ion cloud before pulsing an MCP detector [90]. Another technique uses a high speed shutter to record the particle TOF in addition to (x, y) position on the detector [91]. Following the spirit of delay-line anode detectors [92], these three pieces of information can be used to recover the complete 3-D distribution. Both experimental approaches work for heavy ions where the momentum distribution stretches out over microseconds, but cannot be used for smaller mass particles like electrons.

2.6.1 Abel Transform

By far the most common approach to imaging the 3-D distribution in VMI is to exploit the symmetry of the fragment distribution. In experiments using linearly polarized light, the fragment momentum distribution is cylindrically symmetric about the polarization axis. In circular polarization the k-axis is an axis of cylindrical symmetry. With this *a priori* knowledge, it is possible to mathematically extract the 3-D distribution from a single measurement of it's projection [93, 94, 95].

Let the momentum distribution have internal cylindrical symmetry about the x axis and be denoted $f(x, r)$. Let the lab frame of reference be denoted (x', y', z'). The laser propagates along the z' axis. Initially we consider ionization by linear polarized light where the polarization axis is x'. The VMI static field projects the distribution over the y' axis. The two frames are related by the transformation: $x' = x$, $y' = r\sin\theta$, $z' = r\cos\theta$. The image on the detector is therefore,

$$P(x', z') = \int_{-\infty}^{\infty} f(x, r)\mathrm{d}y' = 2\int_{|z'|}^{\infty} f(x', r)\frac{r\mathrm{d}r}{\sqrt{r^2 - z'^2}} \ . \tag{2.3}$$

This is the Abel transform of $f(x, r)$. The 3-D distribution is related by the inverse Abel transform [96]

$$f(x, r) = -\frac{1}{\pi}\int_{r}^{\infty} \frac{\mathrm{d}P(x, z')}{\mathrm{d}z'}\frac{\mathrm{d}z'}{\sqrt{z'^2 - r^2}} \ . \tag{2.4}$$

The goal of many algorithms is to extract the object distribution $f(x, r)$ from a single measured projection $P(x', z')$. In practice, noise in the measured projection and the singularity in Eq. (2.4) makes direct inversion impossible. The approach employed in Ref. [93, 94] is to find a set of basis functions that are analytical solutions to (2.3). Then the data can be fit to the basis set using a least-squares minimization. Ref. [95] uses an iterative process to determine the solution to (2.4). Both methods work well if and only if (1) the momentum distribution contains an axis of cylindrical symmetry, and (2) that axis lies in the plane of the detector.

What if the distribution does not contain cylindrical symmetry? This is the case with elliptical polarization, but other conditions can also break the symmetry. Ionization of aligned molecules [79, 97], or using orthogonally polarized two-colour fields [98, 99] will yield photo-fragment momentum distributions without cylindrical symmetry. In these situations a more general technique is required.

2.6.2 Tomographic Imaging in VMI

Computerized Tomographic (CT) imaging is a general technique for 3-D imaging of arbitrary objects. It was applied to medical x-ray imaging [100] and was recognized with the Nobel Prize in Medicine in 1979. The word tomography comes from the Greek *tomos* meaning slice. Medical CT was heralded as an improvement on conventional x-ray imaging because it yielded a series of slices through an object, rather than just a single 2-D image. As a form of non-invasive, non-destructive imaging this was a major breakthrough.

The conceptual development of CT imaging begins with the work of Radon in 1917 [101]. He considered the problem of the reconstruction of an object function from a series of line integrals. In our notation we have called the object $f(x, r)$; we now consider the case of an arbitrary distribution $f(x, y, z)$. The object is rotated by an angle θ with respect to the detector. Mathematically, the two frames of reference are related via

$$\begin{pmatrix} x' \\ y' \\ z' \end{pmatrix} = \begin{pmatrix} \cos\theta & -\sin\theta & 0 \\ \sin\theta & \cos\theta & 0 \\ 0 & 0 & 1 \end{pmatrix} \begin{pmatrix} x \\ y \\ z \end{pmatrix} \tag{2.5}$$

where (x', y', z') are the lab frame of reference and the laser propagates along the z' as before. The rotated distribution is then projected onto the detector. Mathematically this is given by the Radon transform,

$$P_\theta\left(x', z'\right) = P_\theta\left(x', z\right) = \int f\left(x, y, z\right)\, \mathrm{d}y'. \tag{2.6}$$

We note that the Radon transform is a generalization of the Abel transform (2.3) to objects without cylindrical symmetry. This comes at the cost of the introduction of the new variable θ. CT reconstruction is a more powerful technique than Abel inversion, but at the expense of an expanded set of coordinates. Therefore, more data is needed in CT imaging.

Physically, the Radon transform is carried out in a VMI experiment by the spectrometer's DC electric field [74, 102]. As discussed in Fig. 2.3, the projection of the momentum vector into the plane of the detector is the experimental realization of the Radon transform. By collecting projections from many different directions the tomographic algorithm is able to reconstruct the complete momentum distribution. Unlike medical tomography, wherein a detector typically covers a portion of the volume of interest, the projections in VMI experiments span the complete momentum space of the photo-electrons. Thus, by rotating the distribution there is enough information to recover the full 3-D distribution for any polarization state.

The setup for VMI tomography is depicted in Fig. 2.8. The laser propagates along the z' axis with polarization in the $x'y'$ plane. A quarter wave plate placed in the beam will create elliptically polarized light. This does not contain an axis of symmetry. A half wave plate can then be used to rotate the axes of the polarization ellipse. The ability to rotate the polarization and thereby the velocity distribution in the chamber is a necessary step in tomographic reconstruction.

The inversion of the 2-D projections follows the parallel ray filtered backprojection algorithm [100]. This method can yield exact reconstructions in contrast to techniques without a filter step. In any computer implementation of the algorithm, the projections are always sampled at some momentum interval dp and some angular interval $\Delta\theta$. This means that the data in the Fourier domain are over-sampled at low spatial frequencies, and undersampled at high spatial frequency. The use of a filter with the correct form can compensate sampling artifacts [103].

The first step in the tomographic algorithm is to filter each measured projection $P_\theta\left(x',z\right)$. This is implemented as the convolution of $P_\theta\left(x'\right)$ with a filter function. We have used the discrete "Shepp – Logan" filter [103]:

$$h\left(x'\right) = h\left(n\tau\right) = -\frac{2}{\pi^2}\left(\frac{1}{4n^2-1}\right) \tag{2.7}$$

where $x' = n\tau$ with τ as the sampling interval and n is an integer. The filtered projection is

$$Q_\theta\left(x',z\right) = h(x') * P_\theta(x',z) \tag{2.8}$$

As explained in section 2.1, the data were originally acquired by integration along the spectrometer's electric field (y' axis). At this stage in the reconstruction, each filtered projection $Q_\theta\left(x',z\right)$ must be backprojected along the y' axis. Summing over all the projection angles yields the reconstructed distribution. Mathematically, the reconstructed distribution $F\left(x,y,z\right)$ is given by

$$\begin{aligned} F\left(x,y,z\right) &= \int_0^\pi Q_\theta\left(x',z\right)\ \mathrm{d}\theta && (2.9)\\ &= \frac{\pi}{K}\sum_{i=1}^{K} Q_{\theta_i}\left(x\cos\theta_i - y\sin\theta_i, z\right) && (2.10)\end{aligned}$$

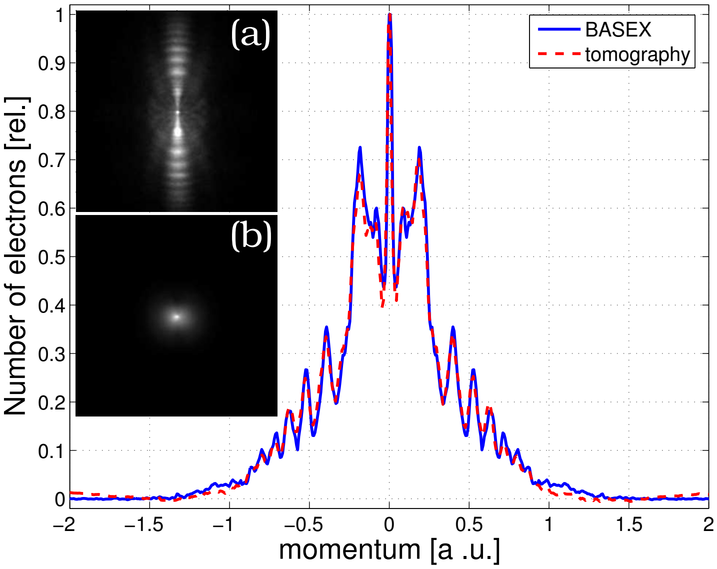

Figure 2.9: Profile along the polarization axis of the 3-D momentum distribution. Blue (solid) line: distribution inverted using the inverse Abel (BASEX) method [93]. Red (dashed) line: distribution inverted using the tomographic method. Inset: examples of projections used in the tomographic reconstruction (a) $\theta = 0°$, (b) $\theta = 90°$.

where the projections are sampled at K different angles and $0 \le \theta_i \le \pi$. Implementing the discrete backprojection (2.10) requires one-dimensional interpolation to find the projection value $Q_{\theta_i}(x')$ at each point (x, y) in the reconstructed image.

Eq. (2.10) is the reconstructed momentum distribution in three dimensions. Thus, by rotating the laser polarization the tomographic method allows us to reconstruct the complete momentum distribution.

We first compare the tomographic method with the inverse Abel method for linearly polarized light. For an Abel inversion the polarization axis must be parallel to the detector face. A single two-dimensional projection was recorded at a laser intensity of 2×10^{14} W/cm^2 and then inverted using the BASEX method [93]. A profile along the polarization axis in the inverted distribution is shown as the solid line in Fig. 2.9. The profile has been normalized to its maximum value. The distribution shows multiple ATI peaks.

Next, the tomographic method was tested under the same conditions.

The laser parameters were held constant and the polarization direction was rotated using a broadband half-waveplate (Bernhard Halle GmbH). Examples of two projections taken at 0 and 90 degrees are shown in Fig. 2.9a and 2.9b. In Fig. 2.9a the polarization is parallel to the detector face, and in Fig. 2.9b it is perpendicular. The two dimensional projections $P_\theta\left(x', z'\right)$ were recorded as the polarization rotated from $0-90$ degrees in steps of 2 degrees. These projections were then duplicated to yield the π projection angles required by the parallel ray backprojection algorithm.

The tomographic method was used to reconstruct the momentum distribution in 15 different slices through the 3-D momentum distribution. A spacing of 0.071 atomic units was used between each adjacent slice along the laser propagation (z') axis. The result is the 3-D electron momentum distribution. A profile along the polarization axis and in the plane of polarization $(z'=0)$ is shown as the dashed line in Fig. 2.9. Again, the profile has been normalized to its maximum value. The profile generated by the tomographic method is reconstructed using a series of 1-D projections measured at different angles. This is in contrast to the inverse Abel method which uses a 2-D projection to infer the structure of the momentum distribution. There is good agreement between the tomographic method and the result from the BASEX method. This shows the tomographic method reproduces the result of the inverse Abel transform for linearly polarized light.

The power of the tomographic method lies in its application to distributions that need not contain any symmetry. A quarter wave plate was rotated by 43° to create elliptically polarized light at an intensity of 3×10^{14} W/cm^2. Using the half wave plate in Fig. 2.8 the polarization ellipse was rotated from $0-178$ degrees in steps of 2 degrees. At each angle a projection of the electron velocity distribution containing roughly 6×10^5 electrons was acquired for 3×10^4 laser pulses. The tomographic method was used as before to reconstruct the 3-D velocity distribution. The distribution in the plane of polarization is shown in Fig. 2.10.

Ellipticity appears in two ways in the reconstructed image. The most obvious evidence is in the nonuniform momentum distribution. This is shown more clearly in Fig. 2.10 where a profile along the major axis is shown as the red line; the minor axis is shown as the black line. In Fig. 2.10 it is clear that there are more electrons along the minor axis of the ellipse. This occurs because the ionization rate is a function of the laser's instantaneous electric field while the drift velocity (1.11) is a function of the vector potential at the phase of ionization. Since the two are $\pi/2$ out of phase, the larger ionization

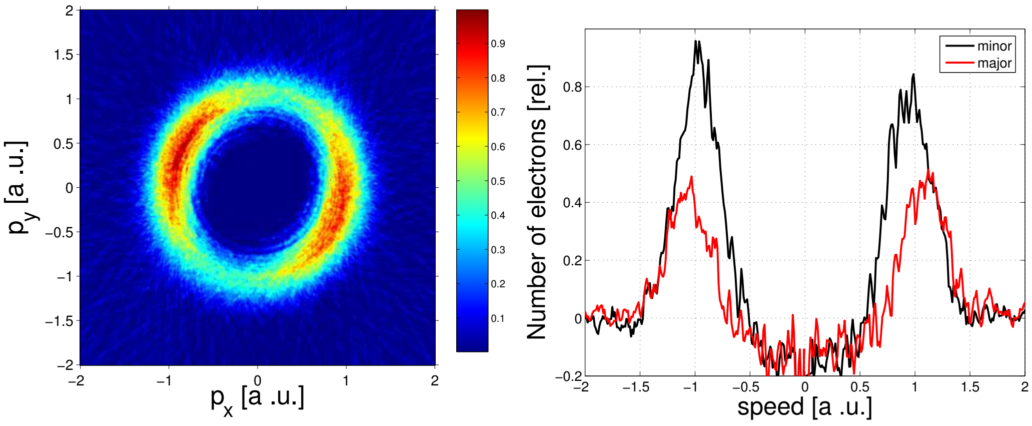

Figure 2.10: Tomographic imaging of the electron velocity spectrum in elliptically polarized light. **Left**: Reconstructed distribution in the plane of polarization. The colour code represents the relative number of electrons. **Right**: The number of electrons as a function of their speed measured along the minor (black) and major (red) axes.

rate appears along the minor axis of the velocity distribution, as shown in Fig. 2.10. Using the size of each of the axes, the laser ellipticity is found to be 0.89.

The reconstructed distribution also gives evidence into the role of the Coulomb potential in the elliptically polarized field [76, 97]. The experiment was done in close to circularly polarized light, and the major axis of the polarization ellipse is at 43° with respect to the v_x axis. However the major axis of the photo-electron distribution is at 26°. The Coulomb potential is responsible for this angular offset. As the photo-electron is curling away from the parent ion, there is a small attraction pulling it back. Within a few optical cycles the electron moves far enough away that the attraction to the nucleus is much smaller than the laser field and can be ignored.

The tomographic method can be applied to visualize the 3-D velocity distribution for any polarization state. Fig. 2.11 shows a three-dimensional representation of the reconstructed velocity distribution in both linearly and elliptically polarized light. A surface of constant probability is shown in navy blue. On the interior of the distributions the colour coding reflects the probability to measure an electron at each point in the 3-D distribution. In

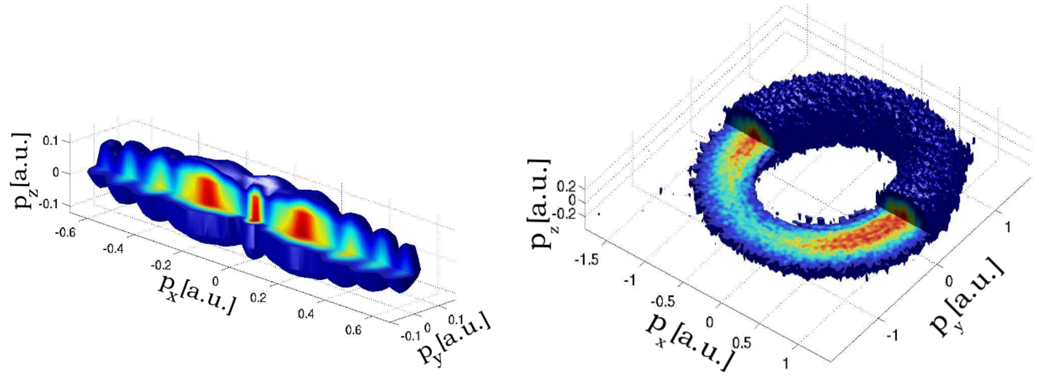

Figure 2.11: 3-D reconstructions using the tomographic method in linearly polarized light (left) and elliptically polarized light (right). The colour code is the same as Fig. 2.10. Values less than 0.1 are transparent.

Fig. 2.11 the data was averaged over neighbouring volume elements.

Chapter 3

Atoms in Strong Laser Fields

Rare gas atoms are a system where tunnelling is extensively tested. We focus on ionization of rare gas atoms by femtosecond laser pulses to study the photo-electron momentum distribution from tunnelling and explore the limitations of tunnelling models. A rigorous test of the tunneling approximation must disentangle the influence of re-collisions [18] – both low impact parameter re-collisions and the multiple large impact parameter collisions that comprise Coulomb focusing [104]. Coulomb focusing modifies the lateral momentum distribution in linearly polarized light [29, 30] and it is essential to include it in a quantitative description of non-sequential double ionization [105]. We use circularly polarized light to overcome these challenges. As we discussed in section 1.2 and illustrate in Fig. 3.1a, an electron that ionizes in circularly polarized light does not re-encounter its parent ion.

In the process of testing laser tunnelling, we demonstrate an improved technique for measuring the intensity of the femtosecond pulse via the photo-electron momentum. We then apply this to study intensity dependent features in the photo-electron momentum spectra.

We next examine the role of conserved quantities in multi-photon ionization. Eq. (1.33) defines how energy conservation is satisfied in above threshold ionization. We address the question of momentum conservation – both the photon linear momentum where we present experimental results supported by a classical model based on the Lorentz force, and angular momentum conservation which we consider in the context of the model developed in section 1.2.

3.1 Photo-electron angular distributions from tunnelling

We performed a series of measurements on the intensity and wavelength dependence of photo-electron momentum spectra from single ionization of Ar and Ne using circularly polarized laser pulses. We find that the photo-electron momentum perpendicular to the laser field follows a Gaussian distribution whose width scales with intensity as predicted by (1.29). The absolute width is in substantial, albeit not total, agreement with (1.29). Our measured lateral expansion of the electron wave packet is $\approx 15\%$ larger than predicted. To test if this deviation arises from non-adiabatic corrections we have also repeated the experiment at different frequencies. In adiabatic tunnelling the laser field is treated as if it were a static field, time serving only as a parameter. It is rigorously valid for long wavelengths ($\gamma \ll 1$). Non-adiabatic tunnelling refers to deviations that arise at higher frequencies – when the field variation becomes too fast. We do not observe the wavelength scaling predicted by non-adiabatic tunneling [58, 71]. In fact, for the same laser intensity we measure the same width for electrons that tunnel at 800 nm and 1400 nm.

After tunnelling in a circularly polarized field, the photo-electron experiences nothing but the laser field until it reaches the detector. Since, in the dipole approximation, the laser field only acts in the plane of polarization, the electron momentum distribution cannot change in the direction perpendicular to the plane of polarization. By measuring the perpendicular distribution we observe the nascent quantum mechanical uncertainty in momentum imposed by the tunnel. Circularly polarized light has two other major advantages. First, the large angular momentum absorption suppresses resonantly enhanced multi-photon processes. Second, the field strength at which the electron tunnels can be measured via the momentum it gains in the plane of polarization (Fig. 3.1b side profile) [106]. In section 3.2 we will show that the accuracy in field measurement is enhanced by including the initial momentum distribution of the tunneled electron.

We use the VMI chamber described in chapter 2 to record a 2-dimensional projection of the 3-dimensional photo-electron momentum distribution. For our measurements we used 15 fs 800 nm pulses from a Ti:sapphire laser system [88]; and 70 fs 1400 nm pulses from an optical parametric amplifier as explained in section 2.5. The beams were focused with an on-axis parabolic

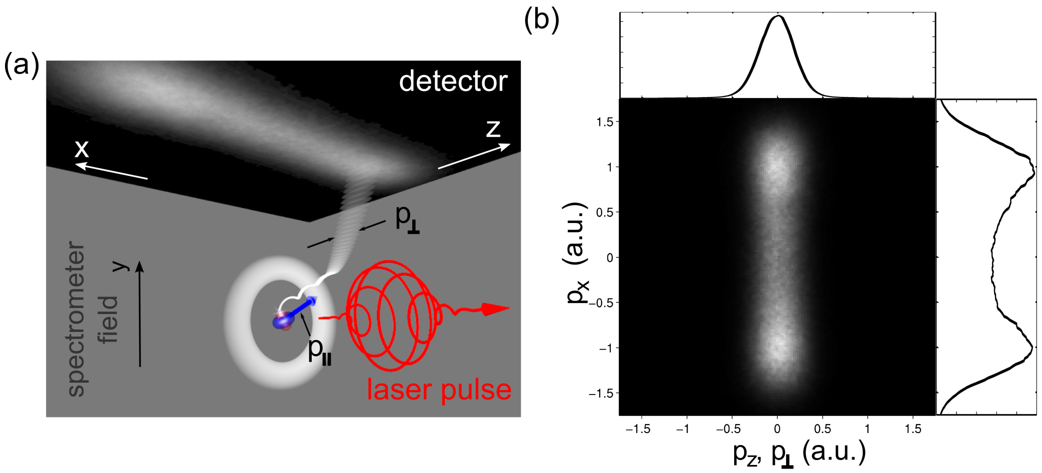

Figure 3.1: a) Schematic trajectory of the tunneled electron in circularly polarized light. The drift momentum of the electrons in the plane of laser polarization, summed over possible angles of the ionization field, yields a toroidal distribution of momentum where the centre of the ring is E/ω_L (see Fig. 2.11). The thickness of this distribution perpendicular to the laser polarization is the width of the momentum distribution at ionization. b) Measured photo-electron momentum spectrum from Ar at 3.1×10^{14} W/cm^2, 800 nm. The laser propagates along the z axis. The integrated profile along the direction of propagation (top) is in good agreement with a Gaussian distribution. The integrated profile in the plane of polarization (side) is used to determine the intensity.

mirror with $f = 5$ cm (F-number 12.5 for 800 nm and F-number 20 for 1400 nm). To ensure that the divergence of the focused beam did not influence our results, we performed experiments with different diameter beams.

Here, we will present results covering a range of Keldysh parameters from γ=0.58 to γ=1.53. We compared the measured lateral photo-electron distribution to the prediction of (1.32). The measurable momentum distribution is predicted to have the form $\exp(-{p_\perp}^2/\sigma^2)$, where $\sigma^2 = E/\sqrt{2I_p}$. We use the fact that the momentum distribution along the k-direction is unaffected by the laser field and we measure it directly. In the plane of polarization, however, the free electron is driven along a classical trajectory by the strong laser field [18]. For long times after the laser pulse has disappeared, the distribution in this direction is centred at $p_\parallel = E/\omega_L$.

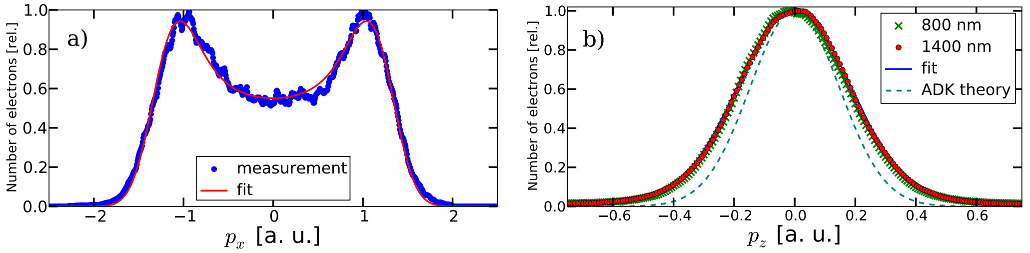

Figure 3.2: a) Measured and calculated distributions at 3.2×10^{14} W/cm^2, integrated along the propagation axis. As discussed in section 3.2, the quality of the fit to data is significantly improved by including the momentum distribution of tunneled electrons in our algorithm. b) The electron wavepacket at 800 and 1400 nm is shown along the p_z axis. The laser intensity was 1.8×10^{14} W/cm^2 for both wavelengths. Also shown is a Gaussian fit to the measurement and the prediction of the ADK theory (Eq. (1.32)) at this intensity. The small offset of the centre from zero is due to photon linear momentum [14] (section 3.3).

A typical image of the momentum distribution of electrons is presented in Fig. 3.1b. The laser beam propagation is along z, and x is in the plane of polarization. Integrating the image along the polarization axis (top profile) leads to a Gaussian profile which is used to test Eq. (1.32). The integrated signal along the propagation axis (side profile) is used to extract the laser field value at the moment of ionization $E(t_i)$.

The connection between the momentum distribution of the ions and the laser electric field at the moment-of-birth has been used before to estimate the laser field [106, 107]. To improve the fit to the measured electron momentum spectrum (Fig. 3.2a) it is necessary to include the initial quantum distribution of the electron in the plane of polarization. We provide more details on the method to determine the laser field at ionization in section 3.2.

The data in Fig. 3.2a was taken at approximately the saturation intensity for argon. For the geometry of a focused Gaussian beam, the interaction region can be divided into infinitesimal shells of constant intensity [106]. Since the pulse is short the atoms are essentially stationary during interaction with the laser and the electrons remain in the focus. As the laser pulse develops in time, the number of electrons from a particular geometrical shell varies with time. Saturation effects for single ionization are included in this model; higher order ionization is negligible for the intensities used in this experiment. The only fit parameters in the model are the laser intensity and total electron yield. Our model provides the differential electron yield distribution in the focus, $\mathrm{d}N/\mathrm{d}E$ where N is the relative number of electrons and E is the laser field. For simplicity in plotting the data we attributed a value of $E_{avg} = \int_0^{E_0} E\frac{dN}{dE}\mathrm{d}E$ to each distribution where E_0 is the peak electric field. To a large extent $E_{avg} \approx E_0$ for a pulse below the saturation intensity. For a pulse with peak intensity above the saturation limit $E_{avg} \approx E_{sat}$ (that is, the field where approximately 40% of the particles are ionized [108]).

Our experiment is in the regime $\gamma \approx 1$ so it is not clear that the electron can adiabatically follow the oscillating laser field. This is one assumption at the core of tunneling theory. Incorporating corrections for non-adiabatic effects introduces a wavelength dependence to the tunneling rate [58] and electron momentum spectrum [71].

For direct comparison with Eq. (1.32) we have included the bound momentum distribution in the non-adiabatic theory. The bound electron distribution $|\Phi_{n,l,m}|^2$ is used to multiply the non-adiabatic tunnelling filter [71],

$$W(p_\perp) \propto \exp\left(-\frac{I_p}{\omega} f\left(\gamma, p_\perp\right)\right) . \tag{3.1}$$

The function $f\left(\gamma, p_\perp\right)$ is given in [71] and we have set $p_\parallel = 0$ for tunnelling in circularly polarized light. In the non-adiabatic theory the momentum distribution scales with the laser wavelength as shown in the dashed curves of Fig. 3.3.

The measurement of the wavepacket width as a function of laser field in argon for both 800 and 1400 nm is presented in Fig. 3.3a. The data is plotted against predictions of Eq. (1.32) and the nonadiabatic theory. There is a substantial agreement between our data and the predictions of tunneling models. However, a deviation of about 15 percent remains. Our result shows that the width of the distribution perpendicular to the tunnel is only a function of the laser field and not the laser wavelength. The error bars include uncertainties in detector response, alignment and momentum calibration of the spectrometer, laser ellipticity, and numerical accuracy of the fit.

A similar result is obtained for neon in Fig. 3.3b. The width of the distribution expands with increase in laser field, however both existing theories predict different values for the absolute width of the measurement.

When we began this experiment we expected a major change in σ as ionization left the tunneling regime [109, 110, 111]. To test this hypothesis we used the second harmonic of the 800 nm pulse to ionize argon. The

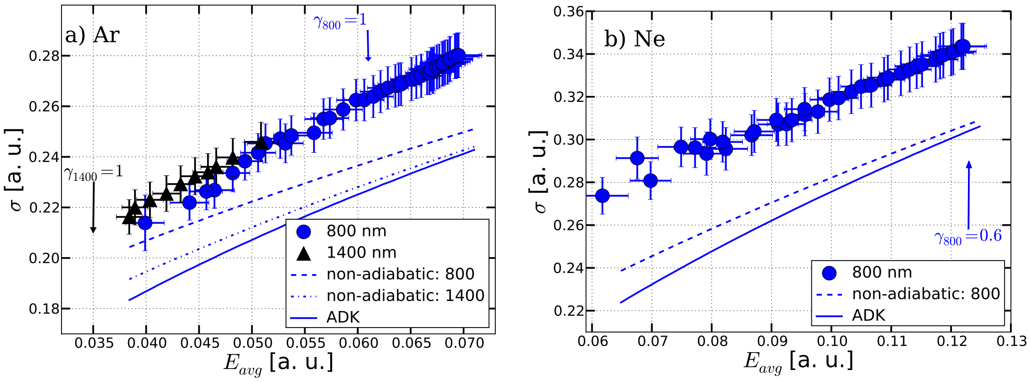

Figure 3.3: a) Width σ of the momentum distribution as a function of average laser field in the focus for argon at 800 and 1400 nm. The data is compared with predictions of non-adiabatic and ADK theories. b) Width of the momentum distribution as a function of the field for neon.

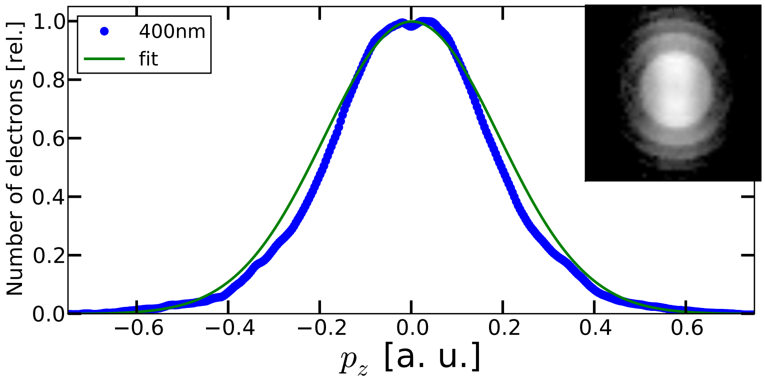

Figure 3.4: Integrated lateral distribution from ionization of Ar at 400 nm using circularly polarized light at approximately 2×10^{14} W/cm^2. Inset shows the measured 2-D electron distribution (log color scale).

400 nm, 50 fs pulse was also circularly polarized ($\gamma \sim 2.5$). While 400 nm ionization of argon is outside the region where tunneling is expected to be a valid approximation, we still measure a profile with a width that is similar to the values in the infrared. An example of a measured distribution for argon at 400 nm is shown in Fig. 3.4 where the inset is the measured 2-D spectrum and the figure is integrated over p_x. At this wavelength it was not possible to use the same intensity measurement method as in the infrared. We scanned the intensity over an estimated range 5×10^{13} W/cm^2 to 5×10^{14} W/cm^2. While the total electron yield increased substantially with intensity, we found no systematic intensity dependence of the lateral profile. Additionally, the width of the lateral distribution lies in the same range as the measurements in the infrared. The peak intensity used for the measurement in Fig. 3.4 is estimated as $(2 \pm 1) \times 10^{14}$ W/cm^2. The large uncertainty in the intensity arises from the combined uncertainty in the pulse duration and focal spot size.

The expansion of the lateral distribution with increasing field strength is a distinct feature of tunnelling. It corresponds to the barrier length decreasing. This is the opposite of what one expects from perturbative ionization. In the perturbative limit the photo-electron angular distribution is a superposition of spherical harmonics $Y_{l,m}(\theta, \phi)$ where the angular momentum l depends on the number of photons absorbed. One intuitively expects l to scale with the laser field, producing a norrower angular distribution at higher fields. This is in opposition to tunnelling theory and our experimental results in the infrared. However, recent simulations have shown a narrowing of the lateral wavepacket at 400 nm [72], suggesting a tunnelling picture is inappropriate at that wavelength.

3.1.1 Lateral wavepacket dependence on m

One issue which we considered in some detail is the contribution of multiple electron orbitals to the lateral wavepacket as measured in section 3.1. As we have shown in 1.3.1, for rare gas atoms the ionization rate from orbitals unaligned to the polarization axis (sketched in blue in Fig. 3.5) is only around 2-3% of the total under normal conditions. Typically the small contribution from $|m| = 1$ can be neglected, however, its significance depends on the precision of the experiment, and the observable quantity. We examine the role of the $|m| = 1$ orbitals via their contribution to the photo-electron lateral momentum distribution. This can provide a different perspective on orbital

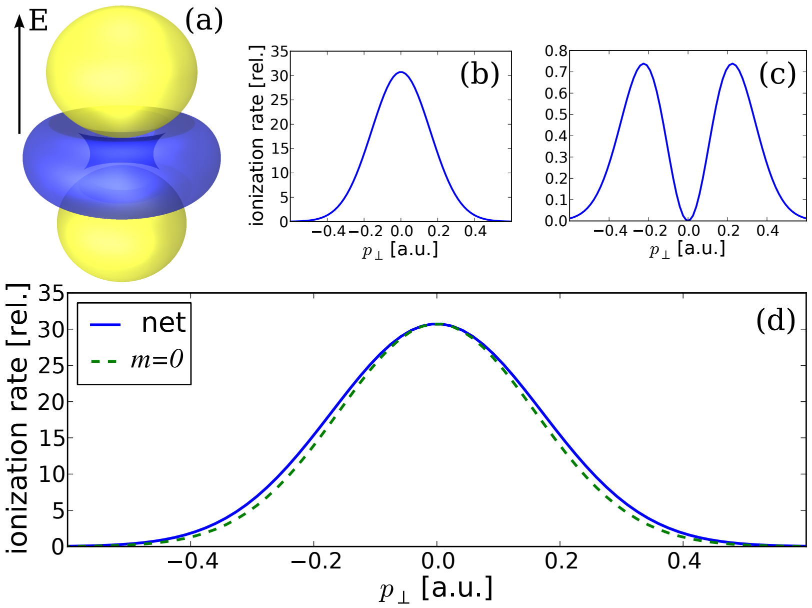

Figure 3.5: (a) Strong field ionization of rare gas atoms removes an electron mainly from the $m = 0$ orbital (shown in yellow) with a small contribution from the $|m| = 1$ orbital (shown in blue). (b) The calculated lateral photo-electron distribution for tunnel ionization from $m = 0$ using (1.32). (c) The calculated lateral photo-electron distribution for tunnel ionization from $|m| = 1$. (d) The net lateral distribution includes contributions from all 6 degenerate electrons in the valence shell and is wider than the single orbital prediction.

alignment in strong field ionization, in addition to previous studies using x-ray [112] or EUV absorption [113].

We have seen in section 3.1 how the DC and non-adiabatic tunnelling theory differ with respect to the lateral momentum distribution from the $m = 0$ orbital. In addition to different lateral distributions, the two theories differ in the ionization rate dependence on the bound orbital $\Phi_{n,l,m}(\boldsymbol{p})$. To model the momentum wavefunctions of rare gas atoms we use hydrogen-like wavefunctions with an effective nuclear charge [114, 115]. We used $Z_{ef} = 6.76$ for Ar and $Z_{ef} = 5.76$ for Ne [116]. It should be noted that Z in the expression for tunnel ionization rate (1.25) is the charge of the residual ion and is not the same as Z_{ef} [35]. By using single electron wavefunctions to model the

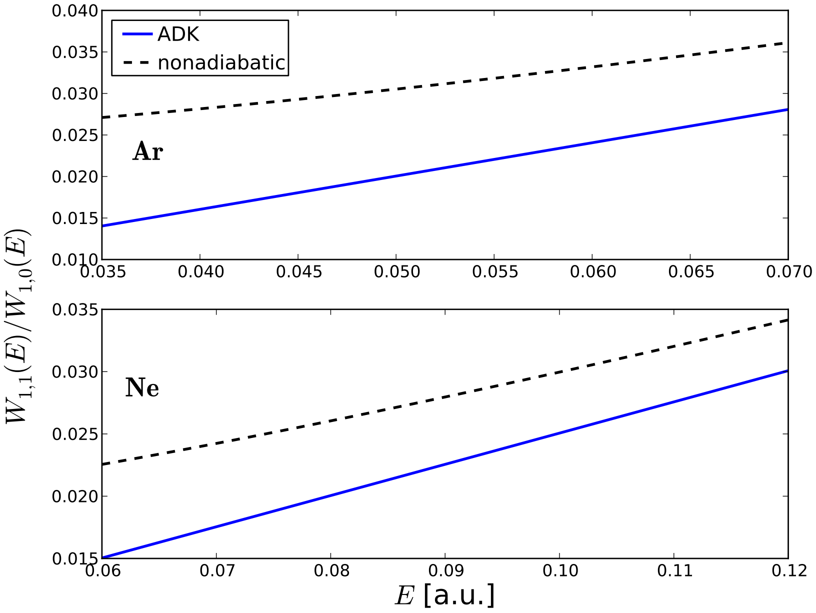

Figure 3.6: Relative ionization rate $W_{l,m}(E)$ from $|m| = 1$ vs. $m = 0$ orbitals in Ar (upper) and Ne (lower) as a function of laser field. The non-adiabatic curves are calculated at $\lambda = 800$ nm.

ionization of multi-electron atoms we are therefore not including electron-electron interaction. Furthermore, the hydrogenic orbitals are solutions to the non-relativistic Schrödinger equation and therefore do not include spin-orbit interaction or higher order corrections.

The expression for the ionization rate in the non-adiabatic theory is given in Ref. [58, 59] (see also [35]) where the pre-exponential factor is a function of both m and ω. The relative ionization rate for $|m| = 1$ vs. $m = 0$ at the experimental intensities is shown in Fig. 3.6 in neon and argon. The rate is only 2-4 %, but in all cases non-adiabatic effects at $\lambda = 800$ nm provide a clear enhancement of the $|m| = 1$ signal.

To model the lateral distribution from all three degenerate orbitals in the valence shell of argon and neon, we take the product of the tunnelling filter function Eqs. (1.29), (3.1) with the bound state. Assuming the instantaneous laser polarization is along the x axis, the lateral distribution is given by

$$P_m(p_\perp) = \int_{-\infty}^{\infty} |A_m|^2 \left|\left\langle p_\perp \left| \Phi'_{n,l,m} \right.\right\rangle\right|^2 \, \mathrm{d}p_x \tag{3.2}$$

where the normalization constant is

$$|A_m|^2 = \frac{W_{l,m}(E)}{\int \mathrm{d}^3\boldsymbol{p}\ \left|\left\langle p_\perp \middle| \Phi'_{n,l,m} \right\rangle\right|^2} \ .$$

In Fig. 3.5b we plot $P_0(p_\perp)$ for Ar at 2.5×10^{14} W/cm^2. The lateral distribution from $m = 0$ is a smooth Gaussian emerging at the rate $2W_{1,0}(E)$ where the factor of 2 represents the doubly occupied $m = 0$ orbital. The four electrons in $|m| = 1$ ionize with the rate $4W_{1,1}(E)$. Since the bound state orbital for $|m| = 1$ has a node along the polarization axis (consider the blue torus in Fig. 3.5a), these orbitals contribute to the distribution only at larger lateral momenta. This is sketched in Fig. 3.5c where we have plotted $P_1(p_\perp)$. The net lateral distribution is then the incoherent sum of these two contributions. The net distribution is shown in Fig. 3.5d along with the distribution from the single orbital ($m = 0$) calculation.

The multi-orbital wavepacket is still approximately described by a Gaussian, however its standard deviation is larger than the single orbital prediction. For comparison with the measured spectra the lateral distribution must be integrated over a second momentum axis. Hence the net momentum distribution along the propagation (z) axis of a circularly polarized pulse is

$$M\left(p_z\right) = \int_{-\infty}^{\infty} \left[P_0\left(p_\perp\right) + g_m P_1\left(p_\perp\right)\right]\ \mathrm{d}p_y \tag{3.3}$$

where g_m is a degeneracy factor, representing the weighting of the $|m| = 1$ orbital. For the noble gases with the exception of helium $g_m = 2$.

In Fig. 3.7 we compare the result of the multi-orbital calculation with the single orbital calculation and the experimental data at 800 nm. The single orbital calculation uses $g_m = 0$ and Eq. 1.32 to make the ADK prediction for the lateral momentum distribution. This is shown as the solid black line in Fig. 3.7 and has the worst agreement with the measurements. Using $g_m = 0$ with Eq. (3.1) to provide the tunnelling filter yields the non-adiabatic single orbital curve. This is shown as the black dashed line in Fig. 3.7. Although it lies closer to the data at low intensity, it disagrees with measurements deeper into the tunnelling regime. In the tunnelling limit $\gamma \to 0$ the quasi-static and non-adiabatic theories converge.

The multi-orbital prediction is shown as the red lines in Fig. 3.7. It is given by Eq. 3.3. In the low intensity limit the contribution of the $|m| = 1$ orbitals is negligible and the multi-orbital theory approaches the single orbital

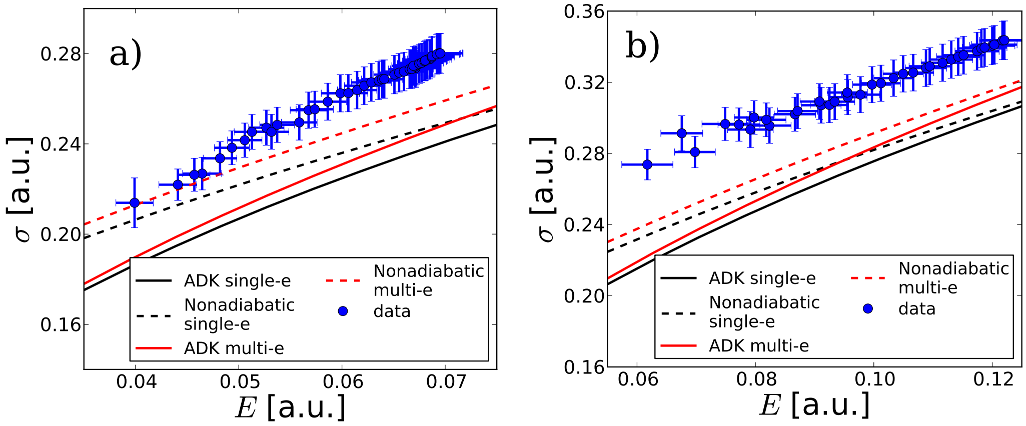

Figure 3.7: Photo-electron lateral momentum distribution at 800 nm as a function of laser field E for (a) Ar, and (b) Ne. The distribution is a Gaussian characterized by its standard deviation σ. The measured values are compared to theoretical predictions using the quasi-static (ADK) or non-adiabatic tunnelling theories. The red lines include the contribution of multiple orbitals in the valence shell of Ar and Ne. The black lines include only the $m = 0$ orbital.

theory. At intermediate and higher laser fields the multi-orbital wavepacket is always broader than the corresponding single orbital wavepacket. The multi-orbital theory calculated using DC tunnelling is shown as the red solid line. It still predicts a lateral wavepacket more narrow than the measurements. Correcting for non-adiabatic effects again increases the wavepacket spread. The non-adiabatic, multi-orbital prediction is shown as the dashed red line. Non-adiabatic effects are responsible for both broadening the tunnel filter Eq. (3.1) and increasing the ionization from $|m| = 1$, as was shown in Fig. 3.6.

Despite the slightly improved agreement obtained by including non-adiabatic effects and contributions from multiple orbitals, the theoretical prediction still lies outside the experimental uncertainty. Hence the explanation must lie beyond the effects considered thus far. Another approach to calculating the size of the lateral wavepacket is using the *quantitative tunnelling formula* (QTF) [73]. By re-deriving the pre-exponential factor in Eq. (1.32) Dreissigacker and Lein obtain good agreement with the experimental result using ionization from $m = 0$ only. As we have seen in this section, adding the contributions from the $|m| = 1$ orbitals does not substantially alter the agreement. The QTF provides the most complete theoretical description of the photo-electron wavepacket.

In Fig. 3.7 we have calculated the photo-electron lateral distribution by adding the different m states incoherently. Incoherent addition is appropriate for ionization of rare gas atoms because the photo-electron and ion are in an entangled state. For ionization of the valence electrons in rare gas atoms, the complete wavefunction is

$$\begin{aligned}|\Psi(t)\rangle = a_N|N\rangle + a_0|I_0(t)\rangle|\chi_0(t)\rangle \\ + a_1|I_1(t)\rangle|\chi_1(t)\rangle + a_{-1}|I_{-1}(t)\rangle|\chi_{-1}(t)\rangle \end{aligned} \quad (3.4)$$

where $|N\rangle$ is the wavefunction of the neutral atom, $|I_m(t)\rangle$ is the wavefunction of the ion created by removal of an electron from orbital m, $|\chi_m(t)\rangle$ is the continuum wavefunction for the photoelectron removed from orbital m, and a_m the respective amplitudes. In the experiment described in section 3.1, the neutral was not observed. Measuring the momentum distribution $|\Psi|^2$ involves cross terms. However, the ion hole states are orthogonal: $\langle I_m|I_n\rangle = \delta_{mn}$ and therefore the cross terms disappear. After the laser pulse has passed one is left with an incoherent addition of amplitudes from the different orbitals:

$$\begin{aligned}\lim_{t\to\infty} |\Psi|^2 = |a_N|^2\langle N|N\rangle + |a_0|^2\langle I_0|I_0\rangle\langle\chi_0|\chi_0\rangle \\ + |a_1|^2\langle I_1|I_1\rangle\langle\chi_1|\chi_1\rangle + |a_{-1}|^2\langle I_{-1}|I_{-1}\rangle\langle\chi_{-1}|\chi_{-1}\rangle. \end{aligned} \quad (3.5)$$

Thus, the different m orbitals do not interfere in strong field ionization of atoms.

In conclusion, the relation between the lateral and longitudinal momentum from tunneling models is accurate when circularly polarized light is used. Our measurements on the rare gas atoms suggest the models are accurate to within 15%. Improved models like QTF are more accurate. This is very important. Tunneling is one of the simplest of quantum mechanical phenomena. It has the robustness on which technologies are built. If laser experiments are accurately described by tunneling, then multi-photon ionization becomes a reliable tool to probe molecules, much like an STM probes solids.

3.2 In-situ laser intensity measurement

As we described in section 1.2 and Fig. 3.1, the photo-electron momentum distribution has a simple dependence on the laser field strength. The drift momentum in the plane of polarization is $p_d = E(t_i)/\omega$. In this section we show how we use the electron momentum spectrum to determine the laser intensity with high precision.

We must distinguish at the outset between the optical intensity and the experimental intensity. The optical intensity I_0 refers to the maximum intensity value in the focus of a $\mathrm{TEM}_{0,0}$ laser mode. As we will show in a moment, the intensity I_0 occurs at just a single point in the laser focus. Since a point occupies zero volume, effectively no particles feel the intensity I_0. For this reason it makes sense to define another intensity, the experimental intensity. This represents the average intensity seen by the particles in the laser focus. We will show that it depends on factors like the optical intensity, pulse duration and transition rate. Only in the low field limit does the experimental intensity approach the optical intensity.

To make a high precision measurement of the experimental intensity using our setup, we must include effects like the initial spread of the electron momentum due to tunnel ionization (see section 3.1), and integration of the focused pulse over the distribution of intensities present. We will show that the intensity distribution in the finite focal volume can be replaced with a single value for the experimental intensity due to the nonlinearity of multiphoton ionization. This is crucial for making direct comparison to theoretical predictions for tunnel ionization. We also show that the retrieved intensity and the quality of the fit is insensitive to spatio-temporal averaging.

Experimentally, we use both velocity map imaging and cold-target recoil ion momentum spectroscopy (COLTRIMS) [92] to test the the quality of our intensity measurement. In both electron and recoil ion momentum spectroscopy experiments we used an 800 nm, circularly polarized light pulse as described in section 2.5. We used a polarizing beam splitter and power meter to determine the ellipticity with an accuracy of 4%. For the ion experiment we used H_2^+ [106]. However, intensity calibration using COLTRIMS can be performed on any atom or molecule provided sufficient resolution in the single ion can be achieved [63, 28]. For the photo-electron experiment, the pulses were 15 fs as in the experiment from section 3.1. Using a short pulse is not essential for applying our method. The method is general enough to apply to a range of pulse durations and intensities.

To model the laser pulse we assume a Gaussian mode propagating along the z axis with electric field

$$E(z,r,t) = \frac{E_0}{\left(1+z^2/z_R^2\right)^{1/2}} \exp\left(-\frac{r^2}{w_0^2\left(1+z^2/z_R^2\right)}\right) f(t) \tag{3.6}$$

where $f(t) \equiv f(z=0,t)$ is the pulse envelope from Eq. (1.1). The optical intensity of the circularly polarized pulse is then $I_0 = cE_0^2/(4\pi)$ in atomic units. The beam spot size is $w^2(z) = w_0^2\left(1+z^2/z_R^2\right)$, where w_0 is the $1/e$ beam radius, and $z_R = \pi w_0^2/\lambda$ is the Rayleigh range. With a Rayleigh length of $z_R = 100\ \mu$m the focus was well contained within the 0.5 mm gas jet. A sketch of the experiment illustrating the co-ordinate system used was shown in Fig. 2.1. To recap, an incident laser pulse propagating along the z axis is focused onto an orthogonally propagating gas jet. The gas jet axis is along x. The electrons or ions created in the laser focus are directed by a DC electric field along the y axis and accelerated onto a distant detector. The detector lies in the xz plane.

The laser focus can be divided into a series of iso-intensity rings. The volume encompassed by a ring at field strength E is

$$V(E,t) = \pi w_0^2 z_R \left(\frac{2}{9}\beta^3 + \frac{4}{3}\beta - \frac{4}{3}\arctan\beta\right) \tag{3.7}$$

where $\beta = \left(E_0^2 f^2(t)/E^2 - 1\right)^{1/2}$. It follows that

$$\frac{\mathrm{d}V}{\mathrm{d}E} = \frac{2\pi w_0^2 z_R}{3E^4}\left(E_0^2 f^2(t) - E^2\right)^{1/2}\left(E_0^2 f^2(t) + 2E^2\right) . \tag{3.8}$$

For the photo-ion measurement we employed COLTRIMS. A constant electric field of ≈2 V/cm accelerates the H_2^+ ions towards a commercial detector consisting of micro-channel plate (MCP) and delay line anode. The detector resolves the ion time-of-flight and impact position. This information gives the full momentum vector of each ion. The small DC electric field used in this experiment is not strong enough to keep high velocity ions on the detector, however, it yields an improved velocity resolution of the H_2^+ ions. The molecular jet in the COLTRIMS chamber is continuous. A series of differentially pumped vacuum chambers and skimmers ensures that the jet is cold in the lateral direction, however, along the jet axis it is much warmer. This creates an uncertainty in the measured ion momentum. In the lateral direction the momentum uncertainty was 10^{-5} a.u., but along the jet axis it

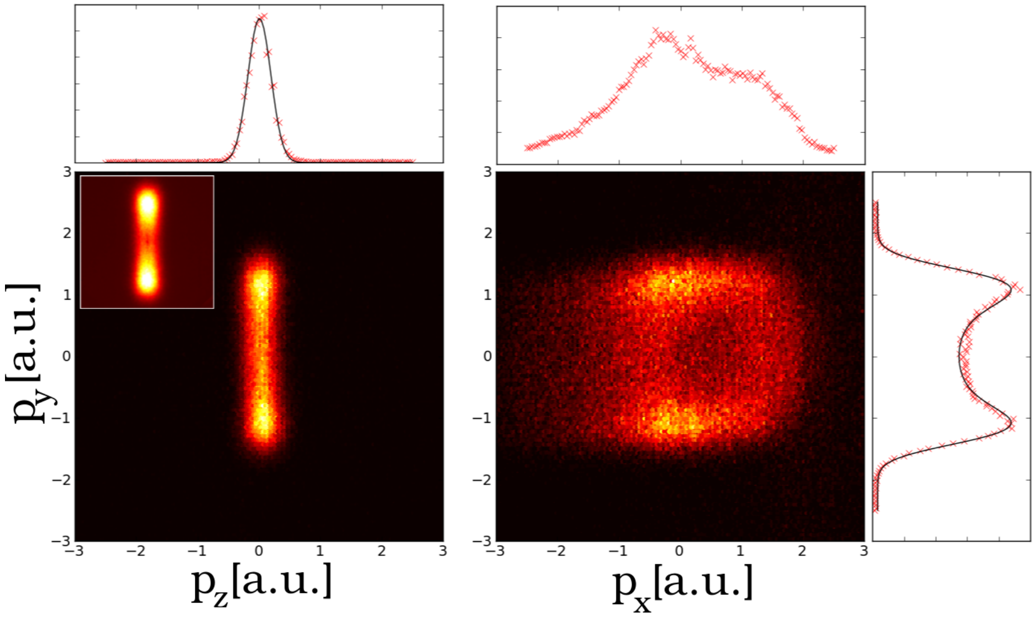

Figure 3.8: Two-dimensional projections of 3-D H_2^+ momentum distributions, and their respective integrals. dN/dp_z is the approximately Gaussian curve which gives the quantum uncertainty due to strong field ionization [69]. dN/dp_x is thermally blurred so much information is lost. However, integrating over this direction yields curves with low uncertainty. The inset figure shows a photo-electron momentum spectrum of from Ar.

was ≈ 0.5 a.u (see Fig. 3.8). This large uncertainty is eliminated in the data analysis by integrating over the jet axis.

For the photo-electron measurements we used the VMI spectrometer described in chapter 2. The method we discuss in this paper can be applied directly to the measured photo-electron spectrum without any inversion of the data, so we do not use any inversion here. As in section 3.1, we corrected the measured spectra for sensitivity and dark signal. The processed image P used for analysis is given by $P = (R - D)\,/\,(S - D)$ where D is a dark image taken with the laser blocked, S is a sensitivity image measured under homogeneous illumination of the MCP and R is the raw photo-electron spectrum measured with both the laser and gas source on. The VMI apparatus used a pulsed gas jet. The momentum uncertainty along the jet axis and in the lateral direction were both 10^{-5} a.u.

In Fig. 3.8 we show the full measured momentum spectrum of H_2^+ ions. An inset shows an example photo-electron spectrum for comparison. For both electrons and ions the yz spectra are very similar indicating the method is applicable to either species. The ion momentum distribution along the gas jet axis (x) is blurred by the thermal velocity distribution in the jet. For electrons this was not a problem because they are much lighter and move faster. In addition, the gas source used in the VMI electron experiment was much colder. For the ions, the distribution in the y direction is not affected and we can obtain a spectrum without thermal blurring by integrating over x. The y axis corresponds to the time-of-flight axis in the spectrometer and is only observable in the electron experiment via tomographic imaging [74]. The xy plane is the plane of polarization, and therefore the spread of the distribution along the z axis is the lateral momentum spread from tunnelling examined in section 3.1. We will show below that an accurate intensity measurement must include this information.

To model the momentum spectrum, we first write the yield from a given iso-intensity shell in the laser focus as

$$\frac{\mathrm{d}N}{\mathrm{d}E} = \left(1 - e^{-\int_{-\infty}^{\infty} W_{l,m}(E(t'))\mathrm{d}t'}\right) \int_{-\infty}^{\infty} \frac{\mathrm{d}V}{\mathrm{d}E}\mathrm{d}t' \ . \tag{3.9}$$

Note that Eq. (3.9) includes saturation of the first ionization state only. Examples of the relative yield from the laser focus are shown in Fig. 3.9. The curves are examples of (3.9) for several different optical intensity values ($I_0 = cE_0^2/(4\pi)$). The field free I_p of argon was used and $Z = 1$. Only by working well below the saturation intensity [108] does the experimental intensity approach the optical intensity.

Using the model it is possible to define the average laser field at which ionization occurs. This corresponds to the experimental intensity,

$$E_{avg} = \frac{1}{N}\int_0^{E_0} E\frac{\mathrm{d}N}{\mathrm{d}E}\,\mathrm{d}E \tag{3.10}$$

This value includes integration over the focal volume and pulse duration. Of course it also depends on the optical intensity through the limits on the integration, and on the transition rate through the yield. This is the most meaningful intensity to use when looking for intensity-dependent features in the momentum spectra (e.g. Freeman resonances [117], or lateral momentum distribution [69]).

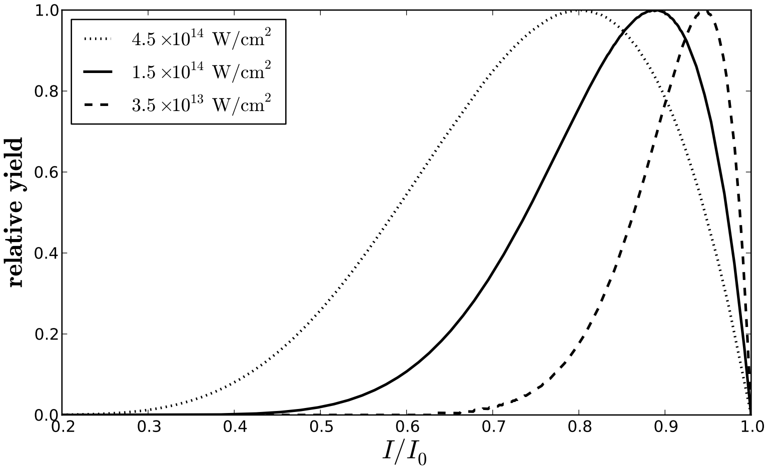

Figure 3.9: Relative yield from the laser focus integrated in space and time. The curves correspond to the function in Eq. (3.9) for three different values of the optical intensity, $I_0 = cE_0^2/(4\pi)$. The medium was neutral argon ($I_p = 15.76$ eV, $Z = 1$) and the pulse was circularly polarized.

The next step is to relate the yield $\mathrm{d}N/\mathrm{d}E$ to the ion or electron drift momentum. Following Refs. [69, 74], we model the momentum distribution in circularly polarized light as a torus:

$$h(E,p) = \frac{1}{\sigma\sqrt{\pi}} \exp\left[-\left(p - \frac{E}{\omega}\right)^2 /\sigma^2\right] \tag{3.11}$$

where σ^2 is the width of the lateral momentum distribution and p is the drift momentum of the tunnel-ionized electron after the pulse has passed. The width σ^2 is the quantum uncertainty from strong field ionization, and it can be measured directly by fitting to the $\mathrm{d}N/\mathrm{d}p_z$ spectrum as we have shown in section 3.1. Taking the limit $\sigma \to 0$ in Eq. (3.11) we obtain the classical expression for the photo-electron or photo-ion drift momentum: $h\,(E,p) = \delta\,(p - E/\omega)$. This was used in Ref. [106]. We will show that rather than taking $\sigma = 0$, measuring it along the z axis offers a much better fit to experimental observations.

Eq. (3.11) is then convolved with the yield from each iso-intensity shell to give the final momentum distribution. Thus $\mathrm{d}N/\mathrm{d}p$ is found by

$$\frac{\mathrm{d}N}{\mathrm{d}p} = \int \frac{\mathrm{d}N}{\mathrm{d}E} h(E,p)\,\mathrm{d}E \quad . \tag{3.12}$$

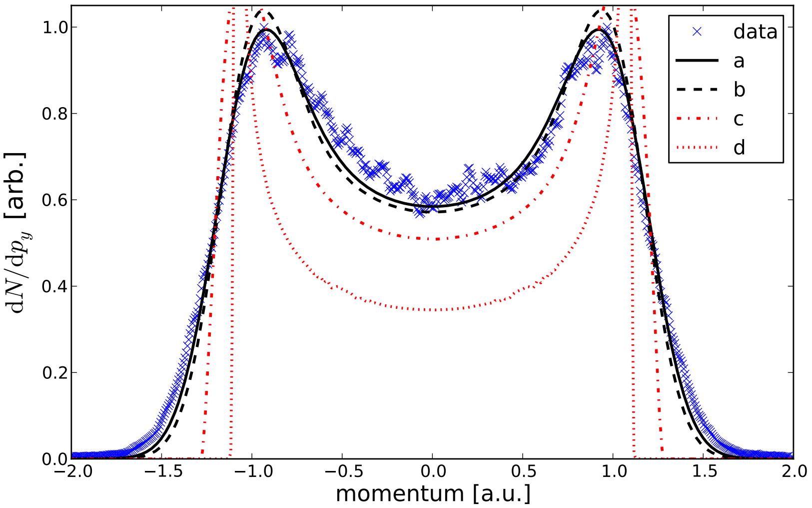

Figure 3.10: Calculated momentum distributions fit to Ar photo-electron spectra at 2.6×10^{14} W/cm^2. Curve labels: (a) Model including the lateral distribution, volume and time integration; (b) with lateral distribution, without volume or time integration; (c) with volume and time integration, without lateral distribution; (d) without volume or time integration or lateral distribution.

Strictly speaking, the size σ of the lateral distribution of the photo-electron or photo-ion depends weakly on intensity [69]. However using a single average value for the lateral distribution over all iso-intensity shells does not significantly affect the results of the model.

To compare with ion spectra or 2-D electron spectra, we must integrate over the molecular beam's propagation direction. For ions, this cancels thermal blurring. Thus,

$$\frac{\mathrm{d}N}{\mathrm{d}p_y} = \int\int \frac{\mathrm{d}N}{\mathrm{d}E} h(E,p)\,\mathrm{d}E\,\mathrm{d}p_x \tag{3.13}$$

represents the curve that can be measured with high accuracy, and will be fitted to experimentally obtained momentum distributions. Eq. (3.13) is the Abel transform of (3.12).

In Fig. 3.10 we compare four curves corresponding to slightly modified versions of the model presented above. Each curve represents the best fit to a measured photo-electron spectrum for argon at 800 nm, 2.6×10^{14} W cm^{-2}.

Curve (a) is the full model including volume and time integration (a 15 fs pulse was used), and the lateral distribution $h(E,p)$. Curve (b) includes the lateral distribution but does **not** include volume or time integration. This is achieved by setting $\mathrm{d}N/\mathrm{d}E = \delta\left(E - E_{avg}\right)$ in Eq. (3.12). Thus model (b) gives the electron a momentum distribution characterized with a single effective laser intensity. Curve (c) is the predicted momentum distribution including volume and time integration, but **not** including the lateral distribution. This means taking $\lim \sigma \to 0$ in Eq. (3.11). Curve (c) is therefore the model of Ref. [106] when the field free I_p and $Z = 1$ are used. Lastly, curve (d) is the result of a model using only the classical expression for the particle's momentum $h(E,p) = \delta\left(p - E/\omega\right)$ without any lateral distribution or spatio-temporal integration. In this case, (3.13) has an analytical solution,

$$\frac{\mathrm{d}N}{\mathrm{d}p_y} = \begin{cases} A\dfrac{E_{avg}/\omega}{\left(E_{avg}^2/\omega^2 - p_y^2\right)^{1/2}} & |p_y| < E_{avg}/\omega \\ 0 & \text{else} \end{cases} \tag{3.14}$$

where A and E_{avg} are the fitting parameters.

We note that the two curves including the lateral distribution are very similar. Both closely resemble the measured spectrum. The curves that do not include the lateral distribution are considerably more sharp – even if spatio-temporal integration is included. In the following we show that the lateral distribution is critical for achieving an accurate fit to measurements. We will show that the full model (a) is the best fit, however, model (b) which ignores spatio-temporal integration and uses a single value for the laser intensity is almost as good.

For the H_2^+ experiment, three parameters were used for fitting $\mathrm{d}N/\mathrm{d}p_x$: laser field E, a constant offset B to compensate for background signal, and peak height A to account for gas density, detector efficiency and experimental yield.

$$F(p_x) = A\frac{\mathrm{d}N}{\mathrm{d}p_x}(E) + B. \tag{3.15}$$

The experiment collecting photo-electrons used only the two fit parameters E and A. Because pulsing the MCP eliminates background noise, we set $B \equiv 0$. The fitting procedure uses a simplex nonlinear optimization algorithm[1] to minimize the value of χ^2 function by varying the fitting parameters. All

---

[1] python's `fmin` from the `scipy` library

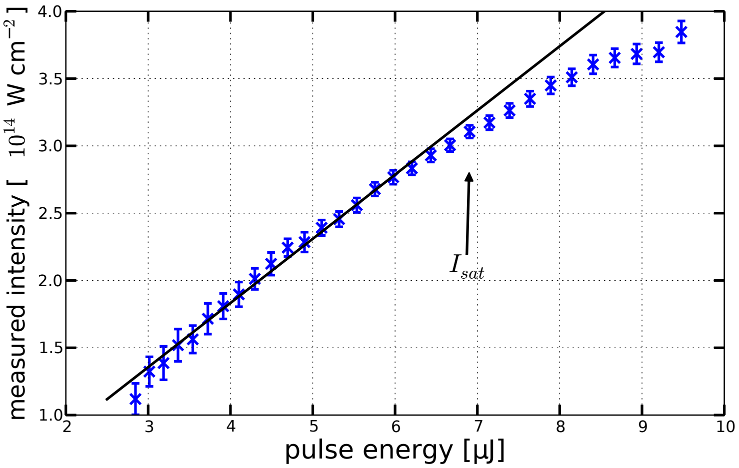

Figure 3.11: Relation between pulse energy and measured peak intensity for the electron experiment (15 fs pulse). At low pulse energy the intensity increases linearly with energy. Once saturation is reached, the relationship deviates from linear.

other values in the algorithm are measured or known (e.g. wavelength, pulse length, I_p, Z). The goodness of fit is evaluated by the magnitude of χ^2_ν i.e. χ^2 divided by the number of degrees of freedom [118].

In Fig. 3.11 we show how the relation between pulse energy and intensity scales. Below saturation the intensity increases linearly with pulse energy. Once saturation is reached the momentum distribution continues to broaden but deviates from the original line.

To quantify the accuracy of the fit, we measure photo-electron spectra from Ar at 31 different laser pulse energies. At each pulse energy a photo-electron spectrum was recorded and the four different models were fit to the measurement. The best fit theory allows us to determine the laser intensity corresponding to a particular spectrum. By evaluating many spectra we can evaluate the accuracy of each theory and identify the relative importance of spatio-temporal averaging and the lateral distribution. The resulting reduced χ^2 values for each spectrum are shown in Fig. 3.12. In Fig. 3.12 there are data markers for each of the four models. The reduced χ^2 for model (a), including the volume and time integration and lateral momentum distribution, is shown as the blue circles. Model (b), including the lateral distribution but not including spatio-temporal integration, is shown as the green × markers and

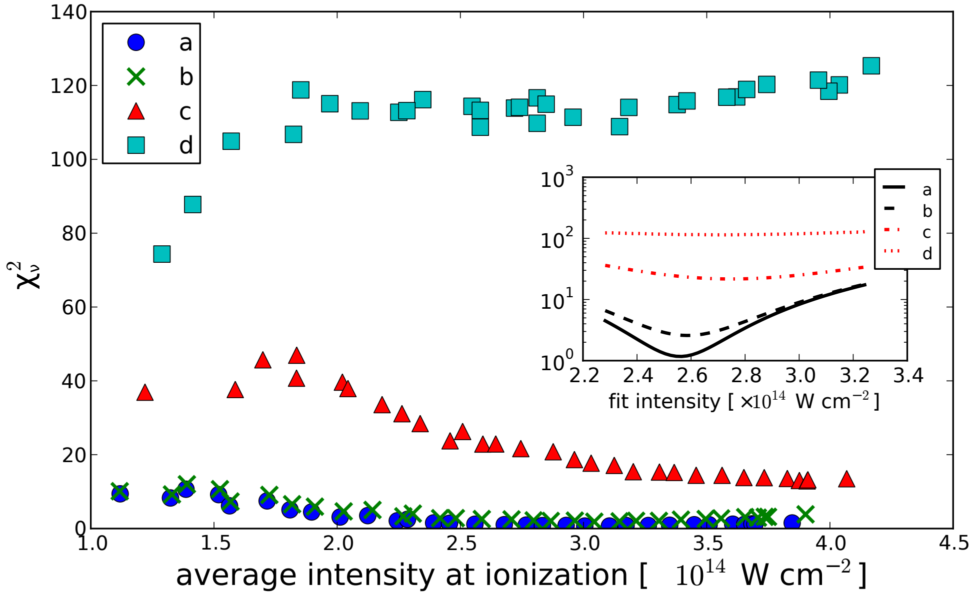

Figure 3.12: Goodness of fit for Ar at 800 nm over a range of laser intensities. The reduced χ^2 statistic is shown for fitting with different models. Inset: Example χ^2_ν function for a single spectrum at 2.55×10^{14} W cm^{-2}. Model labels: (a) With lateral distribution, volume and time integration; (b) with lateral distribution, without volume or time integration; (c) with volume and time integration, without lateral distribution; (d) without volume or time integration or lateral distribution.

is slightly larger than model (a). However, the reduced χ^2 values are still quite small for model (b) compared to model (c) or (d). Also shown are models (c) and (d) as the red triangles and green squares. Models (c) and (d) do not include the lateral distribution and have considerably larger χ^2_ν values.

Fig. 3.12 shows that the best fit – that is, the smallest χ^2_ν – is obtained for the full model (a). However, model (b) is very close. Models (c) and (d) which do not include the lateral distribution have substantially larger reduced χ^2. This is consistent with Fig. 3.10 where it is clear that curves (a) and (b) much more closely resemble the measured spectrum.

The agreement of models (a) and (b) illustrates the importance of including the lateral distribution (i.e. the quantum uncertainty) in fitting to the measured spectrum in the plane of polarization. The complete model including the lateral distribution and spatio-temporal integration is the most accurate fit. By comparing the increase in χ^2_ν for model (b) to the increase for model (c), we observe that the lateral distribution is of more significance than spatio-temporal averaging. The result for model (b) shows that the distributions can be accurately described by a single laser intensity – ignoring spatio-temporal averaging – provided the quantum mechanical lateral distribution is included.

The goodness of fit is further explained in the inset to Fig. 3.12. This shows an example of the reduced χ^2 function for a single spectrum recorded at 2.55×10^{14} W cm^{-2}. The inset shows the value of the optimization parameter χ^2_ν as a function of the laser field E used to fit the distribution via Eq. (3.15). In the inset the intensity is a fitting parameter. It is assumed the minimum χ^2_ν corresponds to the true intensity value. We see that the minimum reduced χ^2 value occurs for model (a) as expected. Model (b) is a slightly less good fit. Models (c) and (d) are poor fits and have reduced χ^2 values larger by an order of magnitude or more. The substantially larger value of χ^2_ν for the models that do not include the lateral distribution illustrates that the lateral distribution is more significant than spatio-temporal averaging. Comparing curves (a) and (b), we see that curve (a) has a very well defined minimum compared to model (b). This is consistent with the results in the main figure. For spectra containing more than 10^5 photo-electrons, we estimate the precision of the fit using model (a) is 4% in intensity. Similar results are obtained for fits to other measured spectra. The complete model (a) is the most precise intensity measurement.

In addition to the uncertainty in the fit, there are other experimental uncertainties associated with momentum calibration (2% in σ and 2% in E), laser ellipticity (2% in E), detector sensitivity (1% in σ), and chamber alignment (1% in σ). When combined with the fit uncertainty, the total accuracy of the intensity measurement is 8% in I.

In conclusion, we have demonstrated how the measured photo-electron spectrum in the tunneling limit is applied to make an *in-situ*, high precision measurement of the experimental laser intensity. In general, the experimental intensity value is different from the optical intensity, however, the two are very similar when well below saturation. The experimental intensity is the correct value to use when comparing to theory since it is the value that creates the physical effects seen by a measurement. We have applied this intensity measurement method for comparing the photo-electron lateral wavepacket to tunneling theory in section 3.1. We continue to use it in the next section where we study the conservation of photon momentum.

3.3 Partitioning of the photon linear momentum

It is well known that light carries both energy and momentum. In the high frequency limit the momentum of radiation manifests as Compton scattering. At optical wavelengths the momentum transfer during light absorption has found many applications like laser tweezers [119], cooling and trapping [120] and the "optical spanner" [121]. Despite it's interest from both a fundamental and applied perspective, the momentum of light is almost always neglected in strong field light-matter science. In Chapter 1 we described how tunnel ionization emerges from the description of light matter interaction in strong, infrared laser fields. As we noted, tunnelling is a DC concept and is valid in the electric dipole approximation. There is no momentum in the theoretical description of laser tunnelling because there are no photons. In this section we examine the linear momentum absorption in strong field ionization. It arises from an interaction between the photo-electron and the light magnetic field. We consider how the conservation of photon momentum is satisfied by dividing it between the photo-electron, ion, and light field. Until now this fundamental problem in atomic-molecular-optical physics has not been addressed. Recently, however, it has become a hot topic due to the role of radiation pressure in creating longitudinal currents that emit terahertz radiation [122, 123, 124, 125].

Previous studies of the photon momentum transfer were performed at relativistic intensities and the long pulse regime. In these conditions the ionization potential I_p is negligible and the photo-electron exits the focus in the presence of the high intensity pulse [126, 127]. In our experiment the photo-electron kinetic energy is comparable to I_p and the photo-electron remains in the focus for the duration of the pulse. These conditions are similar to most THz generation experiments [128].

3.3.1 Theory

As we discussed in section 1.3.3, the total energy absorbed in multi-photon ionization (MPI) is given by the number of photons $N\hbar\omega = I_p + K + U_p$, where I_p is the ionization potential of the atom, K is the drift kinetic energy of the electron measured after the event and U_p is the ponderomotive energy of the electron. Photo-electron distributions of MPI clearly reveal the quantized nature of the transfer of energy (recall Fig 1.8). Likewise, the transferred linear momentum must be conserved $N\hbar k = p_z^e + p_z^i + p^L$ where z is the direction of light propagation and the superscripts denote the momenta of photo-electron, photo-ion, and laser field, respectively.

In chapter 1 we developed the classical model of an electron born at time t_i in the presence of a strong electromagnetic wave. By ignoring the light magnetic field we were able to derive a set of expressions for the particle's position and momentum (1.8), (1.9). We now re-introduce the magnetic field as a second order correction on the electric-dipole expressions, still in the non-relativistic regime.

Substituting in (1.8) we have

$$\dot{\boldsymbol{p}}^{(2)} = \frac{q}{m}\boldsymbol{p}^{(1)}(t) \times \boldsymbol{B}(t) \tag{3.16}$$

$$\begin{aligned} \dot{p}_z^{(2)}(t) &= \frac{q^2 E_0^2 f^2(t)}{\omega m c}\Big(\sin\omega t\cos\omega t\left(1-\epsilon^2\right) \\ &\qquad - \sin\omega t_i \cos\omega t + \epsilon^2\cos\omega t_i \sin\omega t\Big) \ . \end{aligned} \tag{3.17}$$

For circularly polarized light this leads to the following expression for the photo-electron momentum in the presence of the oscillating field,

$$\begin{aligned} p_z^{(2)}(t) &= \frac{q^2 E_0^2}{mc\omega^2}\left(f^2(t_i) - f^2(t)\cos\omega(t-t_i)\right) \\ \lim_{t\to\infty} p_z^{(2)}(t) &= \frac{q^2 E_0^2}{mc\omega^2} = \frac{K+U_p}{c} \end{aligned} \tag{3.18}$$

where K is the photo-electron's drift kinetic energy in circularly polarized light (see section 1.2). We note that the Lorentz force is independent of the sign of q and always gives a positive momentum in the direction of propagation.

As the laser pulse envelope passes the photo-electron, there is an additional contribution to the momentum along the propagation axis. This is from the gradient in the ponderomotive energy seen by the electron as the laser pulse passes it. This is a gradient in time, but it is equivalent to a gradient in space. The contribution to p_z is

$$\begin{aligned} \dot{p}_z^{(3)} &= -\nabla U_p(z,t) \\ &= -\frac{\partial}{\partial z}\frac{q^2E_0^2(1+\epsilon^2)}{4m\omega^2}e^{-(z-ct)^2/c^2\tau^2} \\ p_z^{(3)} &= -\frac{q^2E_0^2(1+\epsilon^2)}{4m\omega^2}\int_0^\infty -\frac{2(z-ct)}{c^2\tau^2}e^{-(z-ct)^2/c^2\tau^2}\mathrm{d}t \\ &= -\frac{U_p}{c}\ . \end{aligned} \tag{3.19}$$

In deriving (3.19) we have made the approximation $z = 0$ after taking the gradient. This is valid when the pulse is short. The ponderomotive gradient term $p_z^{(3)}$ always removes the momentum U_p/c from the photo-electron, independent of the pulse duration. The net z momentum for the photo-electron in a circularly polarized light pulse is

$$p_z = p_z^{(2)} + p_z^{(3)} = \frac{K}{c} \tag{3.20}$$

Eq. (3.20) shows that a free electron always has a net positive momentum as a result of absorbing the energy K. It is created in the presence of a strong field and initially also absorbs the ponderomotive energy U_p. However, that energy and the associated momentum U_p/c are returned to the field as the pulse passes the electron ($p^L = U_p/c$). We confirmed the validity of (3.20) using a numerical simulation to the complete Lorentz equation of motion including the pulse envelope (1.7).

It is significant that energy and momentum are returned via a blue shift in the wavelength of the light pulse, not re-emission of photons at the incident frequency [129, 130]. This can be demonstrated by considering the macroscopic reponse of a plasma on an incident light wave. The phase of the wave is $\phi(t) = \omega t - n(t)kz$ where n is the index of refraction and k the wavenumber. In a plasma the index of refraction is given by

$$n = \sqrt{1-\frac{\omega_p^2}{\omega_0^2}} = \sqrt{1-\frac{\rho(t)e^2}{\epsilon_0 m_e\omega^2}} \tag{3.21}$$

where the plasma frequency in SI units is $\omega_p^2 = \rho e^2/(\epsilon_0 m_e)$ and ρ is the free electron density. Since ρ can only increase by ionization with a femtosecond pulse, the index can only decrease and therefore the frequency shift $\Delta\omega = \partial\phi/\partial t - \omega$ always increases. At a single electron level the index change is negligible for the pulse, however, for the single atom physics it is not. It can be shown that at the single electron level the index change and accompanying blue shift of the driving field *exactly* removes the poderomotive energy [129]. The corresponding momentum U_p/c must also be removed by the blue shift. The blue shift has further consequences for angular momentum conservation, a problem that we examine in section 3.4.

3.3.2 Experiment

We used circularly polarized laser pulses at 800 nm, 15 fs (intensity FWHM) and 1400 nm, 70 fs to ionize Ar or Ne atoms. The energy of the 800 nm pulse was controlled using a half-wave plate and two germanium plates positioned at Brewster's angle. The energy of the 1400 nm pulse was controlled using a neutral density filter. Our experiment spans the intensity range from $10^{14} - 10^{15}$ W cm^{-2}. At these intensities and wavelengths, the photo-electron drift velocity is less than 2% of the velocity of light.

We measure the photo-electron momentum using the VMI spectrometer described in chapter 2. The spectrometer projects the 3-dimensional electron momentum distribution onto a 2-dimensional imaging detector (Fig. 3.13(b)). The detector plane contains the direction of laser propagation (z) and the axis of the gas jet (x). The laser pulses were focused into the supersonic gas jet with a local density of $\approx 10^8$ cm^{-3}. The velocity distribution of the atoms in our pulsed gas jet corresponds to a spread in the electron momentum distribution of $< 1.5 \times 10^{-5}$ a.u. (atomic units - a.u.).

The nominal spectrometer momentum resolution, determined by its pixel size, is 7×10^{-3} a.u. for Ar and 1×10^{-2} a.u. for Ne. However, we have shown in section 3.1 how multi-photon ionization creates a Gaussian wave packet in momentum space along the laser propagation k-direction. The wavepacket is much broader than the nominal resolution. A typical wavepacket that we measure is shown as the crosses in Fig. 3.13(d). Taking the centroid of this distribution, we can determine a shift between momentum distributions obtained under differing conditions with an accuracy of $\sim 2 \times 10^{-3}$ a.u. Since the linear momentum of a single 800 nm photon is 4×10^{-4} a.u., we are sensitive to a momentum shift caused by the absorption of ≈ 5 photons.

To determine the absolute shift we use electrons extracted from Rydberg states that are populated by multi-photon excitation [32, 33] as a reference.

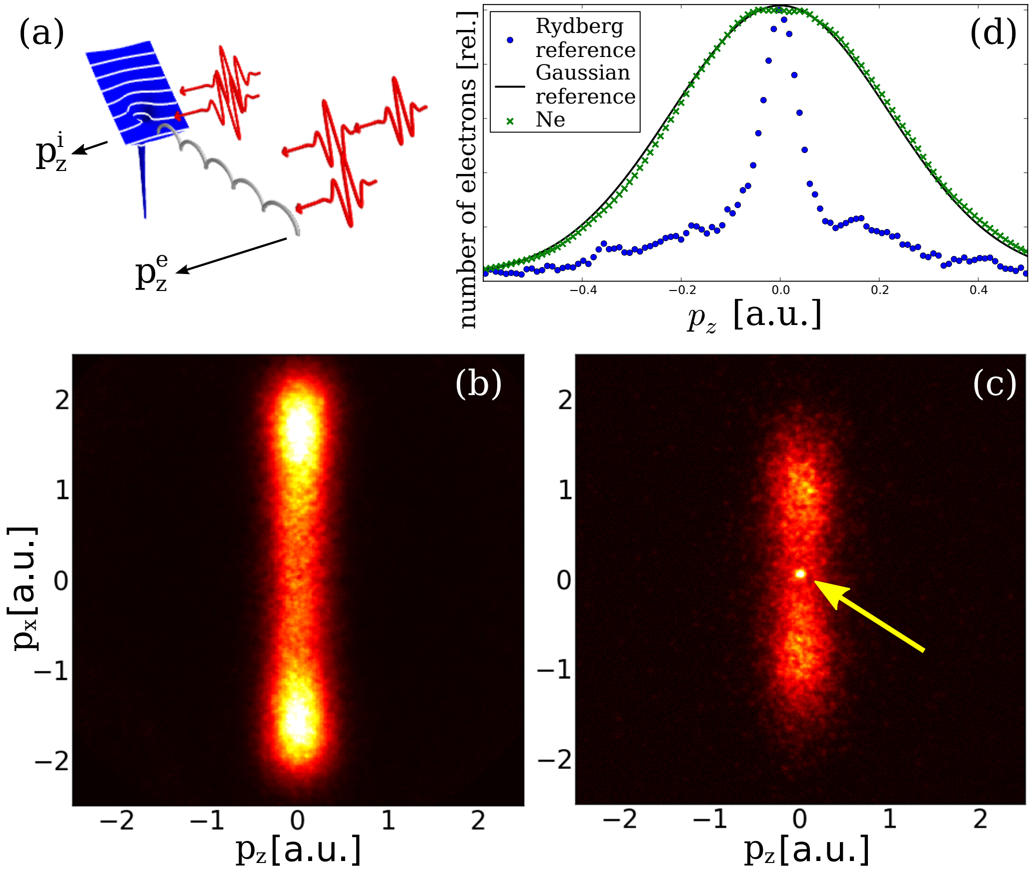

Figure 3.13: (a) Photo-ionization of a neutral atom gives a net momentum to the photo-electron $p_z^e = K/c$ and the ion $p_z^i = I_p/c$ in the direction of light propagation. (b) Measured electron momentum spectrum (in atomic units) of Ne in circularly polarized light at 800 nm, 8×10^{14} W/cm^2. The laser pulse propagates along the z-axis. (c) Background image under the same conditions as in (b) reveals a distinct peak of low energy electrons from laser produced Rydberg atoms that are ionized by the spectrometer DC field (indicated by the arrow). (d) The measured Ne photo-electron distribution (crosses) is compared to the Rydberg reference distribution (dots) and a reference Gaussian distribution centred at $p_z = 0$. The centre of the Ne distribution has a net $p_z > 0$.

The lifetimes of these Rydberg states can easily exceed the duration of our laser pulses. When the laser pulse passes, atoms left in highly excited Rydberg states can be ionized by the spectrometer's DC electric field, resulting in very narrowly distributed, low momentum electrons (see Fig. 3.13(c)). The Rydberg states are most efficiently populated in linear light. However, the water vapor in the background gas provides Rydberg electrons even in circular polarized light. We estimate that the electrostatic fields of the spectrometer 0.6 kV/cm $\leq E_{stat} \leq$ 1.3 kV/cm can field ionize Rydberg states with $n \geq 20$.

Rydberg electrons provide an unambiguous reference for zero momentum. The Rydberg atom or molecule has absorbed approximately $N = I_p/(\hbar\omega)$ photons. Since the multi-photon absorption and ionization steps are decoupled in Rydberg atoms, the linear momentum I_p/c is transferred to the center of mass of the atom [33]. Hence, the origin of the Rydberg electron distribution coincides with zero velocity in the lab frame. By recording many Rydberg electron spectra for a range of laser intensities (shown in Fig. 3.14b) we determine the origin of the momentum distribution with an accuracy of 1×10^{-3} a.u.

As we discussed in section 3.1, using circularly polarized light has two important advantages over linear polarization. It avoids Coulomb focusing [29] in the electron momentum distributions and provides a simple measure for the laser intensity (see section 3.2). In circular polarization the electron momentum distribution resembles a torus [74] whose radius is proportional to the peak of the laser field experienced by the neutral atoms. Since we are only interested in single ionization this is the appropriate intensity measure. Following the method of section 3.2 we determine the light intensity with a precision of 8% [131], thereby directly measuring the net number of photons absorbed for a typical electron at that intensity.

For the data analysis we integrated the measured 2-D spectra over x to arrive at a 1-D distribution along the axis of laser propagation (the crosses in Fig. 3.13d). We use a nonlinear fitting routine to fit the centre, width, amplitude, and noise-floor of a Gaussian distribution to the measurements.

In Fig. 3.14 the intensity dependence of the centre of the distribution, $\mathrm{d}N/\mathrm{d}p_z$, is shown for multi-photon ionization in 800 nm and 1400 nm of neon (circles) and argon (triangles, crosses). The intensity dependent momentum transfer has a different slope for the two wavelengths as is expected from the wavelength dependence of the asymptotic electron kinetic energy $K = q^2E_0^2/\left(2m\omega^2\right)$ [11]. Generally, with increasing intensity the centre of dN/dp_z

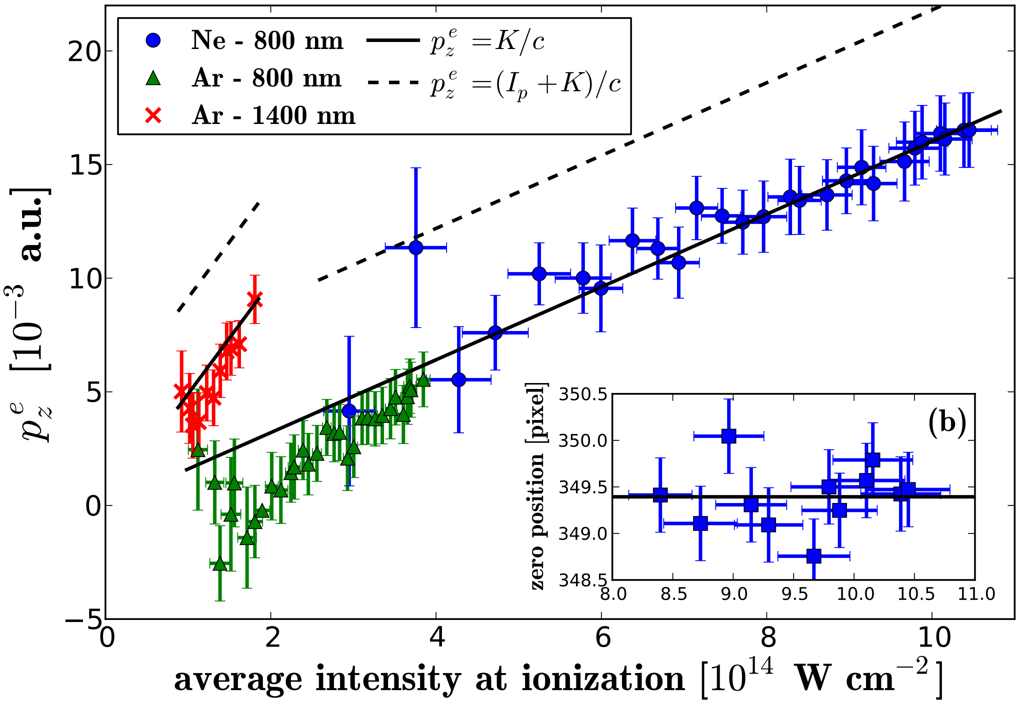

Figure 3.14: (a) The centre of the electron momentum distribution along z as a function of the average intensity at ionization for Ar and Ne at 800 nm and 1400 nm. The intensity at ionization is determined from the electron p_x distribution averaged over the ionization volume (space) and laser pulse length (time; see text for details). The theory lines are given by Eq. (3.20). (b) The zero position of the momentum distribution along the z axis as a function of laser intensity. The position is determined by the centre of the Rydberg electron spot indicated by the arrow in Fig. 3.13c.

is increasingly shifted in the direction of propagation. The upper limit of intensity arises because of saturation of single ionization, when a further increase of pulse energy does not result in an increase in the intensity seen by the neutral atoms. The actual saturation intensity depends on the ionization potential and the pulse duration (70 fs at 1400 nm, and 15 fs at 800 nm).

We have seen in section 3.3.1 what the semi-classical model predicts for the net forward momentum of the photo-electrons (3.20). Eq. (3.20) agrees with the experimental data in Fig. 3.14. For comparison, in Fig. 3.14, we also plot Eq. 3.20 plus a constant offset I_p/c. The dashed line, which includes

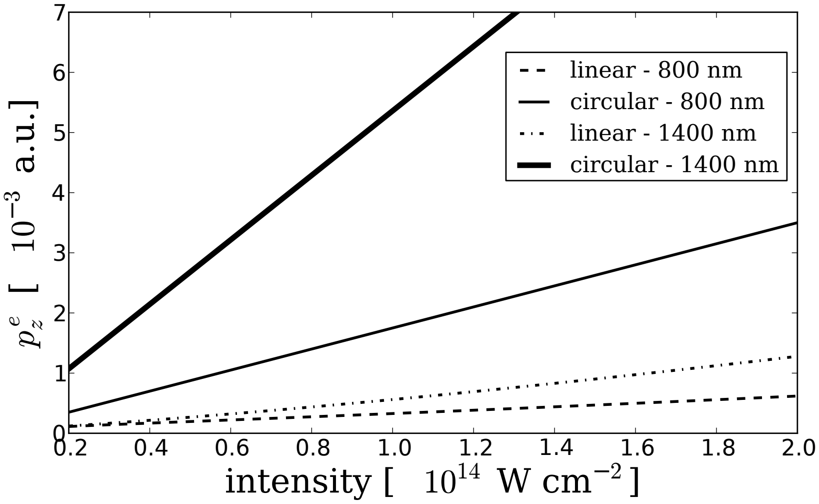

Figure 3.15: Net photo-electron longitudinal momentum p_z^e vs laser intensity calculated for linear and circularly polarized light. The curves are calculated from Eq. (3.20) using the kinetic energy averaged over one optical cycle.

this offset, overestimates the measured p_z^e well beyond our experimental uncertainty. Thus, we conclude that the portion of the longitudinal momentum I_p/c, corresponding to the photons necessary to overcome the ionization energy, is not given to the photo-electron. It must be transferred to the centre of mass of the electron-ion system ($p_z^i = I_p/c$).b

The agreement between Eq. 3.20 and the measurement allows us to draw another conclusion. It shows that the ponderomotive energy does not transfer any net momentum to the electron. This is because the ponderomotive term $p_z^{(3)}$ removes that part of the longitudinal momentum as the pulse passes the electron. The plasma-induced phase modulation of the pulse [129] returns the momentum $p^L = U_p/c$ to the photon field. This is in agreement with the calculation for $p_z^{(3)}$. If the ponderomotive energy were necessary, the slope in Fig. 3.14 would be different by a factor of two – well outside the error bars. This conclusion means that linearly and circularly polarized pulses will transfer very different longitudinal momentum to the photo-electrons. In linearly polarized light most of the energy absorbed by the electron upon ionization is ponderomotive energy and is therefore returned to the field. In circularly polarized light, half the absorbed energy is in U_p and half in K. The momentum associated with K remains with the photo-electron p_z^e.

In Fig. 3.15 we compare the photo-electron longitudinal momentum calculated for circularly and linearly polarized light at two different wavelengths. In both cases we have used Eq. 3.20 to calculate the longitudinal momentum. Circular and linear polarization have very different kinetic energy distributions and this affects the net longitudinal momentum of the photo-electrons when averaged over one optical cycle. In circularly polarized light, the ionization probability is independent of the phase of the field. In linear polarization, the ionization probability and the kinetic energy strongly depend on the phase. Recall from section 1.2 that an electron ionized at the phase ωt_i in linear polarization has drift kinetic energy

$$K(t_i) = \frac{q^2 E_0^2}{2m\omega^2} \sin^2 \omega t_i. \tag{3.22}$$

The average kinetic energy in linearly polarized light is

$$\langle K \rangle = \int_{-\pi/\omega}^{\pi/\omega} K\left(t_i\right) \frac{\mathrm{d}N}{\mathrm{d}t_i}\, \mathrm{d}t_i \tag{3.23}$$

where t_i is the time of ionization and $\mathrm{d}N/\mathrm{d}t_i = W\left[E\left(t_i\right)\right]$ is the Yudin-Ivanov sub-cycle ionization rate [58]. In general $\langle K \rangle$ in linearly polarized light is much less than in circular polarization at a constant intensity. In reality, the limiting intensity in filamentation experiments is determined by dynamic balancing between ionization and plasma defocusing [128]. Therefore, it is more natural to compare linear with circular polarization at the same *ionization yield*. A circularly polarized pulse will reach the same ionization yield at roughly double the intensity of a linearly polarized pulse. This gives an additional enhancement to the charge separation using circular polarization. In addition, re-collisions with the parent ion will strongly affect the electron motion in linear polarization.

Most filamentation experiments take place at an intensity $\sim 5 \times 10^{13}$ W cm^{-2} (linear polarization) or $\sim 1 \times 10^{14}$ W cm^{-2} (circular polarization). For 800 nm light interacting with air, the kinetic energy per electron will be $\sim$ 1 eV for linear and $\sim$ 6 eV for circular polarization so the longitudinal momentum transferred ($p_z^e = K/c$) is similar in magnitude. In the tunneling limit $K_{circ} \approx 25\langle K \rangle_{lin}$ so we expect a much larger current for filamentation using circular polarization.

There are two important implications of our results. First, there has been a debate about the proper role of tunneling in multi-photon ionization [31, 132]. It is clear that tunneling – a DC phenomenon – provides no mechanism to transfer linear momentum to the ion. Although tunneling is a tremendous computational tool, our experiment shows that it remains an approximation. To our knowledge, how the momentum I_p/c is shared between the electron and ion has never been addressed before in experiments, simulations, or models.

Second, the photon momentum transfer to the electron has been invoked to account for THz generation in filaments [122, 123, 125]. In the low fields typical of atmospheric gas breakdown, the momentum transfer will be very small for linearly polarized light. Our results suggest this can be augmented by using circular polarization and longer wavelength. This difference is explored in a recent manuscript where current flows are measured in filaments [125].

3.4 Angular momentum conservation

Having discussed energy and linear momentum conservation in multi-photon ionization, let's now turn to angular momentum. Angular momentum conservation yields the well known dipole selection rules for electron transitions [115] and affects the angular distributions in photo-ionization. Recall from Fig. 1.8 how the angular distributions of ATI electrons change with the absorption of each additional photon. In a circularly polarized laser pulse all photons carry $\pm\hbar$ (positive or negative depending on helicity). The total angular momentum absorbed in multi-photon ionization is $N\hbar = (I_p + K + U_p)/\omega$. Similar to the problem of linear momentum, all the photon angular momentum absorbed at ionization must be transmitted to the electron-ion-light field system.

We begin again with the classical equations of motion (1.8)-(1.9). We will ignore the magnetic field for now and set $\boldsymbol{p}_i = 0$, however, let's allow the photo-electron to have an initial offset. Based on the tunnelling picture in section 1.3.1, the electron's initial position at ionization is not zero, but rather at the exit of the potential barrier: $\boldsymbol{r}_i = \frac{I_p}{qE_0}[\cos\omega t_i\ \hat{\imath} + \sin\omega t_i\ \hat{\jmath}]$. Inserting this in (1.9) we can write the photo-electron's asymptotic position and momentum as,

$$\begin{aligned}\lim_{t\to\infty} \boldsymbol{p} &= \frac{qE_0}{\omega}\left[-\sin\omega t_i \;\hat{\imath} + \cos\omega t_i \;\hat{\jmath}\right] \\ \boldsymbol{r} &= \frac{qE_0}{m\omega^2}\left[(\cos\omega t_i - \omega(t-t_i)\sin\omega t_i)\;\hat{\imath} + (\sin\omega t_i + \omega(t-t_i)\cos\omega t_i)\;\hat{\jmath}\right] \\ &\quad + \frac{I_p}{qE_0}\left[\cos\omega t_i \;\hat{\imath} + \sin\omega t_i \;\hat{\jmath}\right] \;.\end{aligned}$$

Using these we can calculate the angular momentum of the photo-electron after the pulse has passed

$$\begin{aligned}\boldsymbol{L} &= \boldsymbol{r}\times\boldsymbol{p} \\ &= \left(\frac{q^2E_0^2}{m\omega^3} + \frac{I_p}{\omega}\right)\hat{k} \\ &= \frac{U_p + K + I_p}{\omega}\;\hat{k}. \qquad (3.24)\end{aligned}$$

This says that all the angular momentum $N\hbar$ is transferred to the photo-electron. The angular momentum $(U_p + K)/\omega$ is associated with it's classical oscillation in the circularly polarized field, while the angular momentum I_p/ω comes from the initial offset in position at the edge of the potential barrier. Very recent results on photo-electron spectra lend support to the concept that the electron's initial position is at the edge of the tunnel barrier [37].

How is it possible that all the angular momentum is given to the photo-electron and none to the ion or field? We saw in sections 1.3.3 and 3.3 that the energy U_p and linear momentum U_p/c are not in the photo-electron – they are returned to the field after the pulse passes. The angular momentum is not returned, however, because the electron loses the energy U_p via a blue shift of the field [129]. The existing photons in the field are slightly shifted to shorter wavelength as the pulse passes the free electron. This happens whenever plasma is created [130], and it explains why the electron loses energy and longitudinal momentum. In contrast to the longitudinal momentum, a photon preserves its angular momentum as it shifts frequency. Therefore the medium absorbs all of the angular momentum that it is given.

This angular momentum will have a major influence on the medium and is capable of creating a THz magnetic field [133]. The magnetic dipole per electron is $\mu = q^3E_0^2/\left(2m^2\omega^3\right)$ which is several Bohr magnetons at common experimental conditions in filamentation. For air at 800 nm and assuming only 10^{-3} ionization fraction the resulting macroscopic field is on the order of μT. For a completely ionized gas at 2 μm, a THz magnetic field of 1 T or more is feasible. Furthermore, it was recently shown that Laguerre-Gaussian beams carrying orbital angular momentum can enhance the strength of the induced magnetic field by transferring both spin and orbital angular momentum [134]. Thereby unusual plasmas could be created, that may be a source of unique magnetic field structures.

Chapter 4

Molecules in Strong Laser Fields

Molecules are a natural extension of the preceding work on strong field ionization of atoms. Molecules are more physically complex; their rotational and vibrational degrees of freedom provide more experimental opportunities to control matter with a strong laser field. Controlled photo-ionization of molecules can therefore provide more information than the atomic case where there are no “levers”. By studying molecules we can begin to use strong field techniques to manipulate and image the creation and annihilation of chemical bonds. Laser techniques in tandem with ultracold molecular beams [135] could be used to create exotic molecules for applications in science or pharmacy.

Molecules are generally spatially larger than atoms and have a higher density of states. The tunnelling assumptions that work extremely well for multi-photon ionization of atoms may break down for some large molecules and provide opportunities to examine multi-electron effects [66, 67, 42] and electron correlation [136, 137, 138] using strong laser fields.

In this chapter we examine ionization of molecules by infrared femtosecond pulses. We perform a series of pump-probe experiments where we use a lower intensity non-resonant pump pulse to align the molecular axis in the lab frame of reference. We then use a higher intensity circularly polarized probe pulse to singly ionize the molecule and recorded the molecular frame photo-electron angular distribution (MF-PAD) using the VMI spectrometer of Chapter 2. By using circularly polarized light we can isolate the angle-dependent tunnelling current from re-collision and Coulomb interaction with the parent ion. Our results show how the tunnelling current maps into the MF-PAD and provides insight into the symmetry of the ionizing orbital.

4.1 Molecular Alignment

A prerequisite for studying molecular ionization in strong fields is the ability to control molecules in space and time. The temporal resolution of femtosecond laser pulses is much finer than rotational time scales and similar to the vibrational period of many light molecules. Spatial resolution comes from using the laser field to align the molecular axis in the lab frame. Although certain effects like suppressed ionization survive rotational averaging [62], control over the molecular frame is essential for time-resolved experiments on ultrafast electronic imaging. In the following we briefly outline the theory of laser alignment of molecules. Recent reviews are references [139, 140, 141].

4.1.1 Theory

In the absence of an external field, the Hamiltonian for a rotating particle is [142]

$$H = \sum_i \frac{J_i^2}{2I_{ii}} \tag{4.1}$$

where I_{ii} is the momentum of inertia about axis i and $J_i = I_{ii}\omega_i$ is the angular momentum. For a particle like the one sketched in Fig. 4.1 two axes are identical. Therefore the Hamiltonian is

$$H = \frac{J_1^2 + J_2^2}{2I_\perp} + \frac{J_3^2}{2I_\parallel} = \frac{J^2}{2I_\perp} + \left(\frac{1}{2I_\parallel} - \frac{1}{2I_\perp}\right) J_3^2 \tag{4.2}$$

where $J^2 = J_1^2 + J_2^2 + J_3^2$, $I_\parallel$ is the moment of inertia along the main axis of the molecule and $I_\perp$ is in the perpendicular direction. For a quantum system, the angular momentum is replaced by angular momentum eigenvalues $\hat{J}^2\psi = \hbar^2 J(J+1)\psi$. The kinetic energy of a quantum rigid rotor is therefore

$$K = \frac{J(J+1)\hbar^2}{2I_\perp} + \left(\frac{1}{2I_\parallel} - \frac{1}{2I_\perp}\right) \hbar^2 J_3^2 \tag{4.3}$$

Note that for a linear quantum rotor $J_3 = 0$ by symmetry. Hence for a linear rotor the rotational level spacing of the ground state is $\hbar^2/I_\perp$ and the period

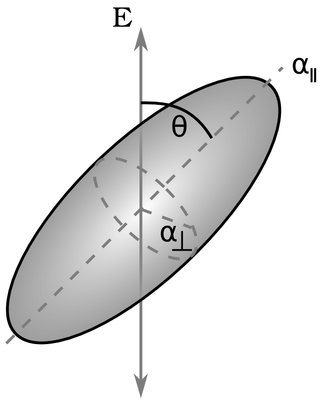

Figure 4.1: A molecule is represented as an ellipsoid located at an angle θ with respect to the laser polarization axis. The main molecular axis has polarizability $\alpha_\parallel$ and moment of inertia $I_\parallel$. The minor axes have polarizability $\alpha_\perp$ and moment of inertia $I_\perp$.

$T_R = 2\pi I_\perp/\hbar$. This is the period for a full revival of a rotational wavepacket. The rigid rotor model compares relatively well to the data from spectroscopic measurements for rotational period (appendix B). A more complete treatment of the problem must include centrifugal distortion of the molecular bonds [142].

Laser alignment of molecules occurs when a strong non-resonant pulse induces a dipole in the molecular frame [143]. We suppose for simplicity that the molecule has polarizability $\alpha_\parallel$ along the main axis and $\alpha_\perp$ along another axis (see Fig. 4.1). The main axis is located at the angle θ with respect to the laser polarization vector. The induced dipole along each axis of the molecule is $\alpha_i E_i$ and the total potential energy is

$$\begin{aligned} U = -\int_0^E \boldsymbol{p}\cdot \mathrm{d}\boldsymbol{E}' &= -\frac{1}{2}\alpha_\parallel E_0^2\cos^2\theta - \frac{1}{2}\alpha_\perp E_0^2 \sin^2\theta \\ &= -\frac{1}{2}\alpha_\perp E_0^2 - \frac{1}{2}\Delta\alpha E_0^2\cos^2\theta \end{aligned} \tag{4.4}$$

where $\Delta\alpha = \alpha_\parallel - \alpha_\perp$. Eq. (4.4) shows the difference in polarizability yields an alignment dependent potential energy for the molecule. The torque on the molecule is then

$$\tau = -\frac{\mathrm{d}U}{\mathrm{d}\theta} = -\frac{1}{2}\Delta\alpha E_0^2 \sin 2\theta. \tag{4.5}$$

This shows that molecules aligned at the angle θ with respect to the laser polarization vector receive a torque toward the polarization axis. The torque is negative (positive) for those molecules aligned at positive (negative) angles and it's magnitude depends on the value of θ. The maximum torque is at $\pi/4$ and molecules aligned at $\theta = \{0, \pi/2\}$ receive no torque.

If the laser pulse is applied for a long time the molecules will slowly migrate toward the polarization axis and oscillate around $\theta = 0$ with some thermal distribution. This is called adiabatic alignment. If the pulse is applied for a time less than the prompt alignment time scale (typically hundreds of femtoseconds) then the short torque applied by the laser field causes the molecules to rotate toward the polarization axis. This is non-adiabatic alignment. Long after the short pulse has passed the main polarizability axis will re-phase with the polarization axis. This occurs at integer multiples of the revival time T_R.

4.1.2 Experiment

To measure the molecular alignment in the lab frame we use Coulomb explosion [85]. In this approach a short, non-ionizing pump pulse creates a rotational wavepacket. A high intensity, circularly polarized probe pulse removes the bonding electrons from the molecule causing it to dissociate by Coulomb repulsion. We detect the dissociating fragments using VMI. The momentum vector of the fragments tells us how the molecule was positioned in the lab frame prior to explosion. The time delay between pump and probe pulses is precisely adjusted by a computer controlled delay stage.

To make a full characterization of the alignment distribution we must measure the fragment momenta in three dimensions. This is possible using delay-line anode detectors [92], however, as discussed in Chapter 2 the VMI spectrometer records a momentum distribution in only two dimensions. The full 3-D distribution can be retrieved using the tomographic procedure in section 2.6.2 or an inverse Abel transform. In molecular alignment experiments, however, the symmetry condition for Abel inversion is only satisfied at certain times during the wavepacket revival and hence cannot be used to measure alignment. The tomographic reconstruction requires a lot of data and is not feasible for day-to-day operation.

As a work-around, we attribute a single average momentum to the distribution. This is possible when the kinetic energy release (KER) has a well defined value. The KER represents the asymptotic kinetic energy given to

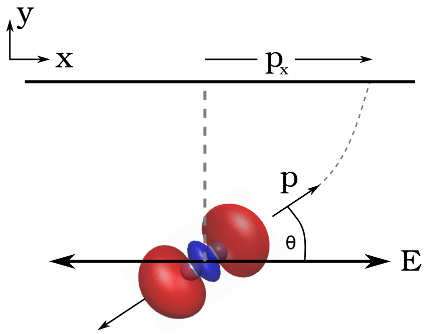

Figure 4.2: Coulomb explosion imaging of molecular alignment in VMI. The pump polarization is along the x axis and is parallel to the detector face. The molecule lies at an angle θ with respect to the pump polarization axis. Measuring the fragment momentum distribution gives access to the alignment parameter $\cos^2\theta = p_x^2/|\boldsymbol{p}|^2$.

fragments dissociating from a single molecule. For small molecules the fragments often dissociate with a well defined KER, hence attributing a single value to the distribution gives a good approximation to the 3-D alignment. For larger molecules many different dissociation channels can be simultaneously populated and the approach will need modification. To determine the KER and the corresponding momentum, we measure a momentum spectrum with the pump pulse blocked. The approach of using a single average momentum likely underestimates the degree of alignment created by the pump pulse.

We measure the 2-D momentum spectrum of the fragments in the lab frame as a function of pump-probe delay (see Fig. 4.2). Typically we observe doubly charged atomic ions. At each delay the 2-D momentum distribution is recorded, $\frac{\mathrm{d}^2N}{\mathrm{d}p_x\mathrm{d}p_z}$. We then project the momentum distribution into the plane of polarization to remove the bias introduced by exploding those molecules that lie in the polarization plane [85]. The alignment parameter is then

$$\begin{aligned}\langle\cos^2\theta\rangle &= \int_0^\pi \mathrm{d}\theta\cos^2\theta\left(\int\frac{\mathrm{d}^2N}{\mathrm{d}p_x\mathrm{d}p_z}\mathrm{d}p_z\right)\\ &= \int_{-p}^{p}\frac{\mathrm{d}p_x}{\sqrt{p^2-p_x^2}}\frac{p_x^2}{p^2}\left(\int\mathrm{d}p_z\frac{\mathrm{d}^2N}{\mathrm{d}p_x\mathrm{d}p_z}\right).\end{aligned} \tag{4.6}$$

By recording the time dependent fragment momentum distributions we can

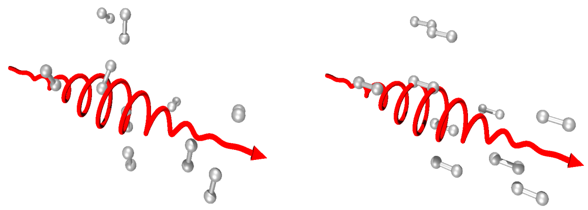

(a) aplanement (b) k-alignment

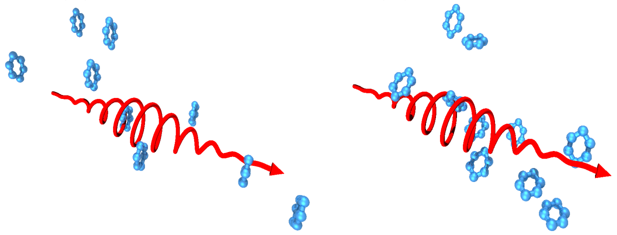

(c) aplanement (d) anti-aplanement

Figure 4.3: Alignment in circularly polarized light. The propagation direction (k-axis) is indicated by the arrow head. (a) A linear molecule is aligned in the plane of polarization. (b) Anti-alignment of a linear molecule fixes the molecular axis along the laser k-axis. (c) Aplanement of benzene. The normal vector to the molecular plane is aligned along the k-axis. (d) Anti-aplanement of benzene. The normal vector now lies in the plane of polarization.

follow the evolution of the rotational wavepacket excited by the pump pulse. This was shown in Fig. 2.7.

The same technique can be used to measure alignment using a circularly polarized pump pulse. In this situation the initial torque pulls the main polarizability axis into the plane of polarization (shown in Fig. 4.3). We call this *aplanement*. For a planar molecule like benzene the molecular plane lies in the plane of polarization and the normal vector is aligned with the laser propagation vector (i.e. k-axis). The anti-alignment with a circularly polarized pump pulse fixes the main polarizability axis orthogonal to the plane of polarization. In the case of a linear molecule, this means the molecular axis lies along the k-axis. Therefore, we call this molecular distribution *k-alignment*. For a planar molecule the normal vector is in the plane of polarization at anti-alignment. Using a circularly polarized pump and probe, Coulomb explosion is again used to measure alignment, but now replacing the laser polarization vector with the k-axis. This means the fragment momentum distribution is projected onto the p_z axis. The alignment angle is then measured with respect to p_z. For measuring k-alignment we therefore use

$$\begin{aligned} \langle\cos^2\theta\rangle &= \int_0^\pi \mathrm{d}\theta\cos^2\theta\left(\int\frac{\mathrm{d}^2N}{\mathrm{d}p_x\mathrm{d}p_z}\mathrm{d}p_x\right) \\ &= \int_{-p}^{p}\frac{\mathrm{d}p_z}{\sqrt{p^2-p_z^2}}\frac{p_z^2}{p^2}\left(\int\mathrm{d}p_x\frac{\mathrm{d}^2N}{\mathrm{d}p_x\mathrm{d}p_z}\right). \end{aligned} \tag{4.7}$$

Enhanced ionization of small molecules by strong laser fields means that it is much easier to observe molecules lying at small angles to the plane of polarization [144]. This introduces a bias to our measurement using Coulomb explosion – our view of the k-algined molecules is always occluded. It is therefore difficult to make quantitative measurements of the degree of alignment for k-aligned molecules. Nonetheless, the qualitative revival structure in a rotational wavepacket can still be observed. In Fig. 4.4a we show a revival scan for O_2 using a circularly polarized pump pulse. The full revival of O_2 occurs at $T_R = 11.7$ ps. The alignment created by a circularly polarized pump pulse shows the same 1/4, 1/2, 3/4 and full revivals as using a linearly polarized pump (compare to Fig. 2.7). The timing of each revival is indicated by the arrows in Fig. 4.4a. Figs. 4.4c and d show examples of measured O^{2+} fragment spectra recorded at aplanement and k-alignment respectively. Because of the bias, the differences are subtle, however, one can see that the distribution at k-alignment is broader along the laser propagation (z) axis. The difference between the two alignment distributions is more clear in Fig. 4.4e which shows the spectra integrated and projected onto the z axis. Despite the biased introduced by Coulomb explosion, it is clear that the k-aligned distribution contains substantially more molecules aligned along the z axis.

The bias to preferentially explode those molecules in the plane of polarization means it is very difficult to make a quantitative measurement of the degree of k-alignment. This is the reason for reduced contrast and systematic offset of the alignment in Fig. 4.4. Additionally, because of the definition of the alignment angle with respect to the z axis rather than the polarization axis, the revival structure appears inverted. For example, at the full revival (11.7 ps for O_2) the rotational wavepacket first goes through k-alignment ($\langle\cos^2\theta\rangle$ large) followed by aplanement ($\langle\cos^2\theta\rangle$ smaller).

The same technique was used to measure the alignment of benzene (shown in Fig. 4.4b). For benzene we observe only the half revival at 44.1 ps and

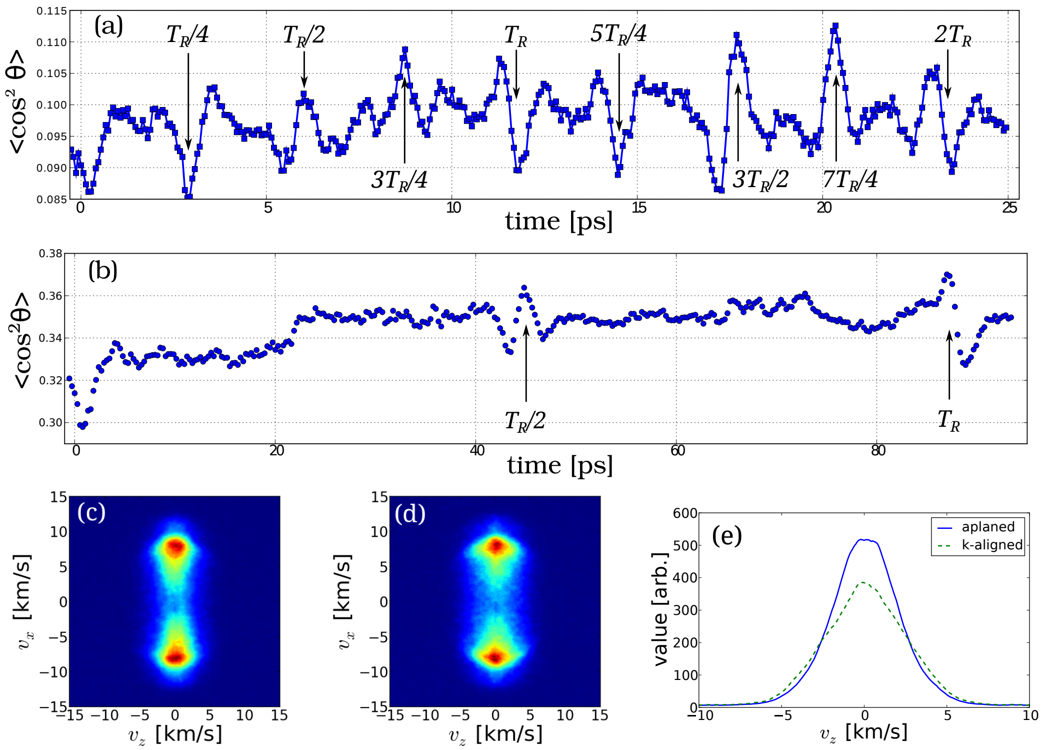

Figure 4.4: Rotational wavepacket dynamics of (a) O_2 ($T_R = 11.7$ ps) and (b) C_6H_6 ($T_R = 88.2$ ps) using a circularly polarized pump pulse. The alignment angle θ is measured with respect to the laser k-axis (z). For O_2 (a) the same revivals as Fig. 2.7 are present with a circularly polarized pump.
(c) O^{2+} fragment momentum distribution at aplanement ($T_R/4 = 2.90$ ps).
(d) O^{2+} fragment momentum distribution at k-alignment ($3T_R/4 = 8.68$ ps).
(e) Integrated distribution along the propagation axis of the O^{2+} fragments at aplanement and k-alignment.

the full revival at 88.2 ps.

4.2 Strong Field Ionization

When a molecule is exposed to an intense infrared laser pulse, it can ionize through a tunnelling process. For small molecules this most often means removing an electron from the highest occupied molecular orbital (HOMO). We assume the nuclei are fixed at their equilibrium positions $\boldsymbol{R}$ and the orbital wavefunction adiabatically follows the laser field. The ionization rate [77] and photo-electron distribution [79] depend on the angle between the molecular axis and laser polarization.

We employ circularly polarized light to examine tunnel ionization from N_2, O_2 and benzene. By comparing molecular frame photo-electron angular distributions (MF-PADs) recorded under different alignment conditions, we show how single ionization from this set of molecules can be described as tunneling from the Dyson orbital[1]. Since the parity of the Dyson orbitals is different (i.e. σ_g from N_2 vs. π_g in O_2 and benzene) we can observe evidence of nodal planes by comparing the MF-PADs from different molecules.

4.2.1 Theory

Several theories of molecular strong field ionization exist to account for suppressed ionization [62, 145], angle-dependent ionization [146] and Stark shifts [147]. All use a similar method of dividing the molecular ionization rate into two parts: the first an atomic-like ionization rate depending on E and I_p, and the second a geometrical part depending on the orientation of the molecular orbital. Non-adiabatic effects are not included thus far.

To calculate the alignment dependent tunneling rate, we use a modified version of a molecular tunneling theory [146]. We write the instantaneous ionization rate as

$$\begin{aligned} W\left(E(t)\right) = W_{ADK}\left(E(t)\right) \cdot 100 \\ \times \int \mathrm{d}p_\perp \mathrm{d}p_\parallel \left|\Phi(\boldsymbol{p})\right|^2 \exp\left(-p_\perp^2 \frac{\sqrt{2I_p}}{E(t)}\right) \end{aligned} \tag{4.8}$$

where $W_{ADK}(E)$ is the atomic tunnel ionization rate (1.25) and the second factor includes the effect of the bound momentum orbital, Φ. To calculate Φ, we take an *ab-initio* Dyson orbital and Fourier transform it to make a 3D momentum-space orbital. The momentum space orbital is rotated into the desired orientation in the lab frame. For the anti-aplanement of linear molecules, the molecular axis lies along p_z. To calculate an aplaned distribution we integrate over 30 angles in the plane of polarization (xy).

---

[1] The Dyson orbital represents the ground state of the neutral projected onto the ground state of the cation [137]. Because the potentials are not identical in the neutral and cation, the Dyson orbital is in general not equivalent to the HOMO, although for small molecules they are very similar.

The laser field is given by Eq. (1.1). At each phase of the laser field $0 \leq \omega t < 2\pi$ the momentum distribution is further rotated with respect to the polarization of the ionizing field. This makes two assumptions: (1) $\Phi(\boldsymbol{p})$ is fixed with respect to the molecular frame, (2) the electron wavefunction adiabatically adjusts to the rotating laser field. To calculate the tunneled distribution at a given phase, we use Eq. (1.32) to calculate the lateral momentum distribution. The lateral distribution is then mapped onto a torus using the classical drift momentum (1.11). Integrating over each phase of the circularly polarized pulse creates a 3D distribution for a particular alignment of the molecule in the lab frame.

To study the effect of saturation in the resulting photo-electron distributions, we track the remaining population in the Dyson orbital. The ionization probability from the Dyson orbital is given by (1.28) and the instantaneous ionization yield is $\mathrm{d}p/\mathrm{d}t$. We use the instantaneous yield to weight the contribution from a particular alignment angle as a function of time in the 40 fs pulse. At each time step we average the yield over all alignments present in the molecular distribution to calculate the net yield. From Eq. (4.8) it is clear the yield depends on the alignment of the bound orbital with respect to the polarization axis, in addition to the length of the tunnel barrier $\approx I_p/E$. Implicit in (1.28) is that the yield also depends on the remaining population in the Dyson orbital.

4.2.2 Results

Experimentally, we use circularly polarized 45 fs pulses at 800 nm to probe the aligned molecules. The pulses are split into a pump and probe using a beam-splitter with variable attenuation control in each arm. The circularly polarized pump pulse was stretched to ~ 60 fs for the small molecules (N_2 and O_2) or 250 fs for benzene. The pump laser pulse is focused by an $f/25$ parabolic mirror onto the pulsed gas jet described in section 2.4. By exploding the molecules and measuring the momentum distributions from N^{2+} and O^{2+} fragments, we measured the degree of alignment $\langle\cos^2\theta\rangle = 0.7$ for N_2 and O_2. For benzene we used the proton momentum distribution to observe aplanement and anti-aplanement.

The proton distribution from benzene is considerably more isotropic than the N^{2+} or O^{2+} fragment distributions which are strongly biased by enhanced ionization (recall Fig. 2.5). In Fig. 4.5 we show an example proton distribution in circularly polarized light. There is some ageing of the MCP which

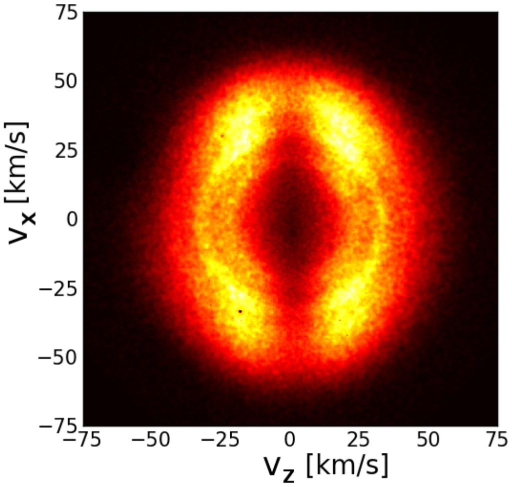

Figure 4.5: Proton momentum distribution from Coulomb explosion of benzene with a circularly polarized 45 fs pulse at 800 nm, 7×10^{14} W/cm^2. The proton distribution is isotropic – little dependence on the exploding laser polarization is observed. Reduced signal at the centre of the detector is due to MCP ageing.

reduces the signal near the centre of the detector. This was not calibrated for in Fig. 4.5. Nonetheless it is clear that the protons fly almost uniformly in all directions when benzene is exploded with a 45 fs pulse. This is despite the fact that enhanced ionization occurs for benzene using pulse durations $\tau \geq 45$ fs [148]. The isotropy of the proton momentum distribution is suggestive of sequential removal or fragments during Coulomb explosion [149] or charge transfer dynamics in benzene ions prior to explosion [150, 151, 152]. Despite the isotropy of the proton distribution, in Fig. 4.4b we still observe wavepacket revivals in alignment of benzene.

We use a circularly polarized probe pulse to singly ionize the aligned or aplaned molecules. The probe was focused onto the sample of aligned molecules with the same parabolic mirror at $f/12.5$. The timing of the probe was precisely controlled by an automated delay stage. In N_2 we used the half revival (aplanement: 4.07 ps, k-alignment: 4.40 ps), for O_2 we used the quarter revival for aplanement (2.90 ps) and three-quarter revival for k-alignment (8.68 ps), and for benzene we used the full revival for anti-aplanement (87.2 ps) and aplanement (88.8 ps). The photo-electron spectra were recorded by the VMI spectrometer. Each measured spectrum is a two-

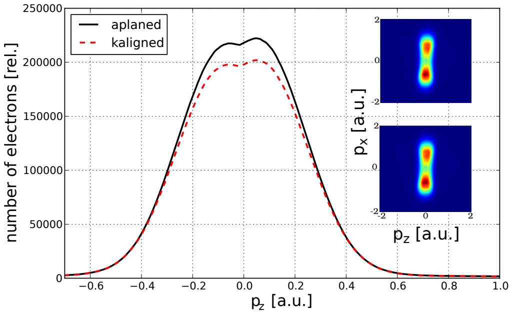

Figure 4.6: Raw lateral momentum distributions for aplaned and k-aligned O_2 integrated over p_x and p_y. k-aligned O_2 shows ionization suppression by about 7%. Inset: 2D photo-electron distributions for aplaned (upper) and k-aligned (lower) O_2.

dimensional projection of the 3-D MF-PAD and contains $\sim 2 \times 10^7$ detected electrons.

An example of the measured raw photo-electron momentum distributions from O_2 at aplanement and k-alignment are shown in Fig. 4.6. The raw distributions are largely a reflection of the strong limits on the electron momentum as we studied from rare gases in section 3.1. In the plane of polarization (xy) the photo-electron drift momentum is given by (1.11). Along the z axis the exponential fall off in ionization probability is due to the increasing tunnel barrier in the lateral direction [69]. Eq. (1.32) gives the prediction of the lateral photo-electron distribution from tunnelling theory.

The lack of obvious structure for the different alignment conditions in Fig. 4.6 is a reflection of imperfect alignment. Despite this, there is 7% less signal from the k-aligned compared to aplaned molecules. This is suppressed ionization from tunneling along the nodal plane of the O_2 Dyson orbital in the k-aligned case [62]. From N_2 and benzene we also observed suppressed ionization from the k-aligned or aplaned molecules respectively, however, the raw photo-electron spectra did not show clear structural features. The suppression was 7% for N_2 and 5% for benzene.

The raw width of the lateral distribution from the three molecules is largely consistent with the values measured in atoms [69]. Additionally, we are able to compare the relative width of the lateral distribution for k-aligned vs. aplaned molecules. In O_2 the k-aligned distribution is 2.3% wider ($1/e$ half width) than the aplaned distribution, however, in benzene the aplaned

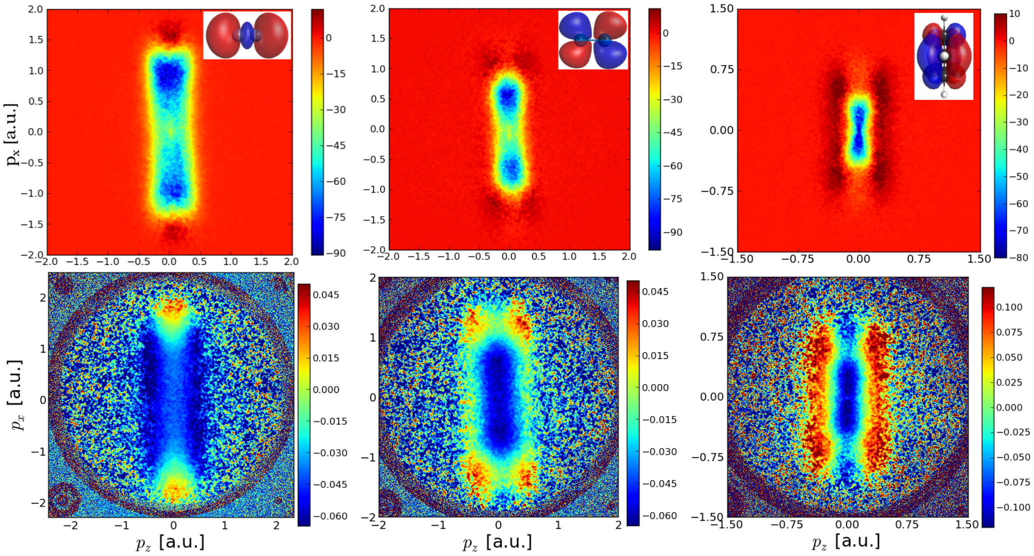

N_2 O_2 C_6H_6

Figure 4.7: Experimental raw difference (upper row) and normalized difference spectra (lower row). Normalized difference is $(a-b)/(a+b)$ where a and b are photo-electron spectra measured under different alignment conditions (see text for details). **Left:** N_2 at 4.5×10^{14} W/cm^2. **Centre:** O_2 at 2.7×10^{14} W/cm^2. **Right:** Benzene at 4.0×10^{13} W/cm^2.

distribution is 12.3% wider. In N_2 the aplaned spectrum was 1.3% wider than the k-aligned spectrum.

To observe more clearly the features of the bound orbital in the tunneled photo-electron distributions, we process the measured 2D spectra in the following way: (1) making a raw difference $RD = a - b$ where a and b are the k-aligned (anti-aplaned) and aplaned distributions respectively; (2) making a normalized difference, $ND = (a-b)/(a+b)$. By subtracting and dividing two distributions we can partially remove the effect of the large contribution from the tunnel barrier itself and observe the small modulations due to different orientations of the bound state wave-function Φ in Eq. (1.32).

In Fig. 4.7 we show examples of the raw difference spectra and normalized difference spectra for N_2, O_2 and benzene. The spectra each show evidence of the symmetry of the Dyson orbital. The Dyson orbital of N_2 does not contain a nodal plane, however, ionization perpendicular to the molecular axis (from k-aligned molecules) has a lower rate than parallel to the molecular axis (aplaned molecules) [107]. As we will show, this creates the bright red regions at larger longitudinal momentum ($p_x \approx 1.8$). As one looks at larger lateral momenta ($|p_z| > 0.8$) the ionization probability drops by 10^{-4} and the signal is lost to experimental noise.

In the O_2 spectra, the k-aligned molecules have a nodal plane along the polarization axis. Ionization along $p_z \approx 0$ is therefore suppressed compared to molecules aligned in the plane of polarization. As we will show later, this also means the k-aligned molecules will saturate later in the laser pulse when the laser field strength is larger. These two combined effects produce the four bright corners on the edges of the O_2 spectra (Fig. 4.7 left). In benzene there is a nodal plane in the Dyson orbital along the molecular plane. The difference between the aplaned and anti-aplaned molecules creates the regions of positive signal at large lateral momentum ($|p_z| > 0.3$) shown in red in Fig. 4.7 (right column).

To demonstrate that our observations are consistent with the tunneling model, we compare the measured differences to calculations from section 4.2.1. In each case, the orbitals were rotated to create either a k-aligned (anti-aplaned) or aplaned set of molecular alignments. We used the experimental intensity values to calculate the tunneled electron distributions and scaled the number of electrons in each calculated spectrum according to the experimental ionization yields. One percent Gaussian noise was numerically added to each of the calculated spectra to more accurately replicate the measurements. To compare with Fig. 4.7 we then created the raw difference and normalized difference of the k-aligned (anti-aplaned) vs. aplaned spectra. The result is shown in Fig. 4.8.

The upper row of Fig. 4.8 shows the role of saturation in the calculation. For N_2 (upper left) and O_2 (upper centre) the ionization rate from k-aligned molecules is lower than for the aplaned molecules. This means that more population remains in the ground state of the k-aligned molecules later on in the pulse when the laser field is larger. Consequently the photo-electron distribution is shifted to slightly larger drift momentum. This is the reason for the four bright red features on the corners of the raw O_2 distributions (centre column in Fig. 4.8 and 4.7). Saturation also plays a role in creating the bright red regions at large longitudinal momentum ($|p_x| \approx 1.8$) in the N_2 distributions. This is again a consequence of the k-aligned molecules ionizing later in the pulse when the laser field is larger. For benzene, the nodal plane along the molecular axis means that the aplaned molecules have a lower ionization rate and hence saturate later in the pulse as verified in Fig. 4.8 upper

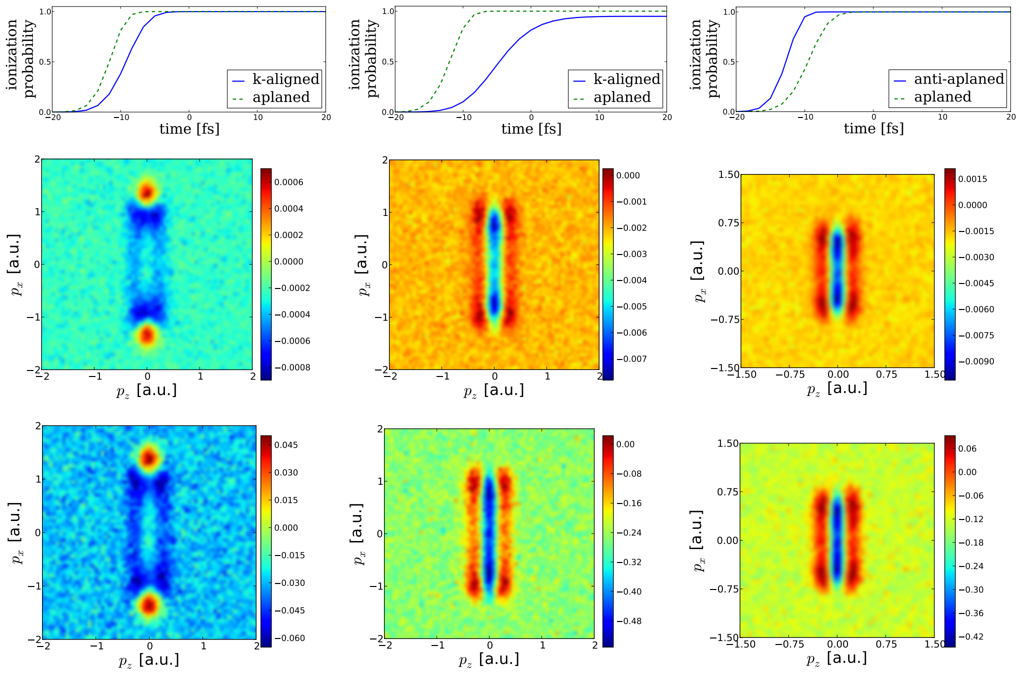

N_2 O_2 C_6H_6

Figure 4.8: **Upper row:** Ionization probability as a function of time in a circularly polarized 40 fs pulse for k-aligned (anti-aplaned) and aplaned molecules. **Middle row:** Calculated raw difference spectra, k-aligned - aplaned distributions. **Lower row:** Calculated normalized difference spectra. **Left:** N_2 at 4.5×10^{14} W/cm^2. **Centre:** O_2 at 2.7×10^{14} W/cm^2. **Right:** Benzene at 4.0×10^{13} W/cm^2. 1% Gaussian noise was added to each calculated spectrum prior to processing.

right. The combination of the large electron density in the lateral direction and shorter tunnel barrier around the maximum of the pulse envelope produces the bright red vertical stripes along the sides of the benzene difference spectra.

Figs. 4.7 and 4.8 illustrate how tunnelling can reveal the symmetry of the ionizing orbital. In O_2 and benzene the Dyson orbital is π. For these molecules, we observe that bright positive regions in the differences and normalized differences appear at larger longitudinal momentum, and for nonzero lateral momentum ($|p_z| > 0.3$). This is due to the nodal plane in the Dyson orbital which suppresses ionization along the polarization axis

($p_z = 0$). In N_2 the Dyson orbital is σ. We observe the ionization is enhanced along the polarization axis ($p_z \approx 0$) at large longitudinal momentum for k-aligned molecules. In the bonding orbital of N_2 there is significant electron density along the polarization axis, so the maximum tunneling amplitude is found at $p_z = 0$.

Summary

By subtracting photo-electron spectra under different molecular alignment conditions, we have shown how laser tunneling can be used to study the symmetry of the Dyson orbital in small molecules. The angular distribution of the bound orbital affects the MF-PAD, ionization rate and saturation intensity in a femtosecond pulse. We have shown how the interplay of these three factors determines the measured photo-electron spectra.

Our measurements used circularly polarized light to isolate the photo-electron from the parent ion. Hence they are free from distortions due to Coulomb focusing or interference with the bound electron wavepacket. This is the most direct approach to observing electron densities in the valence shell and bonding orbitals of molecules.

Technical improvements in molecular cooling, alignment and orientation will lead to improvements in the resolution of the tunneling spectra, much like vibrational isolation is a prerequisite for high resolution STM [48, 49, 50]. This will enable direct imaging of molecular orbital densities using laser tunnelling [79, 153]. Further theoretical development can build on our model by incorporating angle dependent Stark shifts in the neutral and cation [63, 79]. In the future, it would be interesting to apply the ultrahigh spatio-temporal resolution of tunneling to a dynamical problem like charge transfer in molecules [154, 155, 156].

Chapter 5

Conclusion

In this work we have explored the behaviour of atoms and molecules in strong laser fields. By controlling the laser intensity, wavelength, and polarization we have shown how strong field ionization can be modelled as tunnelling of a valence electron through the Coulomb barrier. Tunnelling models work remarkably well in many cases, even though most of our work is in an intermediate regime where the Keldysh parameter $\gamma \approx 1$.

Although the appearance of tunnelling-like behaviour around $\gamma \approx 1$ is unexpected, it is not prohibited. There are still many photons absorbed when $\gamma \approx 1$. In our experiments on ionization of Ar and Ne at 800 nm, ionization requires simultaneous absorption of 18 or more photons. We therefore expect the process is still highly non-perturbative even though $\gamma \approx 1$. At 400 nm ionization of Ar requires absorption of 6-7 photons. This is clearly a different regime. Moreover, as we discuss in section 1.3.1 for the scattering of a particle on an oscillating barrier, perturbative features can occur within a tunnelling problem. The two processes are not mutually exclusive.

There are however, cases where tunnelling is not sufficient. We observed two examples: the lateral momentum distribution of the tunnelled electron, and it's momentum along the laser propagation axis. In the former case, tunnelling theory predicts a value for the electron wavepacket that, although close, is not consistent with our measurements. More complete theories like quantitative tunnelling [73] agree better. In the latter case, the tunnelling model must be supplemented by the Lorentz force to explain the photoelectron's momentum along the propagation axis. The optical magnetic field is essential for providing forward momentum. It is the wave-optics analogue of the photon momentum. This explanation lies beyond the scope of tunnelling models.

In addition to discovering the photon linear momentum partitioning, we also showed how angular momentum is shared in multi-photon ionization. These results, along with the well known rule for energy conservation (1.33) provide all the initial conditions for plasmas generated by multi-photon ionization in a gas. The plasma properties are important for developing new technologies like terahertz sources [125] or novel musical instruments [157].

Better control of the molecular frame is essential for applying the full power of laser tunnelling to molecular imaging. This is analogous to vibrational damping and isolation in scanning tunnelling microscopy [48, 49]. State of the art techniques in cooling, alignment and orientation allow molecules to be prepared in the ground rotational state, and then slowly aligned in the laboratory frame [135, 139]. By rotating the molecular frame with respect to the lab frame and recording a tunnelling photo-electron spectrum at many different angles it is possible to reconstruct a 3-D molecular-frame photoelectron angular distribution [97]. Precise control over the molecular frame is an enabling technology for this type of imaging. Extending 3-D photoelectron spectroscopy to time-dependent processes can give new insight into ultrafast dynamics in molecules [153, 158].

In our work we have concentrated on the ionized electron and mostly ignored the ion. But there is interesting science there too. Ultrafast removal of an electron from a neutral atom or molecule leaves the system with a non-equilibrium charge distribution which must undergo dynamics [159]. The time scale for the hole wavepacket depends on the energy separation of the levels populated [154, 155, 156]. Using few-cycle, carrier-envelope-phase stabilized lightwaves it is possible to trigger ion wavepackets in less than an optical cycle [160]. Watching the coherent hole dynamics, measuring its decoherence and coupling to nuclear degrees of freedom will be a major direction for ultrafast electronics in the future.

Appendix A

Contributions & Acknowledgements

A.1 Statement of Contributions

The attosecond lab at University of Ottawa/NRC is big and many people contribute to research and development. I was instructed to summarize my contributions for the thesis examination committee. My publication list at the time of writing is available below.

In Chapter 1 I give my perspective on ultrafast physics. As with any introduction, many of the concepts are the work of other people. References are given to the original publications where appropriate.

When I arrived at the attosecond lab the VMI chamber described in Chapter 2 was assembled but had never been put to use. I performed the testing, commissioning and calibration of the chamber. I developed the TOF measurement technique we now regularly use for ion experiments and performed the first molecular alignment measurements in our VMI chamber. I was involved in installation of the pulsed gas jet. I automated the experiments by interfacing with peripheral shutters and motion control devices. I did the simulations and created the figures in Chapter 2. I came up with the idea for tomographic imaging of photo-electrons, performed the experiments, analyzed the data and created the figures.

I devised the concept of using circularly polarized light to make a self-consistent test of the tunneled photo-electron wavepacket. In collaboration with a postdoc (Ladan Arissian), we collected the photo-electron data together. I wrote software for analyzing the data, did calculations to support our results and made the figures. I had the idea to check for the contribution of other m-states and did the calculations in section 3.1.1.

During the wavepacket experiment I came up with the idea to include the lateral quantum uncertainty when making the intensity measurement. I did the analysis on the photo-electron data in section 3.2; the ion measurements were done by a postdoc (Christoph Hebeisen) and undergraduate student (Jeff Salvail).

When analyzing the wavepacket experiment I noticed the systematic shift in photo-electron distribution described in section 3.3. I gave the interpretation in terms of the Lorentz force and did the calculations and theory to support it. I made the figures for these results. Ultimately our lab came into collaboration with Laboratoire d'optique apliquée (A Mysyrowicz, B Zhou) who identified the application of this result to terahertz spectroscopy. I also identified the small correction to the angular momentum of the electron-ion system in section 3.4. The basic idea comes from my adviser [133] and my addition completes the description of a conserved quantity.

The concept of laser tunneling as a microscope for molecules has a history of development in the uOttawa/NRC attosecond lab [77, 107, 78, 63]. More recently other ultrafast labs have picked it up too. In collaboration with a postdoc (Ladan Arissian) and visiting professor (A Sokolov) we collected the data in Chapter 4. I wrote the software to analyze the results and made the figures. I also did extensive calculations of the photo-electron spectra from aligned molecules using *ab-initio* orbitals from a collaborator (Michael Spanner).

A.2 Publication List

1. B Zhou, A Houard, Y Liu, B Prade, A Mysyrowicz, A Couairon, P Mora, C Smeenk, L Arissian, and P B Corkum. Measurement and Control of Plasma Oscillations in Femtosecond Filaments *Phys. Rev. Lett.*, 106:255002, 2011.

2. C T L Smeenk, L Arissian, B Zhou, A Mysyrowicz, D M Villeneuve, A Staudte, and P B Corkum. Partitioning of the Linear Photon Momentum in Multiphoton Ionization *Phys. Rev. Lett.*, 106:193002, 2011.

3. C Smeenk, J Z Salvail, L Arissian, P B Corkum, C T Hebeisen, and

A Staudte. Precise in-situ measurement of laser pulse intensity using strong field ionization *Opt. Exp.*, 19(10):9336, 2011.

4. L Arissian, C Smeenk, F Turner, C Trallero, A V Sokolov, D M Villeneuve, A Staudte, and P B Corkum. Direct Test of Laser Tunneling with Electron Momentum Imaging *Phys. Rev. Lett.*, 105(13):133002, 2010.

5. C Smeenk, L Arissian, A Staudte, D M Villeneuve, and P B Corkum. Momentum space tomographic imaging of photoelectrons *J. Phys. B*, 42:185402, 2009.

6. C Smeenk, S Gaede, and J J Battista. Delineation of moving targets with slow MVCT scans: implications for adaptive non-gated lung tomotherapy *Phys. Med. Biol.*, 52:1119, 2007

A.3 Acknowledgements

As I wrote in the statement of contributions, many people contributed to the work described in this thesis. I would like to acknowledge special contributions from a few people. First, my advisor, Prof. Paul Corkum who provided expert guidance and support at many critical times during my work and studies. I have no doubt his input has stengthened and greatly improved our scientific output and changed my perspective on science.

I also wish to acknowledge an excellent and very fruitful collaboration with Dr. Ladan Arissian. We were able to work very well together and our skills seemed to compliment each other. I learned many things from Ladan during her contract in Ottawa and I hope our collaboration will continue.

Lastly, I wish to acknowledge the great love and support I receive from my mother and father. Without it I would be unable to weather the storms and tempests that occaisionally blow through, and sail on to glimpse the sun.

Appendix B

Molecular Tables

Table of rotational constants

See CRC Handbook of Chemistry and Physics [161]

Molecule	I **[amu·nm^2]**	B_0 **[cm^{-1}]**	**Revival period** T_R **[ps]**	
			$2\pi I/\hbar$	$(2B_0c)^{-1}$
H_2	0.0028	60.853	0.28	0.27
N_2	0.085	1.9896	8.41	8.38
CO	0.089	1.9313	8.88	8.64
O_2	0.12	1.4297	11.87	11.67
CO_2	0.46	0.3902	45.49	42.74
CS_2	1.54		152	
C_6H_6	0.89		88.2	
Br_2	2.077	0.0821	206.3	203.14

Table of ionization energies [eV]

See K Kimura *et al.* Handbook of HeI Photoelectron Spectra of Fundamental Organic Molecules [162]

Molecule	I	II	III	IV	V
H_2	15.43				
N_2	15.58	16.98	18.78		
CO	14.01	16.91	16.91	19.72	
O_2	12.07	16.62	17.5	18.17	20.43
CO_2	13.78	17.59	18.08	19.4	
CS_2	10.07	12.83	14.47	16.19	
C_6H_6	9.25	11.53	12.38	13.98	14.86
Br_2	10.55	10.91	13.09	14.62	
OCS	11.18				
H_2O	12.62	14.74	18.51		

Appendix C

Momentum space orbitals

The position and momentum representations in quantum mechanics are related by a Fourier transform [115]

$$\Phi(\boldsymbol{p}) = (2\pi)^{-3/2} \int \mathrm{d}^3\boldsymbol{r} e^{-i\boldsymbol{p}\cdot\boldsymbol{r}} \psi(\boldsymbol{r}) \tag{C.1}$$

where the variables are in atomic units. For hydrogen-like atoms the momentum space orbitals are given by [115, 114]

$$\Phi(\boldsymbol{p}) = F_{nl}\left(p\right) Y_{lm}\left(\theta, \phi\right) \tag{C.2}$$

where (p, θ, ϕ) is the momentum in spherical coordinates and Y_{lm} are the spherical harmonic functions which are unchanged by the Fourier transform. The function F_{nl} is

$$\begin{aligned} F_{nl}\left(p\right) = \left(\frac{2Z}{\pi}\frac{(n-l-1)!}{(n+l)!}\right)^{1/2} 2^{2l+2} Z^{3l+2} n^{l+2} l! \\ \cdot \frac{p^l}{\left(n^2p^2+Z^2\right)^{l+2}} C^{l+1}_{n-l-1}\left(\frac{n^2p^2-Z^2}{n^2p^2+Z^2}\right) \end{aligned} \tag{C.3}$$

where $C^b_a(x)$ is the Gegenbauer function and Z is the effective nuclear charge seen by the electron [116]. The $C^b_a(x)$ are a set of orthogonal polynomials. A few values of the function F_{nl} are shown in table C.1.

In many cases analytical formulae for momentum space orbitals are not available. In these situations the orbitals can be constructed from ab initio orbitals calculated in configuration space using quantum chemistry programs.

$$
\begin{aligned}
F_{10} &= \frac{4Z^{5/2}}{\sqrt{\pi/2}}\,\frac{1}{\left(p^2+Z^2\right)^2} \\
F_{21} &= \frac{128Z^{11/2}}{\sqrt{3\pi}}\,\frac{p}{\left(4p^2+Z^2\right)^3} \\
F_{31} &= \frac{288Z^{11/2}}{\sqrt{\pi/3}}\,\frac{p\left(9p^2-Z^2\right)}{\left(9p^2+Z^2\right)^4} \\
F_{41} &= \frac{512Z^{11/2}}{\sqrt{15\pi/2}}\,\frac{p\left[12\left(16p^2-Z^2\right)^2-2\left(16p^2+Z^2\right)^2\right]}{\left(16p^2+Z^2\right)^5} \\
F_{51} &= \frac{200Z^{11/2}}{\sqrt{3\pi/5}}\,\frac{p\left[32\left(25p^2-Z^2\right)^3-12\left(25p^2-Z^2\right)\left(25p^2+Z^2\right)^2\right]}{\left(25p^2+Z^2\right)^6}
\end{aligned}
$$

Table C.1: Some values of F_{nl}

An example algorithm for converting a configuration space orbital to momentum space is shown below. The Python program reads as input a file containing a position space *ab-initio* orbital and coordinates. It calculates as output a momentum space orbital in 3-D, normalized by $\langle\Phi|\Phi\rangle = 1$.

```
# read the ab initio orbital and coordinates
x,y,z,psi_r = read(filename,‘r’)

# zero pad the orbitals
npad = 127
psir_pd, pdCoords = zeropad(psi_r, [x,y,z], npad)
dx = pdCoords[0][1,0,0] - pdCoords[0][0,0,0]
dy = pdCoords[1][0,1,0] - pdCoords[1][0,0,0]
dz = pdCoords[2][0,0,1] - pdCoords[2][0,0,0]

# calculate the momentum space wavefunction
psi_k = py.fftshift( py.fftn( py.ifftshift(psir_pd) ) )
```

```
# calculate momentum values
# 1D frequency values
kx = py.fftshift( 2*py.pi*py.fftfreq(pdCoords[0].shape[0], dx) )

ky = py.fftshift( 2*py.pi*py.fftfreq(pdCoords[0].shape[1], dy) )

kz = py.fftshift( 2*py.pi*py.fftfreq(pdCoords[0].shape[2], dz) )
dp = kx[1] - kx[0]

# normalize
A = py.sum( abs(psi_k)**2) * dp**3
psi_k = psi_k / py.sqrt(A)

def zeropad(M, coordIn, n):

  xi,yi,zi = coordIn
  # scaling factor
  scftr = float(n)/xi.shape[0]
  gsize2 = xi.max()*scftr
  x3,y3,z3 = py.mgrid[-gsize2:gsize2:n*1j, -gsize2:gsize2:n*1j, -gsize2:gsize2

  dx = xi[1,0,0] - xi[0,0,0]
  dy = yi[0,1,0] - yi[0,0,0]
  dz = zi[0,0,1] - zi[0,0,0]

  ivals = (x3 - xi[0,0,0])/dx
  jvals = (y3 - yi[0,0,0])/dy
  kvals = (z3 - zi[0,0,0])/dz
  coords = py.array([ivals, jvals, kvals])

  # zero padded orbitals are now sampled at the points x3, y3, z3
  M_zp = ndimage.map_coordinates(M, coords)

  return M_zp, [x3,y3,z3]
```

Appendix D

The role of the earth's magnetic field

This appendix summarizes how electrons are deflected by the earth's magnetic field in the velocity map imaging chamber. Electrons ionized by the laser field are first accelerated through a series of electrodes. They then enter a field free region and travel at their maximum velocity until colliding with the detector. Since the field free region is much longer than the acceleration region and the velocity is the largest in the field free region, the largest deflection due to the Lorentz force will occur in the field free region. The following analysis ignores any small deflections that occur in the acceleration region.

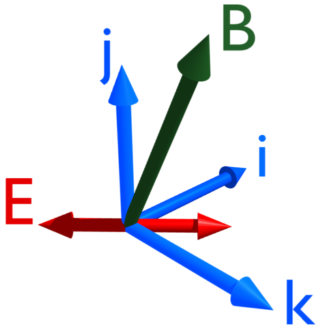

Figure D.1: Coordinate system for the problem. B is the earth's magnetic field and E is the polarization. The spectrometer's electric field (not shown) accelerates the electrons in the ĵ direction.

It is useful to choose a coordinate system with the spectrometer axis along the ĵ direction and the earth's magnetic field lying in the ĵ-k̂ plane. In that case $\vec{B} = (0, B_y, B_z)$. The initial kinetic energy release occurs along the laser polarization, $\vec{E}$, which lies in the î-k̂ plane (refer to figure D.1). We can let the electron be initially at the origin with velocity $\vec{u}_0 = (u_x, u_y, u_z)$.

Using $m\vec{a} = q\vec{v} \times \vec{B}$,

$$\ddot{x} = \omega_z \dot{y} - \omega_y \dot{z} \tag{D.1}$$

$$\ddot{y} = -\omega_z \dot{x} \tag{D.2}$$

$$\ddot{z} = \omega_y \dot{x} \tag{D.3}$$

where we have used $\omega_y \equiv qB_y/m$ and $\omega_z \equiv qB_z/m$. It also simplifies the expressions to define another frequency $\omega_1^2 \equiv \omega_y^2 + \omega_z^2$. To solve the equations of motion, first differentiate (D.1) again and substitute in (D.2) and (D.3). Then using the initial condition on $\vec{u}_0$ and the initial position at the origin, one finds

$$\begin{aligned} x(t) &= \frac{u_x}{\omega_1} \sin \omega_1 t + \frac{u_z}{\omega_y} (\cos \omega_1 t - 1) \\ y(t) &= \frac{\omega_z u_x}{\omega_1^2} (1 - \cos \omega_1 t) + \frac{\omega_z u_z}{\omega_y \omega_1} (\omega_1 t - \sin \omega_1 t) + u_y t \\ z(t) &= \frac{\omega_y u_x}{\omega_1^2} (1 - \cos \omega_1 t) + \frac{u_z}{\omega_1} \sin \omega_1 t \end{aligned} \tag{D.4}$$

Time-of-flight

To find the time of flight, we set $y = L$ where L is the length of the flight tube. Equation (D.4) can be solved by expanding sin and cos as polynomials and retaining up to the quadratic terms. This is valid when $\omega_1 t$ is a small number ($t \ll 100$ ns in this case). This simplification leads to a quadratic equation for time with the solution

$$\begin{aligned} t &= \frac{1}{\omega_z u_x} \left(-u_y \pm \sqrt{u_y^2 + 2\omega_z u_x L} \right) \\ &\approx \frac{1}{\omega_z u_x} \left(-u_y + u_y \left(1 + \frac{\omega_z u_x L}{u_y^2} \right) \right) \\ &= \frac{L}{u_y} \end{aligned} \tag{D.5}$$

where we have used a binomial expansion and the fact that $u_y \gg u_x$. This gives the time-of-flight, $t = L/u_y$ which is the same as the time-of-flight in the absence of a magnetic field. Inserting (D.5) in equations (D.4) we find

$$\begin{aligned} x &= \frac{u_x L}{u_y} - \frac{u_z \omega_1^2 L^2}{2\omega_y u_y^2} \\ z &= \frac{u_z L}{u_y} + \frac{\omega_y u_x L^2}{2u_y^2} \end{aligned} \tag{D.6}$$

The second terms in equations (D.6) represent the deflection of the electron from its typical trajectories in the absence of a magnetic field. For an initial kinetic energy release of 10 eV, an acceleration along ĵto 1 keV, $L = 61$ mm and $\vec{B}_{earth} = (0,\ 52.1,\ 17.8)\ \mu$T, the shift in x and z is less than 0.1 mm. Furthermore, by increasing the potential in the acceleration region, only u_y changes in equations (D.6) and therefore the deflection is further diminished, although at some point relativistic effects become significant.

Appendix E

Gaussian integrals

This section derives properties of some integrals related to the Gaussian integral

$$\int_{-\infty}^{\infty} e^{-x^2} \mathrm{d}x = \sqrt{\pi}. \tag{E.1}$$

A helpful reference for all of these problems is Arfken and Weber [55]. First, consider the related integral:

$$\begin{aligned} \boldsymbol{I_1} &= \int_0^{\infty} e^{-(x-b)^2/a^2} \mathrm{d}x \\ &= a \int_{-b/a}^{0} e^{-u^2} \mathrm{d}u + a \int_0^{\infty} e^{-u^2} \mathrm{d}u. \\ &= \frac{\sqrt{\pi} a}{2} \left(1 + \mathrm{erf}\left(\tfrac{b}{a}\right)\right) \end{aligned} \tag{E.2}$$

where $u = (x - b)/a$. Since the Gaussian is an even function, switching the limits of integration to $0 \leq u \leq b/a$ doesn't change the result. Eqn. (E.2) contains the error function

$$\mathrm{erf}\,(x) = \frac{2}{\sqrt{\pi}} \int_0^x e^{-t^2} \mathrm{d}t. \tag{E.3}$$

One interesting feature of the error function is its integral:

$$\int \mathrm{erf}\,(x/a)\,\mathrm{d}x = x\;\mathrm{erf}\,(x/a) + \frac{a}{\sqrt{\pi}} e^{-x^2/a^2}. \tag{E.4}$$

Next we consider the more general integral,

$$\begin{aligned}\boldsymbol{I_2} &= \int_0^c x^m e^{-x^2/a^2} \mathrm{d}x \\ &= \frac{a^{m+1}}{2} \int_0^{c^2/a^2} w^{(m-1)/2} e^{-w} \mathrm{d}w \\ &= \frac{a^{m+1}}{2} \gamma\left(\tfrac{m+1}{2}, c^2/a^2\right) \end{aligned} \tag{E.5}$$

where the incomplete gamma function is defined by

$$\gamma\left(a, x\right) = \int_0^x t^{a-1} e^{-t} \mathrm{d}t. \tag{E.6}$$

By making the change of variables $t = u^2$, the incomplete gamma function is related to the error function via

$$\sqrt{\pi}\,\mathrm{erf}\left(x\right) = \gamma\left(\tfrac{1}{2}, x^2\right). \tag{E.7}$$

γ also obeys a recursion relation

$$\gamma\left(a+1, x\right) = a\gamma\left(a, x\right) - x^a e^{-x}. \tag{E.8}$$

When a is an integer, the incomplete gamma function simplifies to

$$\gamma\left(n, x\right) = (n-1)!\left(1 - e^{-x} \sum_{s=0}^{n-1} \frac{x^s}{s!}\right). \tag{E.9}$$

The ordinary gamma function is then $\Gamma\left(a\right) = \lim_{x\to\infty} \gamma\left(a, x\right)$ so that in a limiting case of (E.5)

$$\int_0^\infty x^m e^{-x^2/a^2} \mathrm{d}x = \frac{a^{m+1}}{2} \Gamma\left(\tfrac{m+1}{2}\right). \tag{E.10}$$

The last integral to present is the most general one:

$$\boldsymbol{I_3} = \int_0^c x^m e^{-(x-b)^2/a^2} \mathrm{d}x. \tag{E.11}$$

First change the variables $v = x - b$

$$\begin{aligned}\boldsymbol{I_3} &= \int_{-b}^{c-b} \left(v+b\right)^m e^{-v^2/a^2} \mathrm{d}v \\ &= \sum_{j=0}^{m} \binom{m}{j} b^{m-j} \left[\int_{-b}^{0} v^j e^{-v^2/a^2} \mathrm{d}v + \int_0^{c-b} v^j e^{-v^2/a^2} \mathrm{d}v\right]. \end{aligned} \tag{E.12}$$

In (E.12) it is now assumed that m is an integer. The second of these integrals is given by (E.5). The first integral is also given by (E.5) but can change sign depending if v^j is an even or odd function. Using this in (E.12) yields the final result for $\boldsymbol{I_3}$,

$$\int_0^c x^m e^{-(x-b)^2/a^2} \mathrm{d}x = \sum_{j=0}^{m} \binom{m}{j} \frac{b^{m-j} a^{j+1}}{2} \left[(-1)^j \gamma\left(\tfrac{j+1}{2}, b^2/a^2\right) + \gamma\left(\tfrac{j+1}{2}, \tfrac{(c-b)^2}{a^2}\right)\right]. \tag{E.13}$$

Once again, there is a limiting case $c \to \infty$:

$$\int_0^\infty x^m e^{-(x-b)^2/a^2} \mathrm{d}x = \sum_{j=0}^{m} \binom{m}{j} \frac{b^{m-j} a^{j+1}}{2} \left[(-1)^j \gamma\left(\tfrac{j+1}{2}, b^2/a^2\right) + \Gamma\left(\tfrac{j+1}{2}\right)\right]. \tag{E.14}$$

Some cases of Eqn. (E.14) for particular values of m are given in Table E.1.

m	$\boldsymbol{I_3}$
1	$\frac{ab\sqrt{\pi}}{2}\left(1+\operatorname{erf}\left(\frac{b}{a}\right)\right)+\frac{a^2}{2}e^{-b^2/a^2}$
2	$\frac{a^3\sqrt{\pi}}{4}\left(1+\operatorname{erf}\left(\frac{b}{a}\right)\right)\left(1+\frac{2b^2}{a^2}\right)+\frac{a^2b}{2}e^{-b^2/a^2}$

Table E.1: Values of Eqn. (E.14)

Bibliography

[1] P. Krehl and S. Engemann. August Toepler – the first who visualized shock waves. *Shock Waves*, 5:1–18, 1995. 1

[2] D. H. Kelly. Spatio-temporal frequency characteristics of color-vision mechanisms. *J. Opt. Soc. Am.*, 64(7):983–990, Jul 1974. 1

[3] P J Fitzgibbons and F L Wightman. Gap detection in normal and hearing-impaired listeners. *J Acoust. Soc. Am.*, 72:761, 1982. 1

[4] J Dargahi and S Najarian. Human tactile perception as a standard for artificial tactile sensing – a review. *Int. J Med. Robotics Computer Assisted Surgery*, 1(1):23–35, 2004. 1

[5] F Krausz and M Ivanov. *Rev. Mod. Phys.*, 81(1):163, 2009. 1

[6] A H Zewail. Femtochemistry: Atomic-scale dynamics of the chemical bond using ultrafast lasers (Nobel Lecture). *Angew Chem Int Ed*, 39(15):2586, 2000. 2

[7] P. M. Paul, E. S. Toma, P. Breger, G. Mullot, F. Augé, Ph. Balcou, H. G. Muller, and P. Agostini. Observation of a train of attosecond pulses from high harmonic generation. *Science*, 292(5522):1689–1692, 2001. 3, 8

[8] M. Hentschel, R. Kienberger, Ch. Spielmann, G. A. Reider, N. Milosevic, T. Brabec, P. Corkum, U. Heinzmann, M. Drescher, and F. Krausz. Attosecond metrology. *Nature*, 414(6863):509–513, 2001. 3

[9] T Brabec and F Krausz. Nonlinear optical pulse propagation in the single-cycle regime. *Phys. Rev. Lett.*, 78:3282–3285, Apr 1997. 3

[10] J D Jackson. *Classical Electrodynamics*. Wiley, 3 edition, 1999. 3, 4

[11] P B Corkum, N H Burnett, and F Brunel. *Phys. Rev. Lett.*, 62(11):1259, 1989. 4, 7, 68

[12] J H Eberly. Interaction of very intense light with free electrons. In *Progress in Optics*, volume 7, page 360. North-Holland Pub. Co., 1969. 4

[13] E. S. Sarachik and G. T. Schappert. Classical theory of the scattering of intense laser radiation by free electrons. *Phys. Rev. D*, 1:2738–2753, May 1970. 4

[14] C T L Smeenk, L Arissian, B Zhou, A Mysyrowicz, D M Villeneuve, A Staudte, and P B Corkum. Partitioning of the linear photon momentum in multiphoton ionization. *Phys. Rev. Lett.*, 106:193002, 2011. 5, 44

[15] P Eckle, M Smolarski, P Schlup, J Biegert, A Staudte, M Schöffler, H Muller, R Dörner, and U Keller. Attosecond angular streaking. *Nat Phys*, 4:565, 2008. 6

[16] P Eckle, A N Pfeiffer, C Cirelli, A Staudte, R Dörner, H Muller, M Büttiker, and U Keller. *Science*, 322(5907):1525, 2008. 6, 18

[17] A N Pfeiffer, C Cirelli, M Smolarski, R Dörner, and U Keller. *Nature Phys.*, 7:428, 2011. 6

[18] P B Corkum. *Phys. Rev. Lett*, 71(13):1994, 1993. 8, 9, 10, 41, 43

[19] M Lewenstein, P Balcou, M Y Ivanov, A L'Huillier, and P B Corkum. Theory of high-harmonic generation by low-frequency laser fields. *Phys Rev A*, 49:2117, 1994. 8

[20] G. Sansone, E. Benedetti, F. Calegari, C. Vozzi, L. Avaldi, R. Flammini, L. Poletto, P. Villoresi, C. Altucci, R. Velotta, S. Stagira, S. De Silvestri, and M. Nisoli. Isolated single-cycle attosecond pulses. *Science*, 314(5798):443–446, 2006. 8

[21] J. Itatani, J. Levesque, D. Zeidler, Hiromichi Niikura, H. Pepin, J. C. Kieffer, P. B. Corkum, and D. M. Villeneuve. Tomographic imaging of molecular orbitals. *Nature*, 432(7019):867–871, 2004. 8

[22] A Shiner, B E Schmidt, C Trallero, H J Wörner, S Patchkovskii, P B Corkum, J C Kieffer, F Légaré, and D M Villeneuve. Probing collective multi-electron dynamics in xenon with high-harmonic spectroscopy. *Nature Phys.*, 7:464, 2011. 8

[23] M Spanner, O Smirnova, P B Corkum, and M Ivanov. Reading diffraction images in strong field ionization of diatomic molecules. *J Phys B*, 37:L243, 2004. 8

[24] M Okunishi, T Morishita, G Prümper, K Shimada, C D Lin, S Watanabe, and K Ueda. Experimental retrieval of target structure information from laser-induced rescattered photoelectron momentum distributions. *Phys Rev Lett*, 100:143001, 2008. 8

[25] M Okunishi, H Niikura, R R Lucchese, T Morishita, and K Ueda. Extracting electron-ion differential scattering cross sections for partially aligned molecules by laser-induced rescattering photoelectron spectroscopy. *Phys Rev Lett*, 106:063001, 2011. 8

[26] D. N. Fittinghoff, P. R. Bolton, B. Chang, and K. C. Kulander. Observation of nonsequential double ionization of helium with optical tunneling. *Phys. Rev. Lett.*, 69(18):2642, Nov 1992. 8

[27] A Rudenko, V L B de Jesus, T Ergler, K Zrost, B Fueuerstein, C D Schröter, R Moshammer, and J Ullrich. Correlated two-electron momentum spectra for strong-field nonsequential double ionization of He at 800 nm. *Phys Rev Lett*, 99:263003, 2007. 8

[28] A Staudte, C Ruiz, M Schöffler, S Schössler, D Zeidler, Th Weber, M Meckel, D M Villeneuve, P B Corkum, A Becker, and R Dörner. Binary and recoil collisions in strong field double ionization of helium. *Phys. Rev. Lett.*, 99(26):263002, 2007. 8, 53

[29] D Comtois, D Zeidler, H Pepin, J C Kieffer, D M Villeneuve, and P B Corkum. *J. Phys. B*, 38:1923, 2005. 8, 41, 68

[30] A Rudenko, K Zrost, Th Ergler, A B Voitkiv, B Najjari, V L B de Jesus, B Feuerstein, C D Schroter, R Moshammer, and J Ullrich. *J. Phys. B*, 38:L191, 2005. 8, 41

[31] C Blaga, F Catoire, P Colisimo, G Paulus, H Muller, P Agostini, and L DiMauro. *Nature Phys.*, 5:335, 2009. 8, 72

[32] T Nubbemeyer, K Gorling, A Saenz, U Eichmann, and W Sandner. *Phys. Rev. Lett.*, 101(23):233001, 2008. 8, 17, 66

[33] U Eichmann, T Nubbemeyer, H Rottke, and W Sandner. *Nature*, 461(7268):1261, 2009. 8, 66, 68

[34] H Niikura, H Hasbani, F Legare, M Y Ivanov, A D Bandrauk, D M Villeneuve, and P B Corkum. Sub-laser-cycle electron pulses for probing molecular dynamics. *Nature*, 417(6892):917, 2002. 8, 9, 17

[35] Z Chang. *Fundamentals of Attosecond Optics*. CRC Press, 2011. 8, 13, 48, 49

[36] P Salières, A L'Huillier, and M Lewenstein. Coherence control of high-order harmonics. *Phys. Rev. Lett.*, 74:3776–3779, 1995. 9

[37] D D. Hickstein, P Ranitovic, S Witte, X M Tong, Y Huismans, P Arpin, X Zhou, K E Keister, C W Hogle, B Zhang, C Ding, P Johnsson, N Toshima, M J J Vrakking, M M Murnane, and H C Kapteyn. Direct visualization of laser-driven electron multiple scattering and tunneling distance in strong-field ionization. *Phys. Rev. Lett.*, 109:073004, 2012. 9, 12, 21, 73

[38] G Drake, editor. *Springer Handbook of Atomic, Molecular, and Optical Physics*. Springer, 2nd edition, 2006. 10, 12, 21, 22

[39] R McWeeny. Natural units in atomic and molecular physics. *Nature*, 243:196, 1973. 10, 12, 21

[40] E Goulielmakis, Z H Loh, A Wirth, R Santra, N Rohringer, V S Yakovlev, S Zherebtsov, T Pfeifer, A M Azzeer, M F Kling, S R Leone, and F Krausz. Real-time observation of valence electron motion. *Nature*, 466(7307):739, 2010. 10

[41] H J Wörner and P B Corkum. *J. Phys. B*, 44:041001, 2011. 10

[42] O Smirnova, Y Mairesse, S Patchkovskii, N Dudovich, D M Villeneuve, P B Corkum, and M Y Ivanov. *Nature*, 460(7258):972, 2009. 10, 75

[43] Y. Mairesse, J. Higuet, N. Dudovich, D. Shafir, B. Fabre, E. Mével, E. Constant, S. Patchkovskii, Z. Walters, M Ivanov, and O Smirnova. High harmonic spectroscopy of multichannel dynamics in strong-field ionization. *Phys. Rev. Lett.*, 104:213601, 2010. 10

[44] M O Scully and M S Zubairy. *Quantum Optics*. Cambridge University Press, 1997. 11

[45] L V Keldysh. *Sov. Phys. JETP*, 20:1307, 1965. 11

[46] G Gamow. *Z. Physik*, 51:204, 1928. 11

[47] I Giaever. Energy gap in superconductors measured by electron tunneling. *Phys Rev Lett*, 5(4):147, 1960. 11

[48] G Binnig and H Rohrer. Scanning tunneling microscopy. *Helvetica Physica Acta*, 55:726, 1982. 11, 90, 92

[49] C J Chen. *Introduction to Scanning Tunneling Microscopy*. Oxford University Press, 1993. 11, 90, 92

[50] J Repp, G Meyer, S M Stojković, A Gourdon, and C Joachim. Molecules on insulating films: Scanning-tunneling microscopy imaging of individual molecular orbitals. *Phys. Rev. Lett.*, 94:026803, 2005. 11, 90

[51] B. Walker, B. Sheehy, L. F. DiMauro, P. Agostini, K. J. Schafer, and K. C. Kulander. Precision measurement of strong field double ionization of helium. *Phys. Rev. Lett.*, 73(9):1227–1230, Aug 1994. 12

[52] Y. Huismans, A. Rouzée, A. Gijsbertsen, J. H. Jungmann, A. S. Smolkowska, P. S. W. M. Logman, F. Lépine, C. Cauchy, S. Zamith, T. Marchenko, J. M. Bakker, G. Berden, B. Redlich, A. F. G. van der Meer, H. G. Muller, W. Vermin, K. J. Schafer, M. Spanner, M. Yu. Ivanov, O. Smirnova, D. Bauer, S. V. Popruzhenko, and M. J. J. Vrakking. Time-resolved holography with photoelectrons. *Science*, 331(6013):61–64, 2011. 12, 21

[53] D. Rayner, A. Naumov, and P. Corkum. Ultrashort pulse non-linear optical absorption in transparent media. *Opt. Express*, 13(9):3208, May 2005. 12

[54] M V Ammosov, N B Delone, and V P Krainov. *Sov. Phys. JETP*, 64(6):1191, 1986. 13

[55] G B Arfken and H J Weber. *Mathematical Methods for Physicists*. Elsevier Inc., 6th edition, 2005. 13, 104

[56] B H Bransden and C J Joachain. *Quantum Mechanics*. Pearson Prentice Hall, 2nd edition, 2000. 13

[57] M Büttiker and R Landauer. Traversal time for tunneling. *Phys Rev Lett*, 49:1739, 1982. 15

[58] G Yudin and M Y Ivanov. *Phys. Rev. A*, 64:013409, 2001. 16, 42, 45, 49, 71

[59] A M Perelomov, V S Popov, and M V Terentev. *Soviet Physics JETP*, 23(5):924, 1966. 16, 49

[60] T Herath, L Yan, S K Lee, and W Li. Strong-field ionization rate depends on the sign of the magnetic quantum number. *Phys. Rev. Lett.*, 109:043004, 2012. 16

[61] B Walker, B Sheely, L F DiMauro, P Agostini, K J Schafer, and K C Kulander. *Phys. Rev. Lett.*, 73(9):1227, 1994. 16

[62] J Muth-Böhm, A Becker, and F H M Faisal. Suppressed ionization for a class of diatomics in intense femtosecond laser fields. *Phys Rev Lett*, 85:2280, 2000. 16, 19, 76, 83, 86

[63] H Akagi, T Otobe, A Staudte, A Shiner, F Turner, R Dörner, D M Villeneuve, and P B Corkum. *Science*, 325(5946):1364, 2009. 16, 19, 53, 90, 94

[64] M Smits, C. A. de Lange, A Stolow, and D. M. Rayner. Dynamic polarization in the strong-field ionization of small metal clusters. *Phys. Rev. Lett.*, 93:203402, 2004. 16

[65] M Smits, C. A. de Lange, A Stolow, and D. M. Rayner. Absolute ionization rates of multielectron transition metal atoms in strong infrared laser fields. *Phys. Rev. Lett.*, 93:213003, 2004. 16

[66] M Lezius, V Blanchet, D M Rayner, D M Villeneuve, A Stolow, and M Y Ivanov. *Phys. Rev. Lett.*, 86(1):51, 2001. 16, 75

[67] M Lezius, V Blanchet, M Y Ivanov, and A Stolow. *J. Chem. Phys.*, 117(4):1575, 2002. 16, 75

[68] A E Boguslavskiy, J Mikosch, A Gijsbertsen, M Spanner, S Patchkovskii, N Gador, M J J Vrakking, and A Stolow. The multi-electron ionization dynamics underlying attosecond strong-field spectroscopies. *Science*, 335(6074):1336–1340, 2012. 16

[69] L Arissian, C Smeenk, F Turner, C Trallero, A V Sokolov, D M Villeneuve, A Staudte, and P B Corkum. Direct test of laser tunneling with electron momentum imaging. *Phys. Rev. Lett.*, 105(13):133002, 2010. 17, 55, 56, 57, 58, 86

[70] N B Delone and V P Krainov. *JOSA B*, 8(6):1207, 1991. 17

[71] D I Bondar. *Phys. Rev. A*, 78:015405, 2008. 17, 42, 45

[72] J Henkel, M Lein, V Engel, and I Dreissigacker. Adiabaticity in the lateral electron-momentum distribution after strong-field ionization. *Phys. Rev. A*, 85:021402, 2012. 17, 47

[73] I Dreissigacker and M Lein. Quantitative theory for the lateral momentum distribution after strong-field ionization. *Chem Phys*, 2012. 17, 19, 51, 91

[74] C Smeenk, L Arissian, A Staudte, D M Villeneuve, and P B Corkum. Momentum space tomographic imaging of photoelectrons. *J. Phys. B*, 42:185402, 2009. 18, 35, 56, 57, 68

[75] A Czirjak, R Kopold, W Becker, M Kleber, and W P Schleich. *Optics Comm.*, 179(1):29, 2000. 18

[76] A N Pfeiffer, C Cirelli, A S Landsman, M Smolarski, D Dimitrovski, L B Madsen, and U Keller. Probing the logitudinal momentum spread of the electron wave packet at the tunnel exit. *Phys Rev Lett*, 109:083002, 2012. 18, 39

[77] D Pavičić, K F Lee, D M Rayner, P B Corkum, and D M Villeneuve. Direct measurement of the angular dependence of ionization for N_2, O_2, and CO_2 in intense laser fields. *Phys. Rev. Lett.*, 98:243001, 2007. 19, 83, 94

[78] M Meckel, D Comtois, D Zeidler, A Staudte, D Pavicic, H C Bandulet, H Pepin, J C Kieffer, R Dorner, D M Villeneuve, and P B Corkum. *Science*, 320(5882):1478, 2008. 19, 94

[79] L Holmegaard, J Hansen, L Kalhøj, S L Kragh, H Stapelfeldt, F Filsinger, J Küpper, G Meijer, D Dimitrovski, M Abu-samha, C P J Martiny, and L B Madsen. Photoelectron angular distributions from strong-field ionization of oriented molecules. *Nature Phys.*, 6:428, 2010. 19, 34, 83, 90

[80] M Ivanov, M Spanner, and O Smirnova. *J Mod. Opt.*, 52(2 - 3):165, 2005. 19

[81] N B Delone and V P Krainov. *Multiphoton Processes in Atoms.* Springer-Verlag, 2nd edition, 2000. 19, 20

[82] R R Freeman and P H Bucksbaum. *J. Phys. B*, 24:325, 1991. 19

[83] A Eppink and D Parker. Velocity map imaging of ions and electrons using electrostatic lenses. *Rev. Sci. Instruments*, 68(9):3477, 1997. 23, 25, 26

[84] J L Wiza. *Nucl. Inst. Meth.*, 162:587, 1979. 26, 27, 29

[85] P. W. Dooley, I. V. Litvinyuk, Kevin F. Lee, D. M. Rayner, M. Spanner, D. M. Villeneuve, and P. B. Corkum. Direct imaging of rotational wave-packet dynamics of diatomic molecules. *Phys. Rev. A*, 68(2):023406, 2003. 31, 78, 79

[86] M Hillenkamp, S Keinan, and U Even. Condensation limited cooling in supersonic expansions. *J Chem Phys*, 118(19):8699–8705, 2003. 31

[87] D Irimia, R Kortekaas, and M H M Janssen. In situ characterization of a cold and short pulsed molecular beam by femtosecond ion imaging. *Phys. Chem. Chem. Phys.*, 11:3958–3966, 2009. 31

[88] M Nisoli, S De Silvestri, O Svelto, R Szipocs, K Ferencz, Ch Spielmann, S Sartania, and F Krausz. *Opt. Lett.*, 22(8):522, 1997. 32, 42

[89] P O'Shea, M Kimmel, X Gu, and R Trebino. Highly simplified device for ultrashort-pulse measurement. *Opt. Lett.*, 26(12):932, 2001. 32

[90] D Townsend, M P Minitti, and A G Suits. Direct current slice imaging. *Rev. Sci. Inst.*, 74:2530, 2003. 33

[91] L Dinu, A Eppink, Rosca-Pruna F, H L Offerhaus, W J van der Zande, and M Vrakking. Application of a time-resolved event counting technique in velocity map imaging. *Rev. Sci. Inst.*, 73:4206, 2002. 33

[92] J Ullrich, R Moshammer, A Dorn, R Dörner, L P H Schmidt, and H Schmidt-Böcking. Recoil-ion and electron momentum spectroscopy: reaction-microscopes. *Rep. Prog. Phys.*, 66(9):1463, 2003. 33, 53, 78

[93] V Dribinski, A Ossadtchi, V Mandelshtam, and H Reisler. *Rev. Sci. Instr.*, 73(7):2634, 2002. 34, 37

[94] G A Garcia, L Nahon, and I Powis. Two-dimensional charged particle image inversion using a polar basis function expansion. *Rev. Sci. Inst.*, 75:4989, 2004. 34

[95] M Vrakking. An iterative procedure for the inversion of two-dimensional ion/photoelectron imaging experiments. *Rev. Sci. Instr.*, 72(11):4084, 2001. 34

[96] R N Bracewell. *The Fourier Transform and its Applications*. McGraw-Hill, 3rd edition, 2000. 34

[97] J Maurer, D Dimitrovski, L Christensen, L B Madsen, and H Stapelfeldt. Molecular-frame 3d photoelectron momentum distributions by tomographic reconstruction. *Phys. Rev. Lett.*, 109:123001, 2012. 34, 39, 92

[98] M Kitzler and M Lezius. Spatial control of recollision wave packets with attosecond precision. *Phys. Rev. Lett.*, 95:253001, 2005. 34

[99] D Shafir, Y Mairesse, D M Villeneuve, P B Corkum, and N Dudovich. *Nature Phys.*, 5:412, 2009. 34

[100] A C Kak and M Slaney. *Principles of Computerized Tomographic Imaging*. Society for Ind. Appl. Math, 2001. 35, 36

[101] J Radon. On the determination of functions from their integral values along certain manifolds. *IEEE Trans. Med. Imag.*, 5(4):170, 1986. 35

[102] M Wollenhaupt, M Krug, J Kohler, T Bayer, C Sarpe-Tudoran, and T Baumert. *App. Phys. B*, 95:647, 2009. 35

[103] L Shepp and B Logan. *IEEE Trans. Nucl. Sci.*, NS-21(1):21, 1974. 36

[104] T Brabec, M Y Ivanov, and P B Corkum. *Phys. Rev. A*, 54(4):R2551, 1996. 41

[105] G Yudin and M Y Ivanov. *Phys. Rev. A*, 63(3):033404, 2001. 41

[106] A S Alnaser, X M Tong, T Osipov, S Voss, C M Maharjan, B Shan, Z Chang, and C L Cocke. *Phys. Rev. A*, 70(2):023413, 2004. 42, 44, 53, 57, 59

[107] I V Litvinyuk, K F Lee, P W Dooley, D M Rayner, D M Villeneuve, and P B Corkum. Alignment-dependent strong field ionization of molecules. *Phys. Rev. Lett.*, 90:233003, 2003. 44, 88, 94

[108] S M Hankin, D. M. Villeneuve, P.B. Corkum, and D M Rayner. *Phys. Rev. A*, 64(1):013405, 2001. 45, 56

[109] V Schyja, T Lang, and H Helm. *Phys. Rev. A*, 57(5):3692, 1998. 45

[110] P Kaminski, R Wiehle, V Renard, A Kazmierczak, B Lavorel, O Faucher, and B Witzel. *Phys. Rev. A*, 70(5):053413, 2004. 45

[111] C M Maharjan, A Alnaser, I V Litvinyuk, P Ranitovic, and C L Cocke. *J. Phys. B*, 39:1955, 2006. 45

[112] L Young et al. *Phys. Rev. Lett.*, 97:083601, 2006. 48

[113] Z H Loh, M Khalil, R E Correa, R Santra, C Buth, and S R Leone. *Phys. Rev. Lett.*, 98:143601, 2007. 48

[114] B Podolsky and L Pauling. *Phys. Rev.*, 34(1):109, 1929. 48, 98

[115] H Bethe and E Salpeter. *Quantum Mechanics of One and Two Electron Atoms*. Dover, 2008. 48, 72, 98

[116] E Clementi and D L Raimondi. *J. Chem. Phys.*, 38(11):2686, 1963. 48, 98

[117] R Wiehle, B Witzel, H Helm, and E Cormier. *Phys. Rev. A*, 67(6):063405, 2003. 56

[118] P R Bevington and D K Robinson. *Data Reduction and Error Analysis for the Physical Sciences*. McGraw-Hill, 2nd edition, 1992. 60

[119] Justin E. Molloy and Miles J. Padgett. Lights, action: Optical tweezers. *Contemporary Physics*, 43(4):241–258, 2002. 63

[120] W D Phillips. Nobel Lecture: Laser cooling and trapping of neutral atoms. *Rev. Mod. Phys.*, 70:721–741, 1998. 63

[121] N. B. Simpson, K. Dholakia, L. Allen, and M. J. Padgett. Mechanical equivalence of spin and orbital angular momentum of light: an optical spanner. *Opt. Lett.*, 22(1):52–54, Jan 1997. 63

[122] C C Cheng, E M Wright, and J V Moloney. *Phys. Rev. Lett.*, 87(21):213001, 2001. 63, 72

[123] C D Amico, A Houard, S Akturk, Y Liu, J Le Bloas, M Franco, B Prade, A Couairon, V T Tikhonchuk, and A Mysyrowicz. *New J. Phys.*, 10:013015, 2008. 63, 72

[124] P Sprangle, J R Penano, B Hafizi, and C A Kapetanakos. *Phys. Rev. E*, 69(9):066415, 2004. 63

[125] B Zhou, A Houard, Y Liu, B Prade, A Mysyrowicz, A Couairon, P Mora, C Smeenk, L Arissian, and P B Corkum. Measurement and control of plasma oscillations in femtosecond filaments. *Phys. Rev. Lett.*, 106:255002, 2011. 63, 72, 92

[126] C I Moore, J P Knauer, and D D Meyerhofer. *Phys. Rev. Lett.*, 74(13):2439, 1995. 63

[127] D D Meyerhofer, J P Knauer, S J McNaught, and C I Moore. *J Opt. Soc. Am. B*, 13(1):113, 1996. 63

[128] A Couairon and A Mysyrowicz. *Phys. Rep.*, 441:41, 2007. 63, 71

[129] E Yablonovitch. *Phys. Rev. Lett.*, 60(9):795, 1988. 65, 66, 70, 73

[130] W.M. Wood, C.W. Siders, and M.C. Downer. Femtosecond growth dynamics of an underdense ionization front measured by spectral blueshifting. *IEEE Trans. Plasma Science*, 21(1):20 –33, 1993. 65, 73

[131] C Smeenk, J Z Salvail, L Arissian, P B Corkum, C T Hebeisen, and A Staudte. Precise in-situ measurement of laser pulse intensity using strong field ionization. *Opt. Exp.*, 19(10):9336, 2011. 68

[132] H R Reiss. *Phys. Rev. Lett.*, 101(4):043002, 2008. 72

[133] P B Corkum, N H Burnett, and F Brunel. Multiphoton ionization in large ponderomotive potentials. In M Gavrila, editor, *Atoms in Intense Laser Fields*, pages 109–137. Academic Press, 1992. 73, 94

[134] S Ali, J R Davies, and J T Mendonca. *Phys. Rev. Lett.*, 105(3):035001, 2010. 74

[135] M Schnell and G Meijer. Cold molecules: Preparation, applications, and challenges. *Angew Chem Int Ed*, 48:6010–6031, 2009. 75, 92

[136] L S Cederbaum, W Domcke, J Schirmer, and W von Niessen. Correlation effects in the ionization of molecules: Breakdown of the molecular orbital picture. *Adv. Chem. Phys.*, 65:115–159, 1986. 75

[137] S Patchkovskii, Z Zhao, T Brabec, and D M Villeneuve. High harmonic generation and molecular orbital tomography in multielectron systems: Beyond the single active electron approximation. *Phys. Rev. Lett.*, 97:123003, 2006. 75, 83

[138] O Smirnova, S Patchkovskii, Y Mairesse, N Dudovich, and M Y Ivanov. *PNAS*, 106(39):16556, 2009. 75

[139] I Nevo, L Holmegaard, J H Nielsen, J L Hansen, H Stapelfeldt, F Filsinger, G Meijer, and J Küpper. Laser-induced 3d alignment and orientation of quantum state-selected molecules. *Phys. Chem. Chem. Phys.*, 11:9912–9918, 2009. 76, 92

[140] F Filsinger, J Küpper, G Meijer, J L Hansen, J Maurer, J H Nielsen, L Holmegaard, and H Stapelfeldt. Pure samples of individual conformers: The separation of stereoisomers of complex molecules using electric fields. *Angew Chem Int Ed*, 48(37):6900, 2009. 76

[141] J L Hansen, L Holmegaard, L Kalhøj, S L Kragh, H Stapelfeldt, F Filsinger, G Meijer, J Küpper, D Dimitrovski, M Abu-samha, C P J Martiny, and L B Madsen. Ionization of one- and three-dimensionally-oriented asymmetric-top molecules by intense circularly polarized femtosecond laser pulses. *Phys. Rev. A*, 83:023406, Feb 2011. 76

[142] P.W. Atkins and R.S. Friedman. *Molecular Quantum Mechanics*. Oxford University Press, 3rd edition, 1997. 76, 77

[143] M Spanner. *Field-Free Alignment and Strong Field Control of Molecular Rotors*. PhD thesis, University of Waterloo, 2004. 77

[144] T Seideman, M Y Ivanov, and P B Corkum. Role of electron localization in intense-field molecular ionization. *Phys. Rev. Lett.*, 75:2819–2822, Oct 1995. 81

[145] X M Tong, Z X Zhao, and C D Lin. Theory of molecular tunneling ionization. *Phys Rev A*, 66:033402, 2002. 83

[146] R Murray, M Spanner, S Patchkovskii, and M Y Ivanov. Tunnel ionization of molecules and orbital imaging. *Phys Rev Lett*, 106:173001, 2011. 83

[147] D. Dimitrovski, C. P. J. Martiny, and L. B. Madsen. Strong-field ionization of polar molecules: Stark-shift-corrected strong-field approximation. *Phys. Rev. A*, 82:053404, Nov 2010. 83

[148] C T L Smeenk, M Giguère, E Bisson, P B Corkum, and F Légaré. (unpublished results), 2012. 85

[149] S Shimizu, V Zhakhovskii, F Sato, S Okihara, S Sakabe, K Nishihara, Y Izawa, T Yatsuhashi, and N Nakashima. Coulomb explosion of benzene induced by an intense laser field. *J Chem Phys*, 117(7):3180–3189, 2002. 85

[150] S Anand and H B Schlegel. Dissociation of benzene dication $C_6H_6{}^{2+}$: Exploring the potential energy surface. *J Phys Chem A*, 109:115551, 2005. 85

[151] M Alagia, P Candori, S Falcinelli, F Pirani, M S P Mundim, R Richter, M Rosi, S Stranges, and F Vecchiocattivi. Dissociative double photoionization of benzene molecules in the 26-33 eV energy range. *Phys. Chem. Chem. Phys.*, 13:8245, 2011. 85

[152] M. Alagia, P. Candori, S. Falcinelli, M. S. P. Mundim, F. Pirani, R. Richter, M. Rosi, S. Stranges, and F. Vecchiocattivi. Dissociative double photoionization of singly deuterated benzene molecules in the 26–33 ev energy range. *J Chem Phys*, 135(14):144304, 2011. 85

[153] J L Hansen, H Stapelfeldt, D Dimitrovski, M Abu-samha, C P J Martiny, and L B Madsen. Time-resolved photoelectron angular distributions from strong-field ionization of rotating naphthalene molecules. *Phys. Rev. Lett.*, 106:073001, 2011. 90, 92

[154] J. Breidbach and L. S. Cederbaum. Migration of holes: Formalism, mechanisms, and illustrative applications. *J Chem Phys*, 118(9):3983–3996, 2003. 90, 92

[155] J. Breidbach and L. S. Cederbaum. Migration of holes: Numerical algorithms and implementation. *J Chem Phys*, 126(3):034101, 2007. 90, 92

[156] F. Remacle and R. D. Levine. An electronic time scale in chemistry. *PNAS*, 103(18):6793–6798, 2006. 90, 92

[157] C T L Smeenk. **The Laser Musicbox**. http://sites.google.com/site/csmeenk/laser-musicbox. 92

[158] A Stolow and J G Underwood. Time-resolved photoelectron spectroscopy of nonadiabatic dynamics in polyatomic molecules. *Adv. Chem. Phys.*, 139:497, 2008. 92

[159] J. Breidbach and L. S. Cederbaum. Universal attosecond response to the removal of an electron. *Phys. Rev. Lett.*, 94:033901, Jan 2005. 92

[160] A Wirth, M Th Hassan, I Grguraš, J Gagnon, A Moulet, T T Luu, S Pabst, R Santra, Z A Alahmed, A M Azzeer, V S Yakovlev, V Pervak, F Krausz, and E Goulielmakis. Synthesized light transients. *Science*, 334(6053):195, 2011. 92

[161] D R Lide, editor. *CRC Handbook of Chemistry and Physics.* CRC Press, 83rd edition, 2002. 96

[162] K Kimura, S Katsumata, Y Achiba, T Yamazaki, and S Iwata. *Handbook of HeI Photoelectron Spectra of Fundamental Organic Molecules.* Japan Scientific Societies Press, 1981. 97